Department of Materials Science and Engineering
University of Sheffield

La doped SrTiO$_3$ Based Oxide Thermoelectrics

A thesis submitted for the degree of
Doctor of Philosophy by

Zhilun Lu

Supervisors:

Prof. I. M. Reaney

Prof. D.C. Sinclair

October 2015

Publications from this Thesis:

Published:

Z. Lu, D. C. Sinclair and I. M. Reaney, The Influence of La Doping and Heterogeneity on the Thermoelectric Properties of $Sr_3Ti_2O_7$ Ceramics, Journal of the American Ceramic Society, (2015) (DOI: 10.1111/jace.13998).

Z. Lu, H. Zhang, W. Lei, D. C. Sinclair and I. M. Reaney, High Figure of Merit Thermoelectric La-Doped A-site Deficient $SrTiO_3$ Ceramics. Chemistry of Materials, (2016). (DOI: 10.1021/acs.chemmater.5b04616)

Acknowledgement

As an ancient Chinese proverb states: ‘The teacher is the one who could propagate the doctrine, impart professional knowledge, and resolve doubts.’ My Ph.D. research supervisors, Professor I. M. Reaney and Professor D. C. Sinclair did perfectly to guide me to complete my project. Without their support and encouragement, I could never have finished my thesis. I would like to express my great appreciation here to them. Their profound insight, great wisdom and excellent scientific quality can be of benefit to my whole life.

I would like to express my sincerest thanks to the members in my lab (Dr Dawei Wang, Dr Rebecca Boston, Dr Fan Yang, Andrew Mould, Linhao Li, Yun Dang, Yen-Ju Wu, Bo Dong, Dr Rouzbeh Jarkaneh, Adil Al Shoaibi, Amir Khesro, Simon Nicholls, Fayaz Hussain and Greg Lewin). I am lucky and happy to have worked with them in such a high efficient and friendly environment. I am also grateful to Dr I. Sterianou for her guidance in the beginning of my project, Dr Ming Li and Dr Yang Liu for their insightful advice. My special thanks go to Dr Huairuo Zhang, Dr Claire Utton and Ben G Palmer for their great help in my experiments. I also want to thank my internal assessors, Professor N. C. Hyatt and Professor R. J. Hand.

Finally, I would like to thank my parents who always take care of me meticulously. I also want to send my special thanks to my dear girlfriend, Dr Xingjie Wei, for her company and support in my life no matter what happiness or sorrow.

Abstract

In this project, the thermoelectric properties of La-doped $Sr_3Ti_2O_7$, $Ca_3Ti_2O_7$ and $SrTiO_3$ ceramics sintered in air and N_2/5%H_2 have been investigated. Different defect chemistry models were studied in an attempt to improve the thermoelectric performance of La-doped $SrTiO_3$ and related systems.

For La-doped $Sr_3Ti_2O_7$ Ruddlesden-Popper (RP) ceramics, the three starting nominal compositions, $(Sr_{1-x}La_x)_3Ti_2O_7$ (electronic donor-doping), $(Sr_{1-3y/2}La_y)_3Ti_2O_7$ (A-site vacancies) and $(Sr_{1-z}La_z)_3Ti_{2-z/4}O_7$ (B-site vacancies) were sintered under air and flowing N_2/5%H_2 at 1773 K. The La-doped air sintered ceramics were all off-white/yellow in appearance and electrical insulators with low bulk conductivity and a high activation energy, E_a, confirming that solid solubility of La was small and that electronic (donor-doping) compensation does not exist for La-doping of ceramics sintered in air. Processing ceramics under reducing atmosphere is sufficient to form dark single-phase samples for the x series (electronic donor-doping series) up to $(Sr_{0.95}La_{0.05})_3Ti_2O_7$ ($x = 0.05$), indicating that reducing conditions and oxygen-loss from the $Sr_3Ti_2O_7$ lattice are conducive towards electronic La-doping in $Sr_3Ti_2O_{7-\delta}$ ceramics and to extend solid solubility. In all N_2/5%H_2 sintered samples, an insulating surface layer associated with SrO volatilization and oxygen up-take (during cooling) from the sintering process occurred that, unless removed, masked the conductive nature of the ceramics. In the bulk, significantly higher power factors were obtained for ceramics that were phase mixtures containing highly conductive $(Sr, La)TiO_{3-\delta}$, ST. This highlights the superior power factor properties of reduced perovskite-type ST compared to reduced RP-type $Sr_3Ti_2O_7$ and serves as a warning for the need to identify low levels of highly conducting perovskite phases when exploring rare-earth doping mechanisms in RP-type phases.

For La-doped $SrTiO_3$, the favoured mechanism for doping was through the formation of A-site vacancies independent of P_{O_2}. Samples with A-site vacancies ($Sr_{1-3y/2}La_yTiO_3$) had the highest electrical conductivity for the same La content (i.e. 10 at. %) sintered at 1773 K, independent of P_{O_2}. In the $Sr_{1-3y/2}La_yTiO_3$ system, air sintered ceramics were metrically cubic for $0.1 \leq y < 0.30$, tetragonal with short range strontium vacancy, V_{Sr}, ordering for $0.30 \leq y < 0.50$, then orthorhombic with long range ordering of V_{Sr} for $y \geq 0.50$ by X-ray powder and electron diffraction at room temperature. For samples reduced in N_2/5%H_2, compositions with $0.1 \leq y \leq 0.50$ were metrically cubic. Short range V_{Sr} ordering and an orthorhombic structure with long range V_{Sr} ordering were observed for y = 0.50 and 0.63, respectively. Samples with y = 0.15 sintered in N_2/5%H_2 revealed the largest dimensionless thermoelectric figure-of-merit (ZT = 0.41 at 973 K) reported for n-type $SrTiO_3$ based materials, suggesting that the accommodation of La through the formation of V_{Sr} accompanied by reduction in N_2/5%H_2 represents a new protocol for the development of oxide-based thermoelectrics.

Contents

Chapter 1: Introduction

Energy consumption and environmental issues are two of the major concerns for developed economies. The change of global climate due to the burning of fossil fuels and black carbon[1] in the environment is becoming increasingly problematic. As materials that are able to generate electricity from waste heat, thermoelectrics (TE) have attracted huge interest as part of a range of solutions to establish a sustainable technological society[2]. Thermoelectric power generation represents one of the best candidate technologies to reduce our dependency on conventional power sources[3] since it converts waste heat to electricity. To date, the use of TE devices has been proposed for TE-solar hybrid systems[4,5] and waste-heat harvesting in power stations or in vehicles[6] but has to date primarily been used for radioisotope thermoelectric generation (NASA's Voyager and Cassini missions)[7], local cooling in computer chips, mini-refridgerators and air conditioners. TE generators are solid-state devices with no moving parts. They are lightweight, scalable, exhibit no wear and are quiet, and reliable, making them ideal for small, distributed power generation and to replace compression-based refridgeration[3, 8].

Nevertheless, low conversion efficiency and high manufacturing costs have limited many applications of most thermoelectric materials. Therefore, the development of higher-performance thermoelectric materials plays an indispensable role in realising the full potential of power generation and refridgeration. The efficiency of a given material to produce thermoelectric power is governed by its dimensionless figure of merit ZT. Traditional thermoelectric materials, such as PbTe[9, 10] and Bi_2Te_3[11, 12] are composed of toxic, naturally rare elements but have been developed for thermoelectric modules due to their high figure of merit (ZT) values. However, these materials can be oxidised and melt at high temperature in air, which leads to the necessity for high temperature thermoelectric oxides.

Although many thermoelectric oxides have been investigated, in general, most p-type oxides with good thermoelectric performance are ternary and quaternary cobaltates with a common CoO_2 layer, such as $NaCo_2O_4$[13], $(Sr,Ca)_3Co_4O_9$[14], $Bi_{2-x}Pb_xSr_2Co_2O_8$ ($0 \leq x \leq 0.4$)[15], $Tl_{0.4}[Sr_{0.9}O]_{1.12}CoO_2$[16] and $[Pb_{0.7}Hg_{0.4}Sr_{1.9}Co_{0.2}O_3][CoO_2]_{1.8}$[17]. They have ZT values of ~0.8-1 at 800-1000 K. Compared to p-type thermoelectric oxides, n-type oxides with equivalent ZT values have yet to be discovered. The best n-type thermoelectric oxide to date is Al, Ga co-doped ZnO, which show ZT = 0.47 at 1000 K[18]. Other promising n-type oxides are $CaMnO_3$, In_2O_3 and $SrTiO_3$. Nb-doped $CaMnO_3$ has produced a ZT value of 0.27 at 1000 K[19]. Recently, a ZT value of 0.44 at 973 K has been found in $In_{2-2x}Zn_xCe_xO_3$[20]. As a good electronic conductor, $SrTiO_3$ doped with either Nb or La, has ZT ≈ 0.37 and 0.26 at 1000 K[21], respectively. ZT for $Sr_3Ti_2O_7$, Ruddlesden-Popper compounds, have been reported to achieve a maximum of 0.24 at 1000 K for $(Sr_{0.95}Gd_{0.05})_3Ti_2O_7$[22, 23].

Most research on $SrTiO_3$-based thermoelectrics has focused on donor doping mechanisms with higher valence ions on the A- or B-site, especially La-doped $SrTiO_3$ (LST)[24, 25]. The effect of A-site cation deficiency on the thermoelectric performance of donor-doped $SrTiO_3$ has been reported only by J.-W. G. Bos *et al.*[26] and Kovalevsky *et al.*[27] but there is still no report on the influence of other doping mechanisms (i.e. B-site deficiency) on thermoelectric properties. Moreover, no other mechanisms, except donor doping, have been investigated in La-doped $Sr_3Ti_2O_7$ systems. The main goal for this project was therefore to explore different potential defect doping mechanisms for La-doped $SrTiO_3$ and $Sr_3Ti_2O_7$ prepared in air and under reducing conditions to establish the thermoelectric properties and their relation to crystal structure, defect chemistry and ceramic microstructure.

Reference

1 V. Ramanathan and G. Carmichael, Nature Geoscience 1, 221 (2008).

2 D. M. Rowe, International Journal of Innovations in Energy Systems and Power 1, 13 (2006).

3 T. M. Tritt, Annual Review of Materials Research 41, 433 (2011).

4 K. T. Park, S. M. Shin, A. S. Tazebay, H. D. Um, J. Y. Jung, S. W. Jee, M. W. Oh, S. D. Park, B. Yoo, C. Yu and J. H. Lee, Scientific reports 3, 2123 (2013).

5 T. M. Tritt, H. Boettner and L. Chen, Mrs Bulletin 33, 366 (2008).

6 S.-K. Kim, B.-C. Won, S.-H. Rhi, S.-H. Kim, J.-H. Yoo and J.-C. Jang, Journal of Electronic Materials 40, 778 (2011).

7 J. H. Yang and T. Caillat, Mrs Bulletin 31, 224 (2006).

8 L. E. Bell, Science 321, 1457 (2008).

9 V. J. Joseph, P. Heremans, Eric S. Toberer, Ali Saramat, Ken Kurosaki, Anek Charoenphakdee, Shinsuke Yamanaka and G. Jeffrey Snyder, Science 321, 554 (2008).

10 Y. Takagiwa, Y. Pei, G. Pomrehn and G. J. Snyder, Applied Physics Letters 101, 092102 (2012).

11 B. Poudel, Q. Hao, Y. Ma, Y. Lan, A. Minnich, B. Yu, X. Yan, D. Wang, A. Muto, D. Vashaee, X. Chen, J. Liu, M. S. Dresselhaus, G. Chen and Z. Ren, Science 320, 634 (2008).

12 X. B. Zhao, X. H. Ji, Y. H. Zhang, T. J. Zhu, J. P. Tu and X. B. Zhang, Applied Physics Letters 86, 062111 (2005).

13 I. Terasaki, Y. Sasago and K. Uchinokura, Physical Review B 56, R12685 (1997).

14 N. Van Nong, N. Pryds, S. Linderoth and M. Ohtaki, Advanced Materials 23, 2484 (2011).

15 T. Yamamoto, K. Uchinokura and I. Tsukada, Physical Review B 65, 184434 (2002).

16 S. Hébert, S. Lambert, D. Pelloquin and A. Maignan, Physical Review B 64, 172101 (2001).

17 D. Pelloquin, A. Maignan, S. Hébert , C. Martin, M. Hervieu, C. Michel, L. B. Wang and B. Raveau, Chemistry of Materials 14, 3100 (2002).

18 M. Ohtaki, K. Araki and K. Yamamoto, Journal of Electronic Materials 38, 1234 (2009).

19 L. Bocher, M. H. Aguirre, D. Logvinovich, A. Shkabko, R. Robert, M. Trottmann and A. Weidenkaff, Inorganic Chemistry 47, 8077 (2008).

20 J. L. Lan, Y. Liu, Y. H. Lin, C. W. Nan, Q. Cai and X. Yang, Scientific Reports 5, 7783 (2015).

21 K. Koumoto, I. Terasaki and R. Funahashi, MRS Bulletin 31, 206 (2006).

22 Y. Wang, K. H. Lee, H. Hyuga, H. Kita, H. Ohta and K. Koumoto, Journal of Electroceramics 24, 76 (2008).

23 Y. Wang, K. H. Lee, H. Ohta and K. Koumoto, Journal of Applied Physics 105, 103701 (2009).

24 J. Ravichandran, W. Siemons, D.-W. Oh, J. T. Kardel, A. Chari, H. Heijmerikx, M. L. Scullin, A. Majumdar, R. Ramesh and D. G. Cahill, Physical Review B 82, 165126 (2010).

25 J. Liu, C. L. Wang, W. B. Su, H. C. Wang, P. Zheng, J. C. Li, J. L. Zhang and L. M. Mei, Applied Physics Letters 95, 162110 (2009).

26 S. R. Popuri, A. J. M. Scott, R. A. Downie, M. A. Hall, E. Suard, R. Decourt, M. Pollet and J.-W. G. Bos, RSC Advances 4, 33720 (2014).

27 A. V. Kovalevsky, A. A. Yaremchenko, S. Populoh, A. Weidenkaff and J. R. Frade, The Journal of Physical Chemistry C 118, 4596 (2014).

Chapter 2: Literature Review

2.1 Background to ABO_3 Perovskites

2.1.1 Cubic Perovskite and Ruddlesden-Popper Structured Phases

The formula of an ideal cubic perovskite is ABX_3, the structure of which is shown in Figure 2.1. The A cation is surrounded by 12 X anions in cuboctahedral coordination. The B cation is in the centre of an octahedral cage surrounded by 6 X anions. The A site ion is larger than the B site ion, and X is an anion of similar size to the A site cation. The cuboctahedral volume is approximately five times larger than the octahedral volume, especially in the ideal cubic structure. The ideal ABX_3 structure adopts the space group $Pm\bar{3}m$ ($P4/m\bar{3}2/m$ #221). $SrTiO_3$ is commonly considered as showing the ideal cubic perovskite structure with a lattice parameter of 3.905 Å at room temperature.[1]

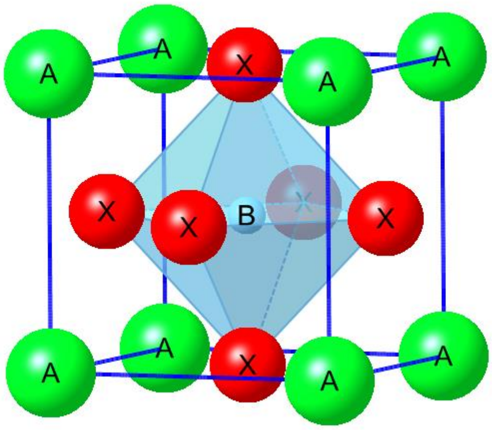

Figure 2.1 The ideal perovskite structure, ABX_3.

Ruddlesden-Popper compounds with general formula $A_{n+1}B_nX_{3n+1}$ were first synthesised and described by S.N. Ruddlesden and P. Popper in 1957[2, 3].

The general formula can also be written as $AX(ABX_3)_n$, which means that compounds have a layer structure with one AX unit per n perovskite blocks. Figure 2.2 illustrates the structure of $Sr_3Ti_2O_7$ with the I4/mmm space group, which is the archetypal n = 2 member in Ruddlesden-Popper systems. The TiO_6 octahedra shear along $\{001\}_C$ planes with a displacement vector of (perovskite lattice parameter) $a_p/\sqrt{2}$ along $[110]_p$. Therefore, the original corner-sharing octahedral framework is broken. To offset this deficiency, the SrO unit resides between the perovskite layers, resulting in transformation from cubic to tetragonal symmetry.

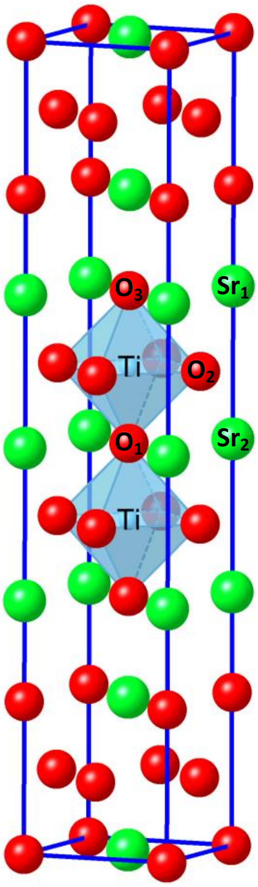

Figure 2.2 The crystal structure of $Sr_3Ti_2O_7$.

2.1.2 Defect Chemistry of $ATiO_3$ (A = Ba, Sr)

$BaTiO_3$

As a well-known system, $BaTiO_3$ has drawn a lot of attention due to its versatile applications including photorefractive materials[4], microwave dielectrics[5], piezoelectric transducers[6] and actuators, multilayer ceramic capacitors (MLCC)[7-9], random access memory (RAM)[10, 11] and positive temperature coefficient of resistance (ptcr) thermistors[12, 13].

The dielectric properties of $BaTiO_3$ stem from a series of phase transitions as a function of temperature, as shown in Figure 2.3[14]. The cubic perovskite phase (space group $Pm\bar{3}m$) is only stable above 125 ℃ with a lattice parameter of 3.996 Å. Below this temperature, $BaTiO_3$ adopts a series of non-centrosymmetric space groups whose structures are ferroelectric. Much work has been dedicated to the relationship between structure and the ferroelectric properties in $BaTiO_3$ based compositions[15-18].

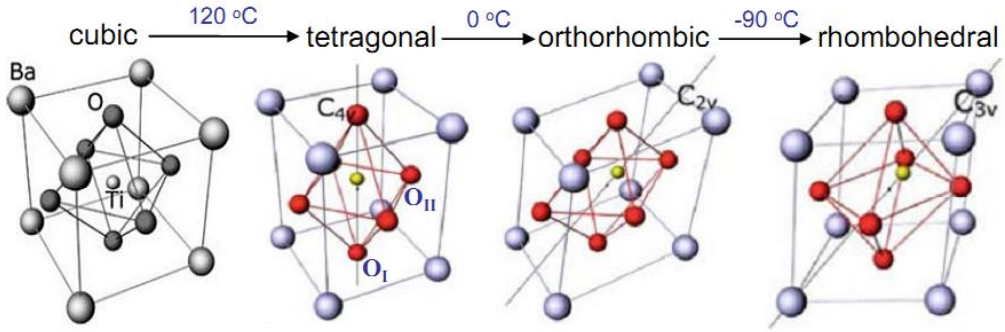

Figure 2.3 Phase transitions of $BaTiO_3$[14].

Due to its use in MLCCs over the last ~30 years there has been a need to understand better the defect chemistry of $BaTiO_3$[19-22]. The defect chemistry of undoped and doped $BaTiO_3$ has been extensively studied by means of thermogravimetry[23], chemical diffusivity[24,25], electrical conductivity measurements[21,22] and Transmission Electron Microscopy (TEM)[26]. However, many discrepancies still exist between reported experimental data and theoretical models. $BaTiO_3$ invariably contains an excess of naturally occurring acceptor-type impurities that have lower valence than the ion which they replace (Ti^{4+} is substituted by Fe^{3+}, Mn^{2+}, Mg^{2+}, etc.)[21]. Hagemann *et al.* have shown the impurity elements of $BaTiO_3$ powders analysed by spectrochemical and X-ray fluorescence, Table 2.1[23]. Although their maximum concentrations are below 100 parts per million (ppm), they play crucial roles in the defect chemistry of $BaTiO_3$, which can be described for acceptor dopants according to the equation:

$$A_2O_3 + 2\mathrm{BaO} \rightarrow 2Ba_{Ba}^{x} + 2\mathrm{A}'_{Ti} + 5O_O^{x} + V_O^{\cdot\cdot} \qquad 2\text{-}1$$

Table 2.1 Typical results of impurity analyses of $BaTiO_3$ ceramics[23]

Impurity element	Weight (ppm)	Remarks
Sr	6500	Isovalent substitution
Ca	70	
Sn	<5	
Pb	<5	
Si	200	Low solubility in perovskite matrix
Al	30	
Na	20	
Cu	1	
Fe	60	Off-valency impurities incorporated in the $BaTiO_3$
Mg	20	
Mn	2	

From equation 2-1, it is evident that acceptor impurities (and dopants) are compensated by oxygen vacancies. Hence the properties of $BaTiO_3$ should be strongly influenced by P_{O_2}. The equilibrium electrical conductivity of undoped polycrystalline $BaTiO_3$ is represented in Figure 2.4 using log-log plots of the electrical conductivity as a function of oxygen partial pressure at 50 ℃ intervals[22]. The minimum value of conductivity corresponds to the completely compensated state, which can be designated as $P_{O_2}^0$. For $P_{O_2} < P_{O_2}^0$, $BaTiO_3$ has rising n-type conductivity with decreasing P_{O_2} due to a stoichiometric deficiency of oxygen. The equilibrium in the reduction reaction region can be expressed as:

$$O_O^x \rightleftharpoons {}^1\!/_2\, O_2 + V_O^{\cdot\cdot} + 2e' \qquad 2\text{-}2$$

For $P_{O_2} > P_{O_2}^0$, the behaviour of the increase in conductivity with P_{O_2} can be explained by means of a reaction for compensation of the impurity-related oxygen vacancies by excess oxygen:

$$V_O^{\cdot\cdot} + {}^1\!/_2\, O_2 \rightleftharpoons O_O^x + 2h^{\cdot} \qquad 2\text{-}3$$

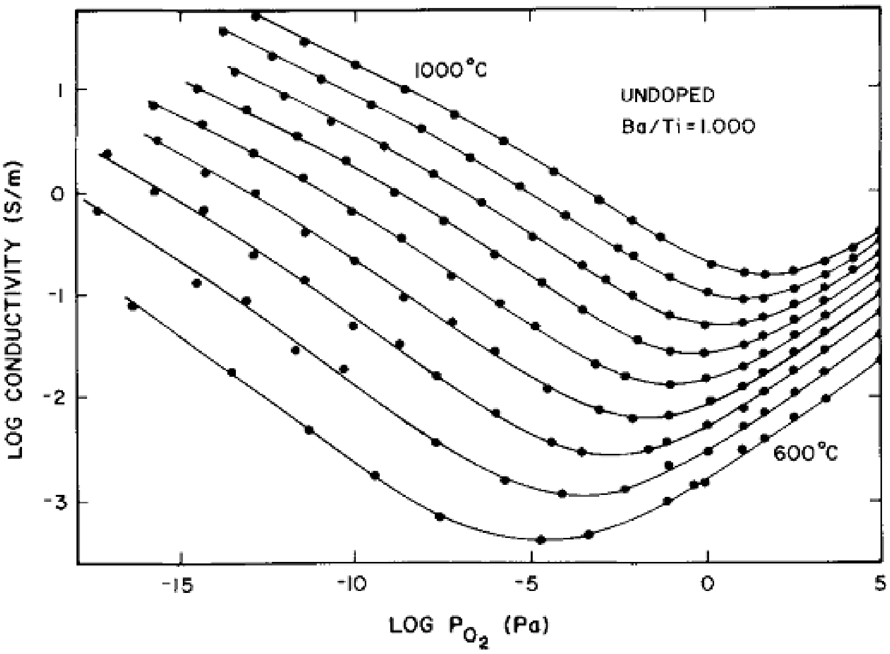

Figure 2.4 Equilibrium electrical conductivity of undoped polycrystalline $BaTiO_3$ from 600 to 1000 ℃ at 50 ℃ intervals[22].

Donor dopants in $BaTiO_3$ are usually large trivalent cations substituted at the Ba-site, e.g., La^{3+}, and intermediate-sized cations that can sit on the Ti site, e.g., Nb^{5+}. However, the compensation mechanisms are complex for donor-doped $BaTiO_3$ and can also be dependent on the conditions of synthesis, e.g. temperature and P_{O_2}. Although interstitial anions have been regarded as being unlikely in the perovskite structure, there are still three options for the positively charged donors to be compensated by: Ba-site vacancies, Ti-site vacancies, or electrons. If La is the dopant, these may be written in Kroger-Vink notation as:

$$La_2O_3 + 3TiO_2 \Rightarrow 2La_{Ba}^{\cdot} + V_{Ba}'' + 3Ti_{Ti}^{x} + 9O_{O}^{x} \qquad 2\text{-}4$$

$$2La_2O_3 + 3TiO_2 \Rightarrow 4La_{Ba}^{\cdot} + V_{Ti}'''' + 3Ti_{Ti}^{x} + 12O_{O}^{x} \qquad 2\text{-}5$$

$$La_2O_3 + 2TiO_2 \Rightarrow 2La_{Ba}^{\cdot} + 2e' + 2Ti_{Ti}^{x} + 6O_{O}^{x} + 1/2O_2(g) \qquad 2\text{-}6$$

It is well known that $BaTiO_3$ with low levels (≤ 0.5 at. %) of either A or B site donor doping is semiconducting and dark-coloured related to the reduction of Ti. This led to the development of two apparently conflicting models. Daniels *et al.*[27] suggested that at 1200 ℃ La is compensated by electrons at low P_{O_2} (< 10^{-7} atm), while ionic compensation dominates at high P_{O_2}. Chan *et al.*[22] suggested an electronic compensation mechanism exists in lightly La-doped $BaTiO_3$ (La ≤ 1 at. %) at all P_{O_2}, because the conductivity is independent of P_{O_2}. A more reasonable model has been proposed by Morrison *et al.*[28]. They suggested a small amount of oxygen loss rather than direct donor doping is the origin of the semiconductivity in La-doped $BaTiO_3$[28]. Unless ceramics are processed in very high P_{O_2} to suppress the oxygen loss, the samples are electrically heterogeneous with a general formula of $Ba_{1-x}La_xTi_{1-x/4}O_{3-\delta}$.

Furthermore, with increasing donor concentration, a transition from semiconducting to insulating behaviour occurs, indicating that ionic compensation dominates at high donor concentrations with Ba-site or Ti-site vacancies. Formation of V_{Ti}'''' was initially considered unlikely due to their high effective charge and tendency to destroy the bonding in crystal structure. However, theoretical calculations[29], equilibrium ternary phase diagram studies[30], atomistic simulations[31] have all certified that V_{Ti}'''' are a favorable defect in $BaTiO_3$. Recently, Freeman *et al.*[32] demonstrated that a model of Ti-site vacancies with subsequent oxygen-loss can explain the semiconductivity in low La-donor concentrations and the insulating behaviour at high doping levels.

$SrTiO_3$

Strontium titanate ($SrTiO_3$) is an electroceramic which exhibits various electronic properties useful in applications such as varistors[33], capacitors[34, 35] substrates for growing superconductors[36], resistive RAM (RRAM)[37], anodes in solid oxide fuel cells (SOFCs)[38-40], field effect transistors (FETs)[41, 42], thermoelectric[43] and as an immobilization host of nuclear waste[44].

At room temperature, $SrTiO_3$ is a cubic perovskite (space group $Pm\bar{3}m$) with a lattice parameter of 0.3905 nm and atomic density of 5.12 g/cm^3. Under the transition temperature reported as being between 105 K[45] and 110 K[46], it undergoes a second order octahedral tilt phase transition to a tetragonal cell based on space group I4/mcm[47].

$SrTiO_3$ is a wide band-gap insulator of 3.2 eV (at T = 0 K) with covalent bonding behaviour resulting from hybridisation of the O-2p states with the Ti-3d states[48]. As its defect structure is similar to $BaTiO_3$, the defect chemical model of $BaTiO_3$ has been applied to $SrTiO_3$[49, 50]. Based on the valence and ionic radii, suitable acceptors have generally been chosen from dopants with a valence lower than four for Ti-site, e.g. Al^{3+}, Cr^{3+}, Fe^{3+}, Ni^{2+}, Mn^{2+}, etc., or Na^+ and K^+ on the Sr-site[56]. The most common donors for $SrTiO_3$ are La^{3+} and Nb^{5+} on the Sr^{2+} and Ti^{4+} sites, respectively.

In general, undoped $SrTiO_3$ exhibits slightly acceptor-doped behaviour because of the natural relative abundance of acceptor-type impurities in TiO_2, similar to that in $BaTiO_3$. Chan *et al.* studied the defect chemistry of polycrystalline $SrTiO_3$ in the 1980s[57]. They proposed that the properties of polycrystalline $SrTiO_3$ are sensitive to the sintering conditions because of the contribution of excess TiO_2, acceptor impurities and $V_O^{\cdot\cdot}$. The equation for charge neutrality of undoped and acceptor-doped $SrTiO_3$ can be expressed as,

$$2[V_O^{\cdot\cdot}] + p = 2[V_{Sr}''] + [A'] + n \qquad 2\text{-}7$$

where $[A']$ represents the net acceptor content, $n \equiv [e']$ and $p \equiv [h^{\cdot}]$. The experimental results from Balachandran *et al.* agreed well with the defect model proposed by Chan *et al.*, which divided the conductivity curves into three different characteristic regions, Figure 2.5. At very low P_{O_2}, doubly ionized oxygen vacancies dominate as expressed in equation 2-2. In the region between the low P_{O_2} side and the conductivity minima, the pressure dependence of approximately ${P_{O_2}}^{-1/4}$ for the conductivity indicates n-type behaviour governed by acceptor impurities. The last region ($P_{O_2} >$ the conductivity minimum) exhibits p-type behaviour as a result of a stoichiometric excess of oxygen based on equation 2-3.

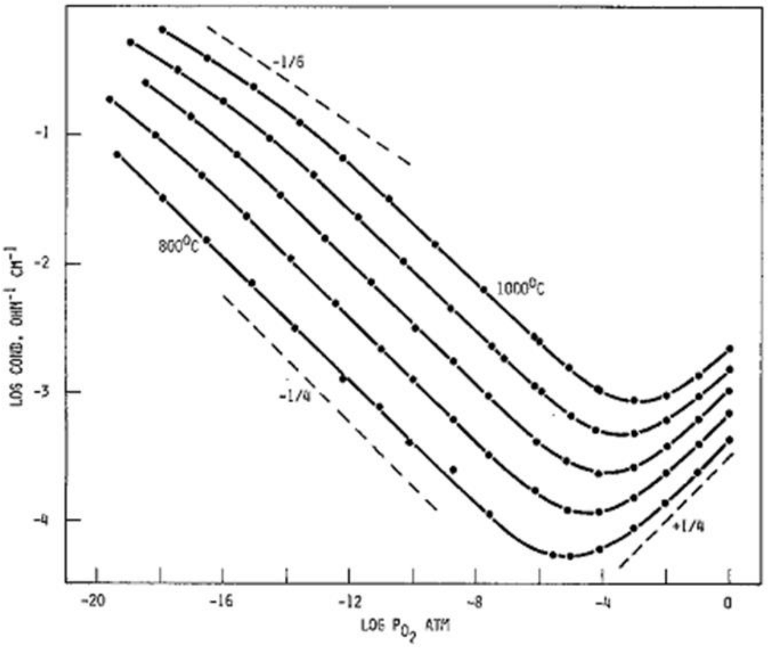

Figure 2.5 Equilibrium conductivity curves of undoped polycrystalline $SrTiO_3$ with Sr/Ti = 1.0000 from 800 ℃ to 1000 ℃ at 50 ℃ intervals[57].

Witek *et al.* studied the electrical properties of $SrTiO_3$ by varying the Sr/Ti ratio, which shows that excess TiO_2 is retained as a second phase in $SrTiO_3$ with Sr/Ti $\leq$ 0.995. The effect of excess TiO_2 on the equilibrium conductivity of $SrTiO_3$ is presented in Figure 2.6. According to the defect model, the compensation of excess TiO_2 occurs with the formation of strontium vacancies (V_{Sr}'') and oxygen vacancies ($V_O^{\cdot\cdot}$) while excess SrO requires the formation of either titanium vacancies (V_{Ti}'''') and oxygen vacancies ($V_O^{\cdot\cdot}$) or interstitial strontium ($Sr_I^{\cdot\cdot}$) and interstitial oxygen (O_I''). Because the interstitial sites are too small for large ions in the perovskite structure and the titanium vacancy has a high effective charge, excess SrO is difficult to generate in large quantities and exists in the form of layer perovskite structures, such as the Ruddlesden-Popper phases[57]. In 1995, Akhtar *et al.* developed a defect model for $SrTiO_3$ using computer simulations, which elucidates that $V_O^{\cdot\cdot}$, $SrTiO_3$ Schottky and SrO "Schottky-like" disorder are more favourable than Ti vacancies and Frenkel defects[58]. Tanaka *et al.* applied first-principles calculations to conclude that oxygen vacancies predominate at low P_{O_2}, whereas the Sr partial Schottky reaction or strontium vacancies exist in the oxidation region[59]. However, according to DFT calculations of intrinsic defect structures in $SrTiO_3$ by Liu *et al.,* the O Frenkel defect also has relatively low formation energy in stoichiometric $SrTiO_3$ and the Schottky defect complex ($V_{Sr}''+ V_{Ti}''''+ 3V_O^{\cdot\cdot}$) is the favoured defect structure. In addition, V_{Sr}'' with $Ti_{Sr}^{\cdot\cdot}$ and $V_O^{\cdot\cdot}$ are the dominant defects for excess TiO_2 whereas $V_O^{\cdot\cdot}$ and Sr_{Ti}'' are preferred for excess SrO in nonstoichiometric $SrTiO_3$[60].

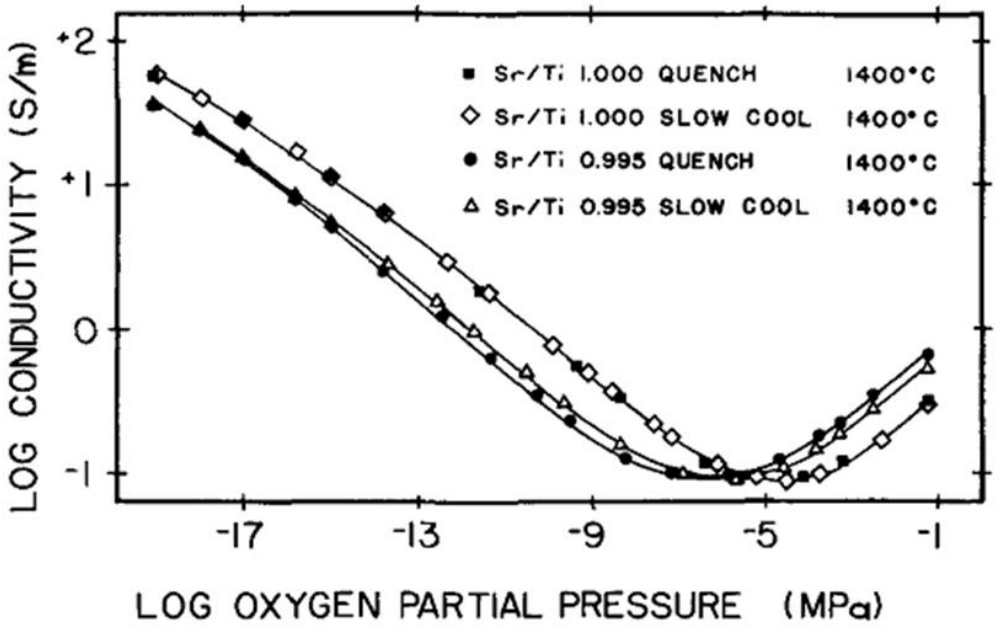

Figure 2.6 Effect of excess TiO_2 on the equilibrium electrical conductivity of polycrystalline $SrTiO_3$ sintered at 1400 ℃, either slow-cooled or quenched.

Compared to undoped and acceptor-doped $SrTiO_3$, the defect chemistry of donor-doped $SrTiO_3$ has attracted more attention, especially La-based strontium titanate’s (LSTs) due to their wide applicability as potential anode and thermoelectric materials. Reports for LST have been inconsistent and contradictory for a long time, especially in respect of the doping mechanisms, solid solution limits and crystal symmetry. This is due, in part, to the sensitivity of LST samples to processing variables such as temperature, P_{O_2} and time. Balachandran and Eror studied the solubility of La in $SrTiO_3$ based on the electronic compensation formula $Sr_{1-x}La_xTiO_3$ by preparing samples using a liquid mix technique in both reduced and oxidised states, which indicated that interstitial mechanisms do not exist and $Sr_{1-x}La_xTiO_3$ ($x \leq 0.40$) is a single phase solid solution with cubic symmetry[61, 62]. However, the cubic symmetry and solid solution limit was found to be lower in $Sr_{1-x}La_xTiO_3$ ($x \leq 0.20$) by Joseph *et al.* using an arc melting technique under Ar atmosphere[63]. Higuchi *et al.*[64], Howard *et al.*[65] and Hashimoto *et al.*[66] observed an increase in lattice parameter with La content for $Sr_{1-x}La_xTiO_3$, which was contrary to that obtained by Eror and Balachandran, as presented in Figure 2.7.

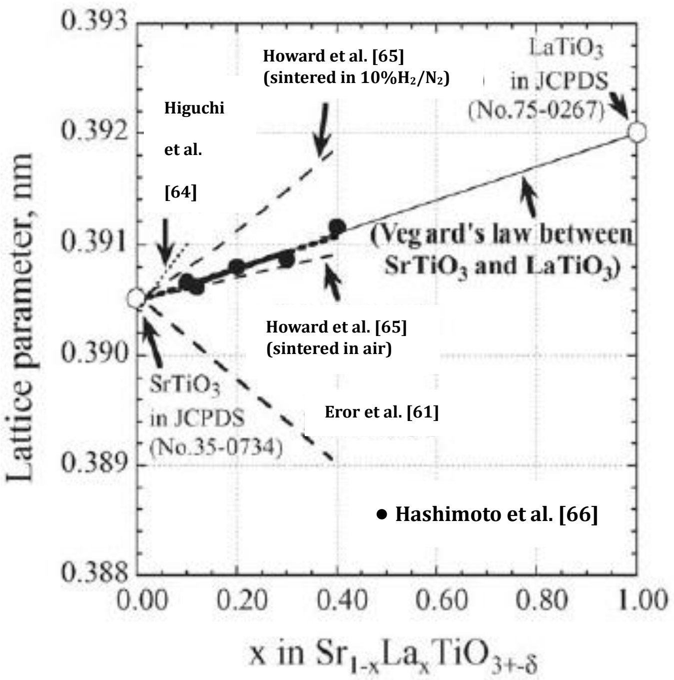

Figure 2.7 Lattice parameter at room temperature as a function of x in $Sr_{1-x}La_xTiO_{3\pm\delta}$. Figure adapted from reference 66.

Three compensation mechanisms are commonly considered for LSTs and they are similar to those considered for donor-doped $BaTiO_3$: Sr-site vacancy, Ti-site vacancy, and electron compensation. So far it is widely accepted that no strong evidence has been provided to suggest that Ti-site vacancies exist in LSTs and that the extra positive charge from substitution of Sr^{2+} by La^{3+} is compensated by electrons offered by the creation of equal numbers of Ti^{3+} from Ti^{4+} with a formula of $La_x{}^{3+}Sr_{1-x}{}^{2+}Ti_x{}^{3+}Ti_{1-x}{}^{4+}O_3{}^{2-}$ in highly reducing conditions[65, 67-69]. However, LST is found to have very low electrical conductivity under oxidising conditions. Moos *et al.* demonstrated that a Sr vacancy compensation mechanism occurs throughout La-doped $SrTiO_3$ samples sintered in oxygen at 1400 ℃ for a La doping level up to 30 at. %[70]. At high P_{O_2}, the uptake of sufficient oxygen results in the formation of SrO layers interleaved with perovskite layers in a similar way to that of Ruddlesden-Popper phases, therefore supporting ionic compensation of La donors by strontium vacancies[70, 71].

In order to determine where excess oxygen may be accommodated in $La_xSr_{1-x}TiO_{3+\delta}$, Irvine *et al.* have proposed a fourth mechanism (intergrowth of two end members, $La_2Ti_2O_7$ and $SrTiO_3$, in the layered perovskites $La_4Sr_{n-4}Ti_nO_{3n+2}$) to describe the intercalation of oxygen in the lattice[72]. As illustrated in Figure 2.8, the excess oxygen atoms locate at the crystallographic shears where the corner-sharing octahedral connectivity is broken. Density measurements were performed to examine different structural models by comparing theoretical and experimental density values, which showed the intergrowth model to be the most suitable for $La_4Sr_{n-4}Ti_nO_{3n+2}$, Figure 2.9.

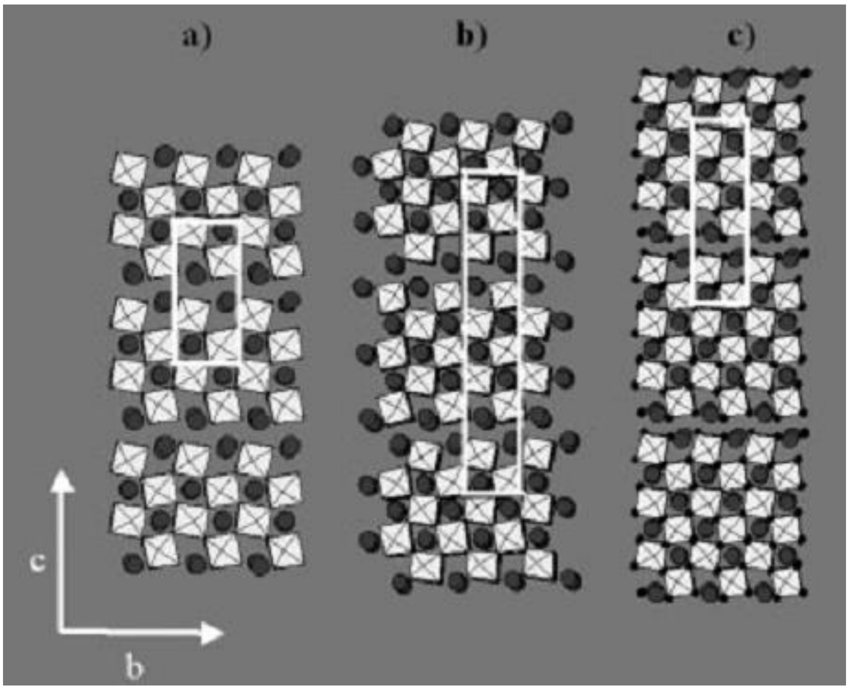

Figure 2.8 Schematic structural models for the $La_4Sr_{n-4}Ti_nO_{3n+2}$ series: (a) $La_2Ti_2O_7$ (n = 4), (b) $La_4SrTi_5O_{17}$ (n = 5) and (c) $La_4Sr_2Ti_6O_{20}$ (n = 6)[72].

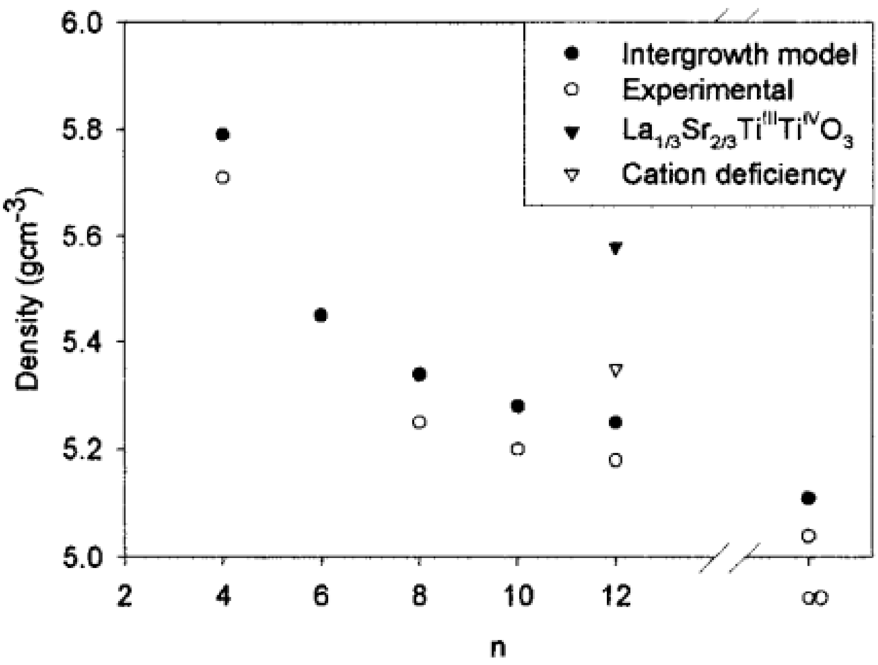

Figure 2.9 Comparison between theoretical and experimental density values for $La_4Sr_{n-4}Ti_nO_{3n+2}$[72].

Furthermore, it is worth noting that Sr-site deficiency is beneficial to the improvement of electrical conductivity in $La_xSr_{1-3x/2}TiO_3$ as compared to stoichiometric compounds ($La_xSr_{1-x}TiO_3$) at the same oxygen partial pressure[73, 74]. However, it is necessary to understand the crystal structures of these systems to answer why A-site deficient compositions have higher electrical conductivity. A-site cation-vacancy ordering has been observed by Battle *et al.* using High resolution (HR) TEM in the system of $La_xSr_{1-3x/2}TiO_3$ ($0.25 \leq x \leq 0.60$)[75]. In Figures 2.10(a) - (d), a change in the [100] zone electron diffraction pattern for the furnace-cooled specimens was observed from x = 0.30 to x = 0.60. Figure 2.11 shows the microstructures from the same part of the electron diffraction patterns in Figure 2.10. A few dispersed Sr-site vacancies appear (Figure 2.11(a)) and are visible in greater concentration (Figure 2.11(b)) as the La-concentration increases. They then form square (cubic) and rectangular (orthorhombic) shapes (Figure 2.11(c)) and finally adopt only orthorhombic symmetry (Figure 2.11(d)). The combined evidence from Figures 2.10 and 2.11

suggests that increasing V_{Sr} and resulting superstructure ordering occurs with increasing La concentration up to x = 0.60. In 2004, Howard *et al.* also showed the existence of an octahedral tilt transition in this system, Figure 2.12[76]. Nevertheless, there is still no definitive report on the influence of cation/vacancy ordering, oxygen-loss and octahedral tilting on the structure-composition-property relations in LST.

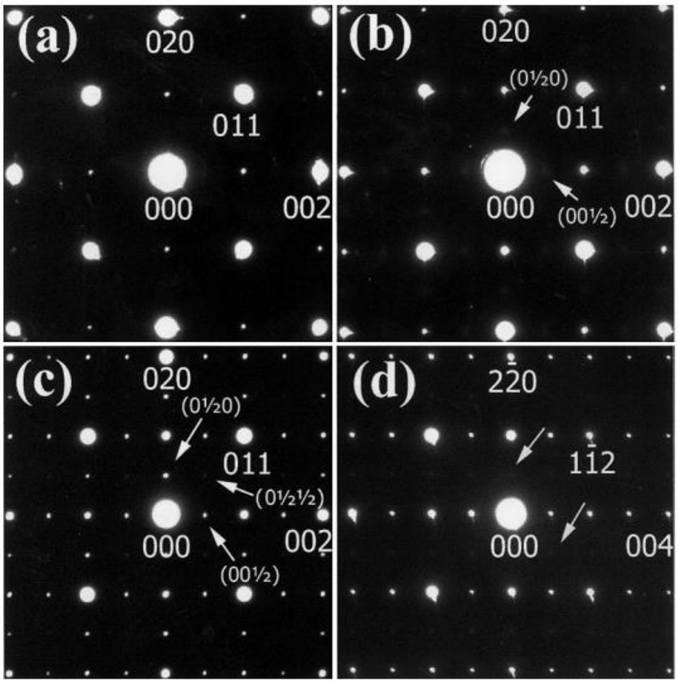

Figure 2.10 Electron diffraction patterns of furnace-cooled $La_xSr_{1-3x/2}TiO_3$ indexed for (a) x = 0.30, (b) x = 0.40, and (c) x = 0.50 as the [100] zone of a cubic system; (d) x = 0.60 is indexed as the [110] zone of an orthorhombic system. Arrows indicate weak reflections[75].

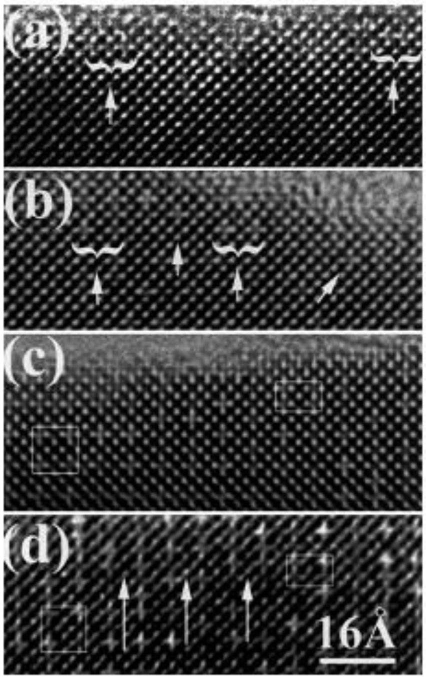

Figure 2.11 Lattice images of furnace-cooled projected along [100] of a cubic system for (a) x = 0.30, (b) x = 0.40, (c) x = 0.50, and along [110] of an orthorhombic system for (d) x = 0.60. The arrows in (a) and (b) point to isolated vacancies or vacancy pairs (bracketed). Square and rectangular vacancy groups are indicated in (c) and (d), and the arrows in (d) indicate the $[1\bar{1}0]$ direction[75].

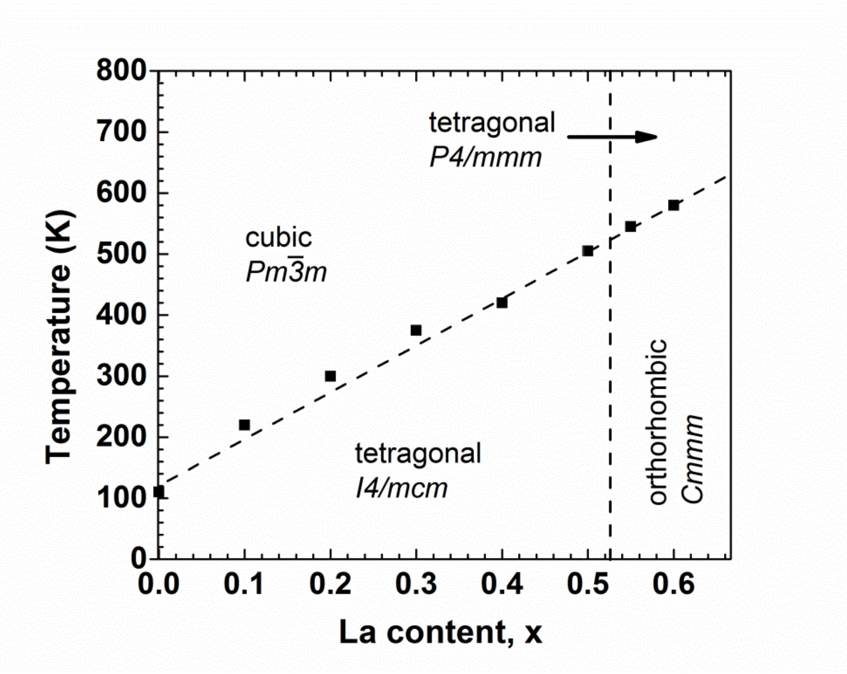

Figure 2.12 A summary of the space groups versus temperature observed for $La_xSr_{1-3x/2}TiO_3$[76].

2.2 Thermoelectric Effects

Generally, thermoelectric effects are composed of three separate identified contributions: the Seebeck, Peltier and Thomson effects.

2.2.1 Seebeck Effect

The Seebeck effect was discovered in 1821 by Thomas Johann Seebeck, who found that a compass needle would deflect in the presence of a material with a temperature difference between two ends[77]. He initially classified it as a magnetic phenomenon and then corrected himself to suggest that it is an electromotive force that can lead to a measurable voltage or current in a closed loop between two ends of a material in response to a temperature gradient across that material. For the junction of two dissimilar metals, metal A and metal B, the relative Seebeck coefficient (also known as thermopower), S_{AB}, is given as:

$$S_{AB} = S_B - S_A = \Delta V_B/\Delta T - \Delta V_A/\Delta T \qquad \text{2-8}$$

where ΔV is the voltage difference between two ends of the material and ΔT is the temperature difference.

The voltages generated by the Seebeck effect are generally small. Therefore, the Seebeck coefficient is expressed as microvolts per kelvin of temperature difference (μV/K). Some thermoelectric devices can produce a few millivolts if the temperature difference is large enough.

The Seebeck effect is used in thermocouples, which are responsible for temperature measurements or to provide electrical power for waste-heat harvesting in power stations if a large temperature difference is maintained across that material.

2.2.2 Peltier Effect

The Peltier effect was discovered by Jean-Charles Peltier in 1834[78] and may be considered as the inverse of the Seebeck effect. It is the appearance of heat generation or absorption within each end of a material upon the application of a current across that material. The Peltier heat (Q) generated per unit time at the junction of two dissimilar metals, metal A and metal B, is equal to:

$$Q = л_{AB}I \qquad \text{2-9}$$

where $л_{AB}$ is the Peltier coefficient, and I is the electric current across this junction.

The Peltier effect can be used for cooling devices such as refridgerators or for heat pump devices involving multiple current-carrying junctions in series.

2.2.3 Thomson Effect

William Thomson (Lord Kelvin) established a relationship (the Thomson effect) between the Seebeck and Peltier coefficients in 1851. The Thomson effect can be summed up as the heating or cooling in a current carrying conductor with a temperature gradient along its length. The Thomson effect predicts the rate of heat generation per unit volume, q, is given as:

$$q = -\tau J \nabla T \qquad \text{2-10}$$

where J is the current density, τ is the Thomson coefficient and where ∇T is the temperature gradient.

Seebeck coefficients vary with changing temperature in many materials and therefore a gradient in the Seebeck coefficient occurs due to a temperature gradient. A current flowing through this gradient will result in a continuous version of the Peltier effect. The first Thomson relation is:

$$\tau = \frac{d\pi}{dT} - S \qquad \text{2-11}$$

where *л* is the Peltier coefficient, T is the absolute temperature and S is the Seebeck coefficient. The second Thomson relation is:

$$\pi = ST \qquad \text{2-12}$$

We can use the Thomson coefficient to determine the absolute Peltier and Seebeck coefficients owing to its uniqueness for individual materials. But the Thomson effect is of little actual application value because it is a secondary effect.

2.3 Thermoelectric Efficiency

Thermoelectric device performance relies on the Carnot efficiency, the intrinsic material parameters and the dimensionless figure of merit ZT.

For Peltier cooling, the measured maximum temperature drop (ΔT_{max}) is used to calculate ZT[79].

$$\Delta T_{max} = \frac{ZT_{cold}^{2}}{2} \qquad \text{2-13}$$

For power generation and the cooling mode, the maximum conversion efficiency of thermoelectrics, η, is respectively expressed as:

$$\eta = \left(\frac{T_{hot}-T_{cold}}{T_{hot}}\right)\left(\frac{\sqrt{1+ZT_{avg}}-1}{\sqrt{1+ZT_{avg}}+\frac{T_{cold}}{T_{hot}}}\right) \qquad \text{2-14}$$

$$\eta = \left(\frac{T_{cold}}{T_{hot}-T_{cold}}\right)\left(\frac{\sqrt{1+ZT_{avg}}-\frac{T_{cold}}{T_{hot}}}{\sqrt{1+ZT_{avg}}+1}\right) \qquad \text{2-15}$$

where the Carnot efficiency is given as the first factor of equation 2-14, T_{avg} is the average temperature $T_{avg} = (T_{\mathrm{hot}}+T_{\mathrm{cold}})/2$. Equation 2-14 indicates that a large temperature gradient and high ZT_{avg} value leads to high conversion efficiency. Increasing the temperature gradient is the aim of generator design. Meanwhile, the figure-of-merit (ZT) can be used to characterise the performance of a thermoelectric device, which is defined as:

$$ZT = \frac{S^2 \sigma T}{\kappa} \qquad 2\text{-}16$$

where S is the Seebeck coefficient as defined earlier, σ is the electrical conductivity and κ is the thermal conductivity. T is the average temperature in Kelvin at which the thermoelectric properties are measured. $S^2\sigma$ is the power factor that is often used to compare thermoelectric materials due to the challenge of obtaining reliable thermal conductivity values[80].

2.4 The Strategy for Improving Thermoelectric Performance

Thermoelectrics have attracted renewed interest, driven by the need for alternative commercial sources of electrical power. They have emerged as a promising contender for electronic refridgeration and power generation applications. Thermoelectrics can convert heat into electricity directly due to the "Seebeck effect". The inverse of this, the "Peltier effect", has been used in thermoelectric refridgeration. Based on these two processes, thermoelectric devices have been applied widely to power generation and energy conservation, for example, waste-heat harvesting in power stations[81-85], local cooling on computer chips, mini-refridgerators, Radioisotope Thermoelectric Generator (RTG), air conditioners and so on. As they are solid-state devices with no moving parts, lightweight, scalable, no wear, low noise, and reliable this makes them ideal for small, distributed power generation and to become the new replacement of compression-based refridgeration[80].

The key to obtaining high ZT values is securing a high Seebeck coefficient (S), high electrical conductivity (σ) and low thermal conductivity (κ), all in the same material[86-92]. A high Seebeck coefficient is related to a high open circuit voltage ($V = S\Delta T$) of a thermoelectric material with a temperature gradient, which therefore determines the power output. A high electrical conductivity can minimize ohmic losses when current passes through the device.

In the meantime, heat transfer across materials of high thermal conductivity occurs at a faster rate than across materials of low thermal conductivity. Therefore, low thermal conductivity leads to a large thermal gradient.

Unfortunately, it is impossible to have all these properties optimised in one material. Metals have very high electrical conductivity but also high thermal conductivity and low Seebeck coefficient. Polymers and glasses have very low thermal conductivity but generally very low electrical conductivity[93]. This has led to the concept of ‘‘phonon-glass, electron-crystal’’ (PGEC) materials which means the best thermoelectrics are crystalline materials that manage to scatter phonons without disrupting the electrical conductivity significantly but still have charge carriers of high mobility, thereby meeting the compromises required for optimizing ZT[80].

2.4.1 Increasing the Power Factor

The power factor is the Seebeck coefficient squared multiplied by the electrical conductivity ($S^2\sigma$). If its value is large, a large thermoelectric voltage and a high current can be generated.

The mechanism for the generation of the Seebeck effect in semiconductors is different from that in a metal because both the carrier concentration and the position of the Fermi level of a metal remain relatively unchanged with temperature. However, in semiconductors, since carriers in the hot end have more thermal energy than there in the cold end, hot carriers will diffuse from the hot end to the cold end. Thus, more carriers localise in the cold end, which forms an opposed electric field. If the material is in an open circuit, the rate at which carriers move from the hot to cold end caused by diffusion will be balanced by the rate at which carriers move from the cold to hot end owing to the electric field, thus equilibrium is reached. As a result an electrochemical potential will form with the appearance of a temperature difference between the two ends. This electrochemical potential is known as the Seebeck voltage, and the amount of voltage generated per unit temperature gradient is called the Seebeck coefficient[93].

To obtain a large Seebeck coefficient, there should only be one type of carrier (electrons or holes). Mixed n-type and p-type carrier systems will weaken the Seebeck voltage because of the enrichment of both charge carriers in the cold end. Thus $S_{total} = S_n+S_p$, where S_n is negative, and S_p is positive.

The Mott formula[94] for the Seebeck coefficient S is

$$S = \frac{\pi^2}{3}\frac{k_B^2 T}{e}\frac{dln\sigma(E)}{dE}\mid_{E=E_f} \qquad 2\text{-}17$$

where k_B is Boltzmann's constant, and e is the charge of an electron, σ (E) is the electrical conductivity determined as a function of the band filling or Fermi energy, E_f. If the electronic scattering is independent of energy, then σ (E) is proportional to the density of states (DOS) at E.

The interrelationship between carrier concentration and the Seebeck coefficient can be seen from relatively simple models of electron transport. According to a simple theory for nearly free electrons, the Seebeck coefficient is given by[95]:

$$S = \frac{8\pi^2 k_B^2}{3eh^2} m^* T \left(\frac{\pi}{3n}\right)^{2/3}\left[1+\left(\frac{dln\lambda_s}{dlnE}\right)_{E_f}\right] \qquad 2\text{-}18$$

where h is Planck's constant, n is the carrier concentration, and m* is the effective mass of the carrier, λ_s is the scattering distance. It has been shown that room temperature values of S vary as $n^{-2/3}$, as required by equation 2-17[96].

The electrical conductivity (σ) is related to n through the carrier mobility μ:

$$\sigma = ne\mu \qquad 2\text{-}19$$

$$\mu = \frac{e\tau}{m^*} \qquad 2\text{-}20$$

Using Eqs. 2-19 and 2-20 we can further define σ as:

$$\sigma = \frac{ne^2\tau}{m^*} \qquad 2\text{-}21$$

where e denotes electron charge and τ is the carrier lifetime. As temperature increases, τ decreases in a metal. By contrast, electrical conductivity in semiconductors correlates positively with temperature because their carrier density increases at a faster rate than the decrease of carrier mobility with increasing temperature.

The Seebeck coefficient is proportional to effective mass and inversely proportional to carrier concentration (equation 2-18) but electrical conductivity has the opposite trend (equation 2-21). Thus there should be a certain optimum balance between them, which relies on the carrier concentration, as can be seen from Figure 2.13. m* refers to effective mass, which increases with flat, narrow bands with high density of states at the Fermi surface. Thus, a balance must be found between effective mass and mobility for a high power factor. It is not obvious which effective mass is optimum. Good thermoelectric materials can be found within a wide range of effective mass and mobility[79].

Typically metals have high electrical mobility but small Seebeck coefficients because of half-filled bands caused by equal negative and positive charges cancelling each other when contributing to the induced thermoelectric voltage. However, large Seebeck coefficients have been observed in alloys and solid solutions of rare-earth elements known as “heavy fermion” systems[97]. Oxides have low mobility but high effective mass, implying that a generally applicable route to enhanced ZT is to deliberately engineer impurity-induced band-structure distortions[98]. Some semiconductors, such as SiGe, have high mobility but low effective mass[99].

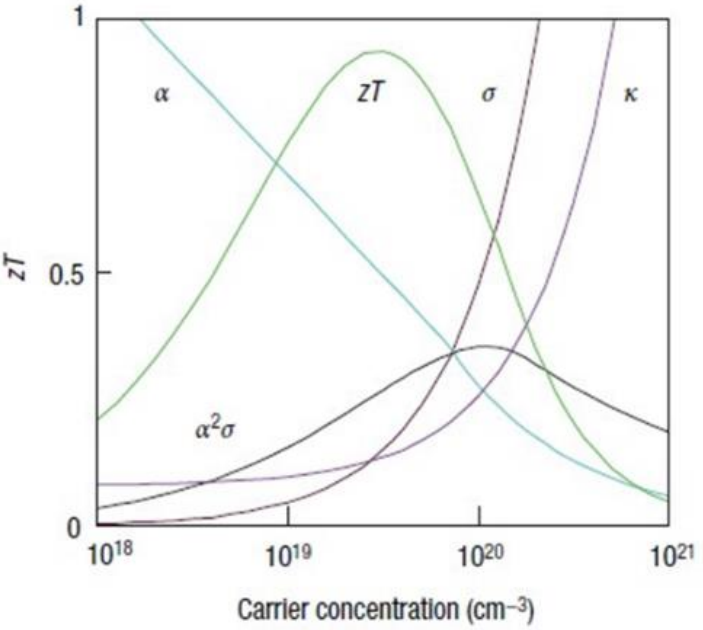

Figure 2.13 Optimising *ZT* through carrier concentration tuning: maximising the efficiency (*ZT*) of a thermoelectric involves a compromise between thermal conductivity (κ; plotted on the y axis from 0 to a top value of 10 W m^{-1} K^{-1}) and Seebeck coefficient (S; 0 to 500 µV K^{-1}) with electrical conductivity (σ; 0 to 5000 $\Omega^{-1}cm^{-1}$). Good thermoelectric materials are typically heavily doped semiconductors with a carrier concentrations between 10^{19} and 10^{21} carriers per cm^3 (79).

2.4.2 Lowering Thermal Conductivity

The thermal conductivity κ in thermoelectrics has two contributions; one from mobile electrons (κ_e) and another from phonons travelling through the lattice (κ_{kappa}). Thus, $\kappa = \kappa_e + \kappa_{kappa}$. Electron kinetic energy is transferred to the cold end by collisions with each other and with the atoms in the lattice. Phonons have a range of kinetic energies and the energy is transferred from the hot to cold end via phonon-phonon interactions. The thermal conductivity must be low to maintain a temperature difference across the material.

The Wiedemann-Franz law indicates that the ratio of the electronic part of the thermal conductivity κ to the electrical conductivity σ is constant at a given temperature according to the following relation[100]:

$$L = \frac{\kappa_e}{\sigma T} = \frac{\pi^2}{3}\left(\frac{k_B}{e}\right)^2 = 2.44 \times 10^{-8} W\Omega K^{-2} \qquad \text{2-22}$$

A good approximation for the lattice thermal conductivity has been offered by the classical kinetic theory:

$$\kappa_{latt} = \frac{C_v l v_s}{3} \qquad \text{2-23}$$

where C_v is the specific heat at constant volume, l is mean free phonon path, and v_s is the average velocity of sound.

At very low temperatures (under 40 K), the behavior of κ_{latt} is dominated by the Debye T^3 law for C_v. Phonon scattering is insignificant in this temperature range due to the low number of excited phonons and their very long lifetime. However, at high temperatures, that is, above the Debye temperature, C_v approaches the classical value of 3R, leading to the primary dependence of κ_{latt} on l which is determined by phonon-phonon scattering[101]. According to Keyes's expression[102] the lattice thermal conductivity is dominated primarily by phonon-phonon scattering (equation 2-24):

$$\kappa_{latt} T = \frac{R^{3/2}}{3\gamma^2\varepsilon^3 N_0^{1/3}} \frac{T_m^{3/2}\rho^{2/3}}{A^{7/6}} \qquad \text{2-24}$$

where R is the ideal gas constant, T_m is the melting point, ρ is the density, γ is the Grüneisen constant, ε is the fractional amplitude of interatomic thermal vibrations, N_o is Avogadro's number, and A is the mean atomic weight.

From the equations above, the parameters in equation 2-16 are determined by the details of the electronic structure and scattering of charge carriers (electrons or holes), and thus are not independently controllable. Therefore, the figure-of-merit (*ZT*) can be improved by manipulating the lattice thermal conductivity without decreasing the electrical conduction. Three successful strategies have been used to reduce the lattice thermal conductivity. The first one is to introduce point defects or rattling structures[103-106]. The second one is to engineer complex crystal structures to separate the electron-crystal from the phonon-glass, where the main purpose is to scatter phonons without significantly disrupting the electron-transport region[107-113]. A third strategy is to create nanostructures thus shortening the mean free path. These materials can be formed as superlattices (2D structures)[114], nanowires (1D structures)[115], quantum dots (0D structures)[116] and thin-film materials[117].

Although, obviously, there is a large specialised market for thermoelectrics far beyond the few applications discussed above, thermoelectric devices are not in wide spread use today because the main limitation is the low energy conversion efficiency relative to mechanical cycling.

2.5 Thermoelectric Materials Performance

The remarkable progress in the enhancement of the figure of merit ZT in recent years is shown in Figure 2.14. The largest figures of merit have been achieved with tellurium-, antimony- and germanium-based compounds[118-122]. A figure of merit of one or larger is generally considered to be needed for practical applications. Many different material systems exhibit enhanced figures of merit, and some of them have broken the $ZT \approx 1$ barrier which was the maximum ZT of any material for over fifty years[93].

2.5.1 Why Oxides?

The above materials are composed of toxic, naturally rare, and heavy elements and can be oxidised or melt at high temperatures in air. To overcome these limitations, novel TE materials with high ZT composed of nontoxic, naturally abundant, light, and cheap elements need to be developed. Oxide materials meeting these requirements are highly promising candidates from this point of view. If the durability can be improved and the cost decreased, oxide thermoelectric materials may be used in devices for harvesting energy from waste heat[123].

It should also be mentioned that there is great effort currently under way to solve engineering challenges related to creating thermoelectric devices, although that is not the focus of this review[124]. The objective here is to review the current status of oxide thermoelectric materials, including results from the literature on the thermoelectric properties of promising n-type and p-type oxide materials.

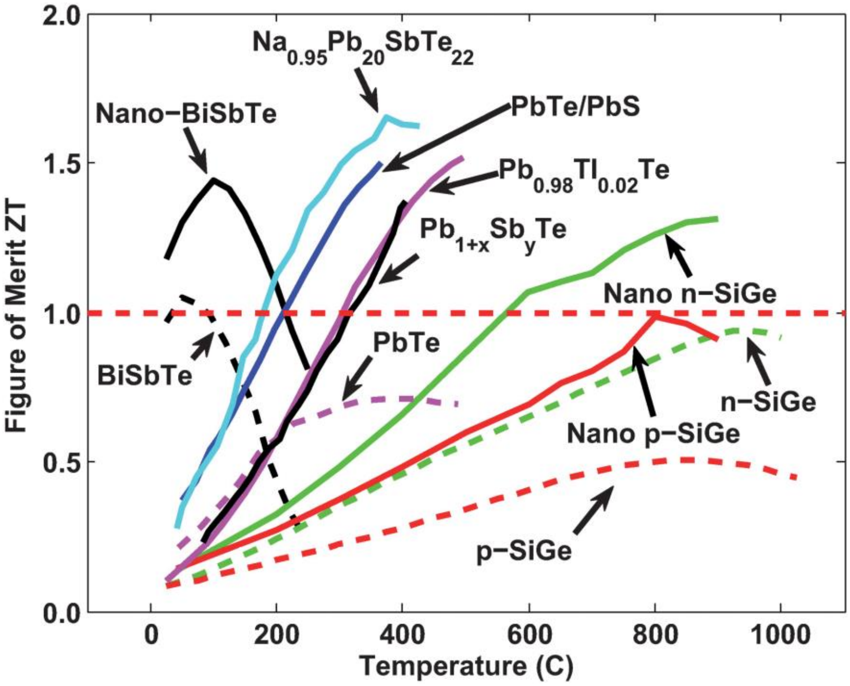

Figure 2.14 Figure of merit *ZT* of current state of the art thermoelectric materials versus temperature. The dashed lines show the maximum *ZT* values for bulk state of the art materials, and the solid lines show recently reported *ZT* values, many of which were obtained in bulk nanostructured materials (BiSbTe[125], $Na_{0.95}Pb_{20}SbTe_{22}$[126], PbTe/PbS[127], $Pb_{0.98}Tl_{0.02}Te$[98], $Pb_{1+x}Sb_yTe$[128], n-SiGe[129], p-SiGe[130]).

2.5.2 P-type oxides

As discussed above, the short mean free paths of layer-structured materials allow them to have low thermal conductivity due to phonon scattering at the interfaces between the layers. Moreover, drastic improvement of the thermoelectric performance was theoretically predicted for quantum-well cobaltite structures[131, 132]. The ternary and quaternary cobaltates have generated much excitement because of their high Seebeck coefficients and related high power factor coupled with a low thermal conductivity. The appeal of oxides for high-temperature thermoelectric power generation derives from their presumed high thermal and chemical stability in air. Therefore, cobalt oxides with layered crystal structures are drawing more attention.

The most promising p-type oxide thermoelectric materials are those based on alkali or alkaline-earth cobaltite compounds that are related to high-T_c superconductors and form layered structures[133]. These materials have large Seebeck coefficients, which are caused by a strong electron correlation due to spin fluctuation and the low spin state of Co^{3+}(134). There are two promising thermoelectric oxides, Na_xCoO_2[135-137] and $Ca_3Co_4O_9$[138-140]. In Na_xCoO_2, the CoO_2 layers are separated by a layer of sodium ions, while in $Ca_3Co_4O_9$, the CoO_2 planes are separated by a Ca_2CoO_3 layer that forms a rock salt-type structure, Figure 2.15.

As shown in Figure 2.15, Na_xCoO_2 adopts a hexagonal layered structure with edge-sharing 2D triangle CoO_2 sheets (“electron crystal”) to maintain electrical conductivity and highly disordered Na layers (“phonon glass”) alternately stacked along the c-axis to scatter phonons. Variations in cobalt valence, as evidenced by the changes in oxygen content, have been reported to affect the thermoelectric properties of $Ca_3Co_4O_9$[141]. The CoO_2 planes of this structure provide a path for p-type carriers (holes), while lattice phonons disrupt heat transfer between the layers and the other structural components.

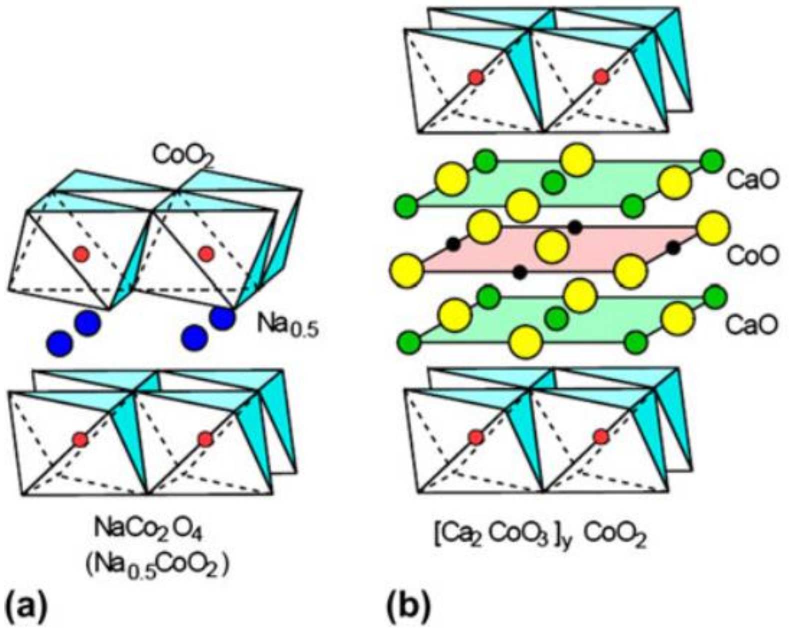

Figure 2.15 Schematic illustration of the crystal structure of CoO_2-based TE oxides: (a) Na_xCoO_2, (b) a Ca-based Co oxide known as $Ca_3Co_4O_9$[108].

Na_xCoO_2

One of the most important layered cobaltite-based thermoelectric materials is Na_xCoO_2. The sodium content differs between reports and the transport properties are affected by the concentration of sodium ions[108]. However, good thermoelectric properties are observed near $x = 0.55 - 0.70$ (the γ phase, $NaCo_2O_4$) It belongs to a bronze-type compound expressed as A_xBO_2 ($0.50 < x < 1.00$), which was first identified by Jansen and Hoppe[142].

The first report of a large Seebeck coefficient in $NaCo_2O_4$ attracted extensive attention on layered cobalt oxides. The conductivity and Seebeck coefficient of $NaCo_2O_4$ single crystals reach 5000 S cm^{-1} and 100 μV/K at 300 K, which is about ten times larger than in typical metals, consequently a large power factor of 50 μW cm^{-1} K^{-2} at 300 K. In $NaCo_2O_4$, the in-plane resistivity ρ of 200 μΩ cm at 300 K decreases in a metallic-like fashion with decreasing temperature down to 1.5 K. This is as conductive as the superconducting Cu oxides, meaning that the layered Co oxide is one of the most promising conductive layered oxides for thermoelectric materials. However, it has low mobility (13 cm^2/V s at 300 K), which is strikingly against the common sense that dirty conductors are not suitable for thermoelectric materials[143]. It also indicates that good thermoelectric materials will be found in semiconductors with low mobility but high effective mass and carrier concentration. The proposed origin of the unusually large Seebeck coefficient of $NaCo_2O_4$ is an magnetic entropy of k_B ln6, which is equivalent to 150 μV/K at the high temperature limit and agrees with the experiment satisfactorily, and is caused by the low-spin state of Co^{4+} in the background of the low-spin state Co^{3+} ions of zero entropy[134]. The high $ZT \approx 0.8$ at 1000 K from a polycrystalline sample[144] and $ZT > 1$ at 800 K from a single-crystal sample[145] have been reported.

In recent years, copper[146] and zinc[147] additions to Na_xCoO_2 have been shown to increase the electrical conductivity and Seebeck coefficient. The value of the Seebeck coefficient for $Na(Co_{0.95}Zn_{0.05})_2O_4$ at 1073 K is 415 μV/K, which is twice as large as that of ZnO-free $NaCo_2O_4$[147].

$Ca_3Co_4O_9$

Due to the great interest in p-type Na_xCoO_2, many cobaltites with hexagonal CoO_2 layers that are structurally similar to that of Na_xCoO_2 have been investigated. Promising p-type thermoelectric properties have since been found in $Ca_3Co_4O_9$ compounds[148, 149].

In these oxides, a common feature is an electronic transport pathway in the presence of CdI_2-type two-dimensional hexagonal CoO_2 layers consisting of edge sharing CoO_6 octahedra, accompanied by low thermal conductivity caused by sodium ion blocking layers or calcium cobalt oxide misfit layers. However, $Ca_3Co_4O_9$ has CaO, CoO and CaO triple rock salt layers instead of the Na layers, thus the chemical formula is $[Ca_2CoO_3]_yCoO_2$ ($y \approx 0.62$). Only the b-axis length is incommensurate between the adjacent sheets due to a peculiar lattice misfit that is attributed to hexagonal CoO_2 layers interleaved with rectangular rock salt layers[97].

The thermoelectric properties of $Ca_3Co_4O_9$ measured on whiskers (ribbon-like single crystals) of 50 - 200 μm width along the in-plane direction exhibited the largest ZT = 1.2 - 2.7 at 873 K[150]. The various results are fairly consistent with a conductivity of ~104 S m^{-1}, a Seebeck coefficient of ~150 μV/K and a thermal conductivity of ~2 W K^{-1} m^{-1}. The entropy is zero for the Co^{3+} ion due to its triply degenerate t_{2g} state. But Co^{4+} is different, because it has one less electron than Co^{3+}, which causes a degeneracy of six (two from spin, three from orbital). As a result, the Co^{4+} ion induces a large entropy of k_B ln6. So the transport entropy, entropy per charge, is estimated to be k_B ln6/|e| = 150 μV/K, which is roughly equal to the Seebeck coefficient of $Ca_3Co_4O_9$ at high temperatures.

Bismuth is usually used to dope $Ca_3Co_4O_9$ and has been shown to increase the electrical conductivity and Seebeck coefficient simultaneously as well as decrease the thermal conductivity[151, 152]. The decrease of thermal conductivity is due to the enhancement of phonon scattering caused by the larger size and mass of bismuth as compared to calcium. The increase in conductivity is attributed to an increase in carrier mobility rather than carrier concentration. Bi^{3+} changes the energy dependence of mobility and thus leads to an increase in *S*.

Ag enhances the ZT of $Ca_3Co_4O_9$ either as a substituent for Ca or as a second (metallic) phase.[153] Ag^+ at the Ca site is considered to increase the carrier concentration and mobility, resulting in an increase in the Seebeck coefficient whereas Ag and Ag^+ can enhance the power factor[154]. The large mass of Ag also leads to a decrease in the thermal conductivity[154, 155].

Partial substitution of Cu for Co in $Ca_3Co_4O_9$ is consistently reported to increase the electrical conductivity mainly because of the rise in hole concentration but also due to a decrease in the Seebeck coefficient[156, 157]. Other transition metal dopants, such as Fe and Mn, occupy Co sites in the CoO_2 layer.

Although there are reports of an increase in electrical conductivity due to doping of iron or nickel, in most cases the beneficial effect of transition metal dopants is an increase in Seebeck coefficient, rather than an increase in electrical conductivity. For example, electrical conductivity is significantly increased by the partial substitution of Na at the Ca site without the degradation of *S*, but the Seebeck coefficient decreases in the case of Mn, Cu and Na substitutions[157].

Although $Sr_3Co_4O_9$ has a lower conductivity than $Ca_3Co_4O_9$, a small concentration of Sr substitution in $Ca_3Co_4O_9$ does not significantly affect the electrical conductivity but leads to a decrease in thermal conductivity and thus a small increase in the figure of merit[158].

Strong anisotropy in the properties and the crystal growth leads to the performance of bulk ceramic samples several times lower than that of single crystals. Further improvement in processing techniques is anticipated to transfer the outstanding thermoelectric performance of the single crystals to bulk polycrystalline ceramics.

2.5.3 N-type oxides

$CaMnO_3$

It is known that $CaMnO_3$ (space group Pnma) has the perovskite structure with a = 0.5282 nm, b = 0.7457 nm, and c = 0.5267 nm[159]. The ZT of undoped $CaMnO_3$ is less than 0.04 at 900 K with electrical conductivity of ~10 S/cm[160]. However, $CaMnO_3$ is still a promising n-type oxide thermoelectric owing to its large absolute Seebeck coefficient ($|S| > 300$ μV/K). Appropriate substitutions at the A- or B-site can increase electrical conductivity and lower thermal conductivity to enhance the ZT value. Thus far, the thermoelectric properties of doped $CaMnO_3$ have been investigated extensively up to 1000

K[161-164].

A-site substitution with rare earth elements has proven to be beneficial in increasing the electrical conductivity of $CaMnO_3$. Ohtaki *et al.* have studied the high temperature performance of $CaMnO_3$ with a series of A-site dopants (Y, La, Ce, Sm, In, Sn, Sb, Pb and Bi)[161]. The maximum ZT value (0.085) was found in a 10 at. % Bi-doped sample at 900 ℃. Thao *et al*. have shown the highest ZT value of 0.20 for $Ca_{0.8}Dy_{0.2}MnO_{2.98}$ at 1273 K[162]. The $Ca_{1-x}Re_xMnO_3$ system with Nd, Tb, Ho and Yb doped on the A-site has also achieved high ZT enhancement. The electrical conductivity increases along with a decrease in thermal conductivity from Nd to Yb substitution because of the heavier elements creating stronger local vibrations in the lattice that suppress the thermal conductivity. Therefore, Yb substituted compounds have reached a ZT of 0.16 at 1000 K[164]. Subsequently, $Ca_{1-x}Yb_xMnO_3$ (x = 0.00 - 0.50) was studied by Flahaut *et al.* based on the above facts. The best ZT value of 0.20 was obtained for $Ca_{0.95}Yb_{0.05}MnO_3$ at 1000 K in that work. The results show that the enhanced octahedral distortion with Yb content leads to the reduction of Mn-O-Mn bond angles. The shift of the degree of hybridisation between the Mn 3d e_g and O 2p σ states narrows the conduction bandwidth to some extent. Consequently, the Seebeck coefficient depends only on the charge carrier concentration while the electrical conductivity is affected not only by the charge carrier concentration but also by the octahedral distortion. The thermal conductivity is mainly governed by the octahedral distortion and the mass difference. Furthermore, in $Ca_{0.9}R_{0.1}MnO_3$ (R = La, Pr, Nd, Sm, Eu, Gd, Tb, Dy, Ho, Er and Yb) ceramics, the size mismatch between the Ca^{2+} and R^{3+} ions, as the content of R ions increases, has been regarded as another source of the increasingly anharmonic lattice vibrations that suppress the phonon transport[165]. For all the compounds above, the Seebeck coefficient is related only to carrier concentration as shown in Figure 2.16[166], but the electrical conductivity also depends on the effective bandwidth that reduces with the smaller average (R, Ca) site ionic radii. The largest ZT values have been obtained in $Ca_{0.9}Dy_{0.1}MnO_3$

and $Ca_{0.9}Yb_{0.1}MnO_3$ at 1000 K, as presented in Figure 2.17[165].

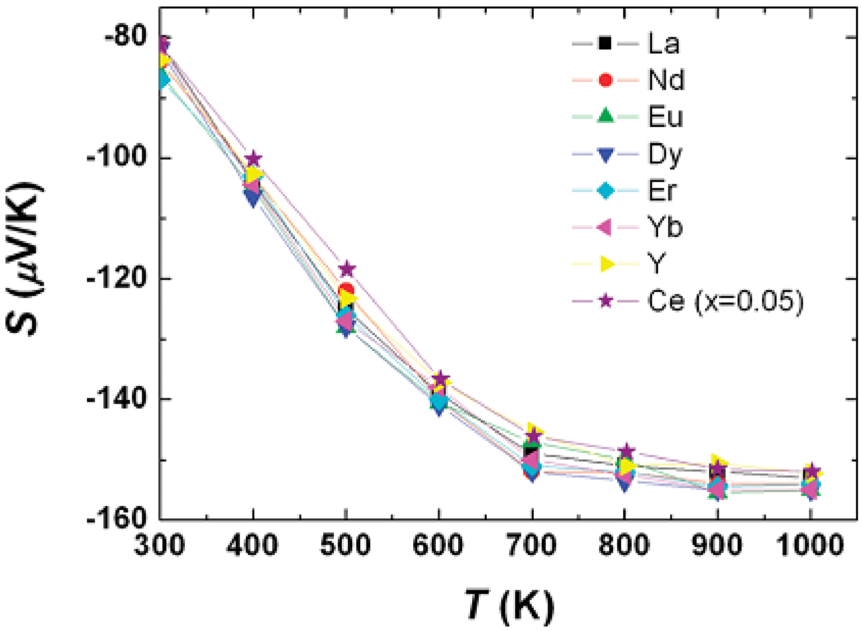

Figure 2.16 Temperature dependence of S for $Ca_{0.9}R_{0.1}MnO_3$ samples (S of $Ca_{0.95}Ce_{0.05}MnO_3$ is also shown)[166].

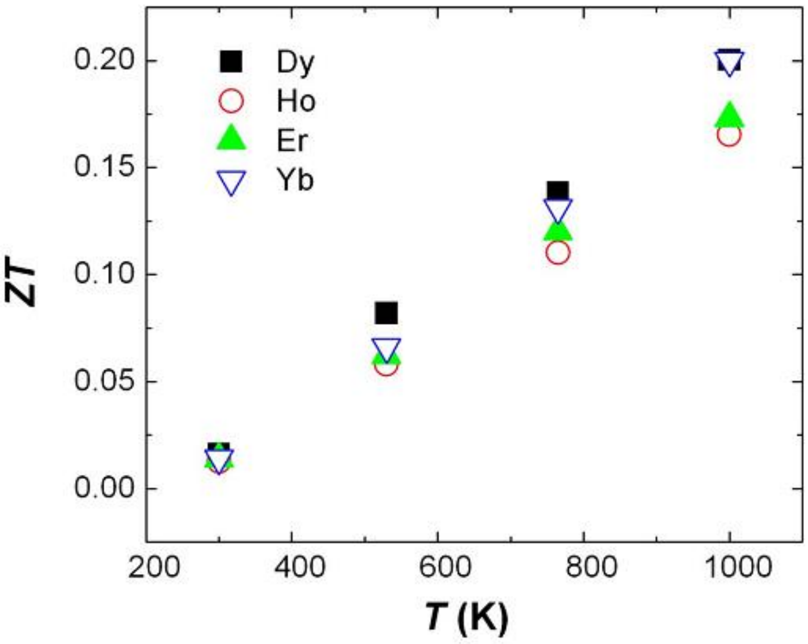

Figure 2.17 Temperature dependence of ZT values for $Ca_{0.9}R_{0.1}MnO_3$ (R=Dy, Ho, Er and Yb)[165].

B-site substitution has fewer options on account of the smaller space for small ions with high valence. The introduction of higher valence ions on the B-site results in the reduction of Mn^{4+} to Mn^{3+}, which corresponds to n-type conduction. As Mn^{3+} is stable at high temperature in air, doped $CaMnO_3$ can be applied as a potential n-type material up to very high-temperature. Pi *et al.* have studied Ru and Mo doped $CaMnO_3$ at low T. However, the ZT values are less than 0.015[167]. An enhanced ZT value of 0.08 was achieved at 1000 K in 4 at. % Nb-doped $CaMnO_3$[163]. Niobium substitution increases the electrical conductivity and decreases the Seebeck coefficient and thermal conductivity. This trend was also observed in Ta-doped $CaMnO_3$. Subsequently, Bocher *et al.* reported the thermoelectric properties of $CaMn_{1-x}Nb_xO_3$ (with x = 0.02, 0.05, 0.08 and 0.10) obtained by applying soft chemistry (SC) synthesis and the solid state reaction (SSR) method. They found that the SC compounds, exhibit dramatically lower thermal conductivity (< 1 W m^{-1} K^{-1}) than the SSR compounds probably owing to the nanosized twinned domains in the SC phases. The SC compounds also reveal higher electrical conductivity than the SSR compounds. The ZT values for both sets of compounds are presented in Figure 2.18[168].

Lan *et al.* also compared the thermoelectric performance of $Ca_{1-x}Gd_xMnO_3$ (x = 0.02, 0.04, and 0.06) by chemical co-precipitation and solid state reaction method. The results indicate that a decrease in grain size dramatically reduces thermal conductivity. A highest ZT of 0.24 has been achieved for $Ca_{0.96}Gd_{0.04}MnO_3$ at 973 K in air[169].

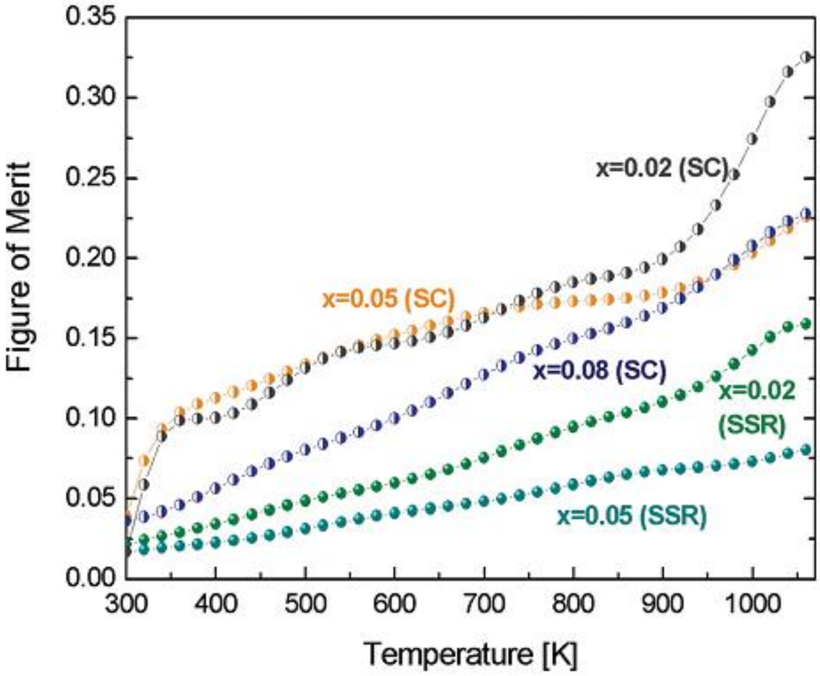

Figure 2.18 Temperature dependence of the figure of merit for $CaMn_{1-x}Nb_xO_3$ (for x = 0.02, 0.05 and 0.08) synthesised by both SSR (closed symbols) and SC (open symbols) methods[168].

As discussed above, the highest thermoelectric performance was obtained in 10 at. % Yb doped and 2 at. % Nb doped $CaMnO_3$. Recently, Kabir *et al.* have been trying to improve the thermoelectric properties via codoping. The ZT values for Yb-doped $CaMn_{0.98}Nb_{0.02}O_3$ are shown in Figure 2.19[170]. The highest ZT value of 0.13 was achieved for $Ca_{0.95}Yb_{0.05}Mn_{0.98}Nb_{0.02}O_3$ at 973 K, which is somewhat lower than the ZT value of 0.20 obtained for single doped samples.

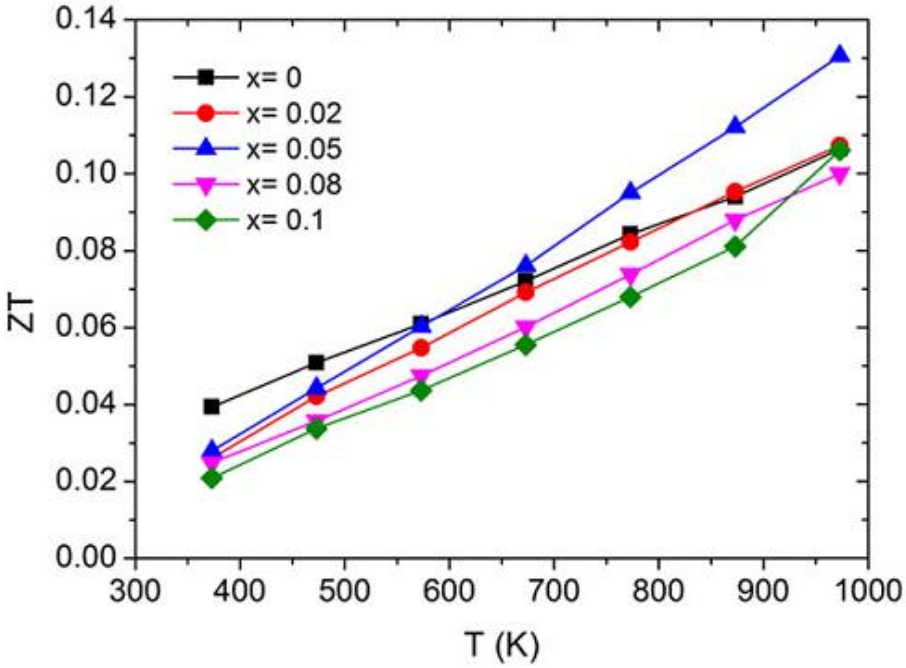

Figure 2.19 The temperature dependence of the thermoelectric figure of merit (ZT) for $Ca_{1-}xYb_xMn_{0.98}Nb_{0.02}O_3$ (x = 0.00, 0.02, 0.05, 0.08 and 0.10)[170].

ZnO

ZnO has the wurtzite structure at ambient conditions as shown in Figure 2.20. It is an n-type semiconducting oxide with a wide band gap of 3.3 eV and is a promising n-type thermoelectric material. The mobility of electrons is high in ZnO due to its conduction band consisting of the lowest unoccupied 4s and 4p orbitals of the Zn^{2+} ion. The covalent character of the Zn-O bond also increases the carrier mobility in the structure. The main disadvantage of ZnO for thermoelectrics is its high thermal conductivity on account of its hexagonal structure.

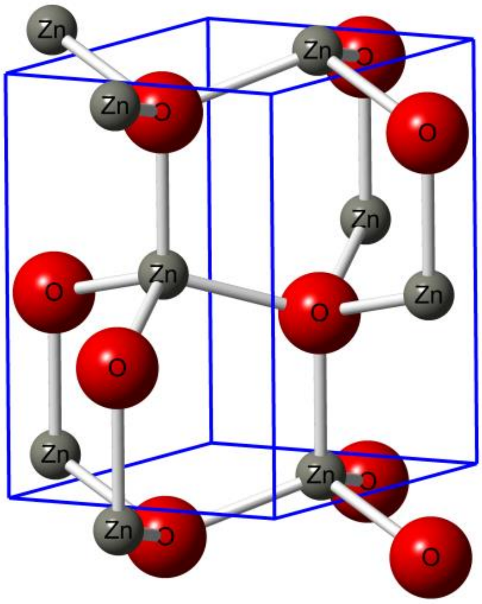

Figure 2.20 The crystal structure of ZnO (Wurtzite).

The best ZT values reported for n-type ZnO-based oxides are 0.47 at 1000 K and 0.65 at 1247 K, as obtained by Ohtaki *et al.* in $Zn_{0.96}Al_{0.02}Ga_{0.02}O$ and shown in Figure 2.21[171]. In the 1990s, Ohtaki *et al.* focused on $(Zn_{1-x}Al_x)O$ (x = 0.00 - 0.10) thermoelectric oxides for the first time and gained a ZT value of 0.30 at 1000 ℃[172]. This gave considerable encouragement to consider ZnO-based oxides as novel n-type thermoelectric materials. Kim *et al.* increased the ZT value of Al and Ni co-doped ZnO dramatically, producing the largest reported value of 0.70 at 900 ℃[173]. Park *et al.* have studied some co-doped systems, such as $Zn_{1-x-y}Al_xTi_yO$ and $Zn_{1-x-y}Sb_xSn_yO$ ceramics[174, 175]. $Zn_{0.97}Al_{0.02}Ti_{0.01}O$ exhibits the highest power factor value (3.8×10^{-4} W m^{-1} K^{-2}) at 800 ℃ for the Al, Ti co-doped series, whereas $Zn_{0.985}Sb_{0.005}Sn_{0.01}O$ shows an even higher value of 1.15×10^{-3} W m^{-1} K^{-2} at 800 ℃ for the Sb, Sn co-doped series. Subsequently, Yamaguchi *et al.* shed light on the thermoelectric properties of transition metal (Fe, Ni, and Sm) and Al co-doped ZnO ceramics. The ZT value for $Zn_{0.96}Al_{0.02}Ni_{0.02}O$ reaches 0.126 at 800 ℃[176]. The spark plasma sintering (SPS) process with hydroxide raw materials was used to improve the electrical conductivity and gain fine grains to lower the thermal conductivity for Al-doped ZnO with a 4 at. % Al doped-ZnO displaying the highest ZT of 0.085 at 400 ℃[177]. However, a small grain size is potentially prone to impair the ZT value because it decreases the electrical conductivity[178]. It is now well known that aluminium is helpful to improve the ZT of ZnO owing to the decrease of the c/a ratio of the unit cell. Heavy doping to suppress the c/a ratio could be crucial to enhance ZT[179]. Recently, thermoelectric Al-doped ZnO thin films deposited by pulsed laser deposition (PLD), radio frequency (RF) and pulsed direct current (DC) magnetron sputtering have been exploited. Thin film power factors of 0.55×10^{-3} W m^{-1} K^{-2} (on single crystal substrates) and 1.2×10^{-3} W m^{-1} K^{-2} (on amorphous substrates) have been obtained for 2 at. % Al-doped ZnO at 600 K[180, 181].

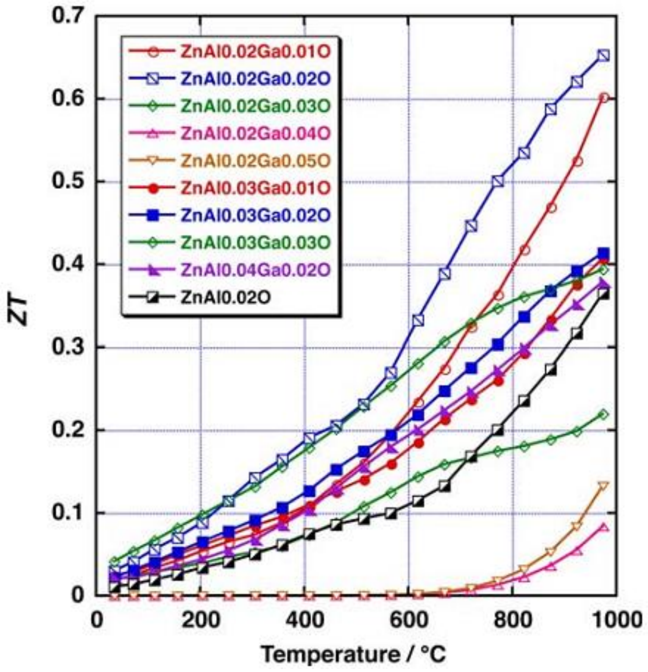

Figure 2.21 Temperature dependence of the dimensionless figure-of-merit ZT for Zn$_{1-x-y}$Al$_x$Ga$_y$O ($0.02 \le x \le 0.04$, $0 \le y \le 0.05$) ceramics.

$SrTiO_3$ and $Sr_3Ti_2O_7$

Strontium titanate, with the simple cubic perovskite structure is another potential n-type thermoelectric material based on its prominent electrical conductivity by doping higher valence ions on the A- and B-site. For example $SrTiO_3$ heavily doped with La^{3+} and Nb^{5+} have a ZT of 0.26[182] and 0.37[183] at 1000 K, respectively. Overall, the electrical conductivity and Seebeck coefficient are high enough to compete with that of conventional thermoelectric materials.

In 2001, the thermoelectric properties of $Sr_{1-x}La_xTiO_3$ single crystals ($0.00 < x < 0.10$) prepared by the floating-zone method were reported by Okuda *et al.*[184]. Large power factors of 2.8 to 3.6×10^{-3} W m^{-1} K^{-2} with high carrier density of (0.2 - 2.0) $\times10^{21}$ cm^{-3} at room temperature were reported. Muta *et al.* found that reduced single-crystalline $SrTiO_3$ measured along the [100] axis has a similar ZT value to that of 5 at. % La doped $SrTiO_3$, as shown in Figure 2.22[185]. Moreover, Ohta *et al.* compared La-doped STO single crystals with Nb-doped STO single crystals and demonstrated that even if the largest ZT of 0.27 was attained in La-doped STO at 1073 K, the carrier effective mass m* of Nb-STO is larger than that of La-STO[182]. Research on heavily carrier-doped $SrTiO_3$ single crystals is an interesting avenue to explore the potential of a new n-type oxide thermoelectric oxide.

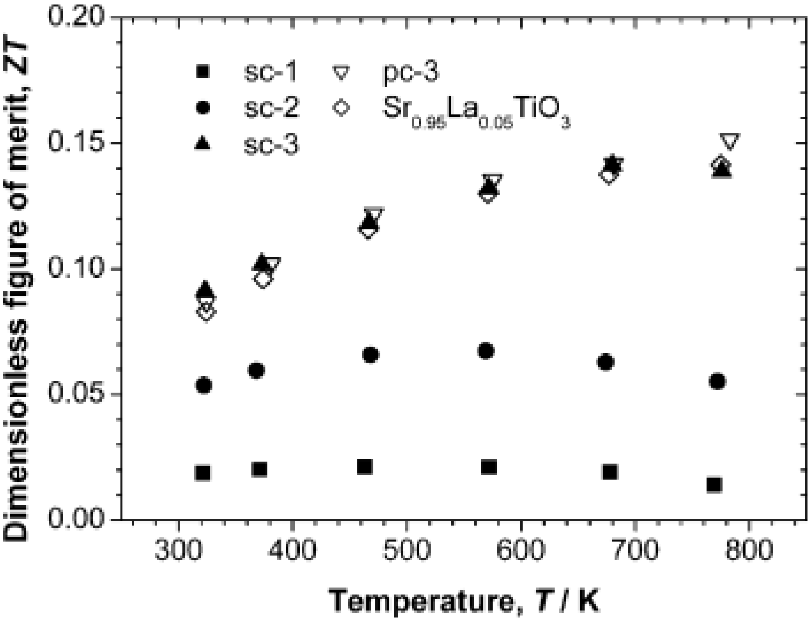

Figure 2.22 Temperature dependence of ZT for various $SrTiO_3$-based samples[185].

Aimed at increasing the solubility of the Nb content in the $SrTiO_3$ lattice to optimise the ZT value, epitaxial films of a series of Nb-doped $SrTiO_3$ (up to 40 at. % Nb-doping) have been grown on (100) oriented $LaAlO_3$ single-crystalline substrates at 700 ℃ by pulsed laser deposition (PLD). Thus, Ohta *et al.* obtained a ZT of 0.37 at 1000 K in 20 at. % Nb-doped STO with a carrier density of 4×10^{21} cm^{-3} with this being the highest value so far reported in $SrTiO_3$-based thermoelectrics, as presented in Figure 2.23[183]. Kato *et al.* attempted to further reduce thermal conductivity by isovalent substitution of Eu^{2+} for Sr^{2+} in $Sr_{1-x}Eu_xTi_{0.8}Nb_{0.2}O_3$ (x = 0.00~0.80) epitaxial films. The Seebeck coefficient and electrical conductivity were both found to be independent of the Eu content. Although the mean free path of the phonon shortened by 12% at 300 K there was no significant reduction at high temperature, revealing that Eu-substitution is beneficial to $SrTi_{0.8}Nb_{0.2}O_3$ only at low temperature[186]. However, oxygen-deficiency has been proven to reduce the thermal conductivity significantly in $Sr_{1-x}La_xTiO_{3-\delta}$ films prepared using

PLD under a high vacuum of ~10^{-7} Torr as compared to unreduced strontium titanates[187, 188]. This result suggests that the introduction of oxygen vacancies and point defects from film growth processes could offer more effective phonon-scattering centres to suppress the thermal conductivity. In 2010, the combined influence of La doping and oxygen reduction (δ) in $SrTiO_3$ epitaxial films was measured from 300 to 900 K. The thermal conductivity of all samples varied from ~5 W m^{-1} K^{-1} at 300 K to ~3 W m^{-1} K^{-1} at 873 K, maybe as a result of different dominating factors that can influence thermal conductivity, i.e. defects at low temperature compared to Umklapp scattering at high temperature[189]. The highest ZT of 0.28 was attained for $Sr_{0.85}La_{0.15}TiO_{3-\delta}$ at 873 K.

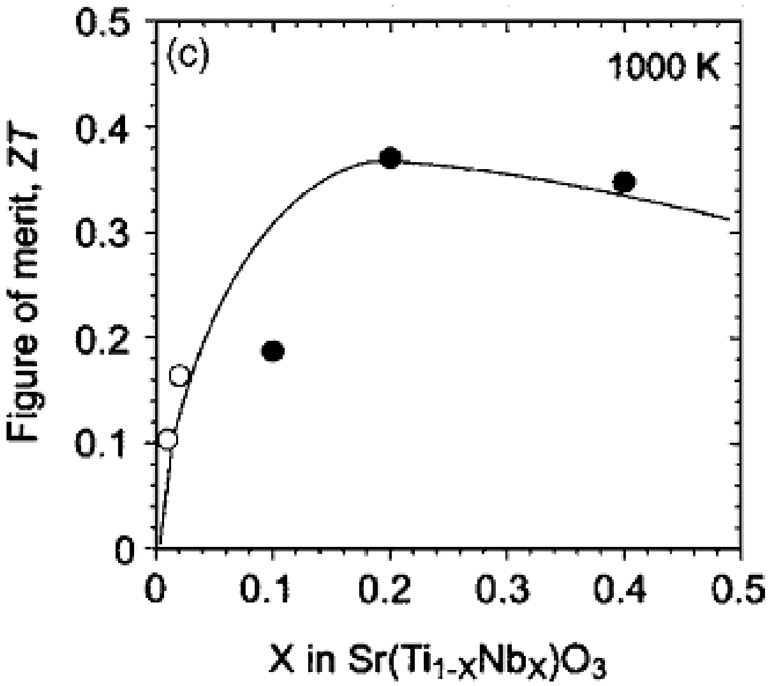

Figure 2.23 ZT versus Nb-content for Nb-doped $SrTiO_3$ epitaxial films at 1000 K[183].

Although high ZT values have been achieved in STO single crystals and epitaxial films, polycrystalline ceramics are indispensable for low cost, high volume applications. In 2003, an investigation on polycrystalline samples of $Sr_{1-x}RE_xTiO_3$ (x = 0.05 - 0.20, RE = Y, La, Sm, Gd and Dy) was conducted. It demonstrated both the Seebeck coefficient and electrical conductivity to be independent of the rare earth dopant so that the highest ZT value of 0.22 at 573 K was observed for Dy doped $SrTiO_3$ which had the lowest thermal conductivity[190]. Moreover, Ohta *et al.* extended their research from single crystals and epitaxial films to ceramics for 20 at. % Nb doped $SrTiO_3$. The results illustrated that single-crystalline film, polycrystalline film and ceramic samples exhibit similar ZT values at high temperature, Figure 2.24[191]. This suggests that the grain boundary contribution of ceramic samples to lower thermal conductivity is not enough to offset the decrease of electrical conductivity at low temperature. 10 at. % Ni and 10 at. % Ta doping on the A-site and B-sites, respectively gave ZT of 0.28[192] at 873 K and 0.17[193] at 752 K. This suggests that La^{3+} and Nb^{5+} remain the best dopants for $SrTiO_3$ thermoelectric ceramics to date. Liu *et al.* tried to improve the ZT of oxygen-deficient La-doped $SrTiO_3$. They attained a maximum ZT value of 0.21[194] for $Sr_{0.9}La_{0.1}TiO_{3-\delta}$ at ~750 K and about 0.2[195] at ~700 K for $Sr_{0.95}La_{0.05}TiO_{3-\delta}$ by employing forming gas (5 mol% hydrogen in argon) and introducing TiO_2 (rutile).

Recently, researchers have tried to exploit new synthetic techniques and strategies to improve the thermoelectric properties of doped $SrTiO_3$. Okinaka *et al.* have adopted combustion synthesis and spark plasma sintering (SPS) to fabricate rare-earth-doped (La, Sm, Gd, Dy and Y) $SrTiO_3$ and obtained a maximum ZT of 0.22 at 800 K from a $Sr_{0.92}La_{0.08}TiO_3$ sample[196]. Wang *et al.* have investigated Nb-doped $SrTiO_3$ with additions of mesoporous silica (MS)[197], titanate nanotubes (TNT)[198] and YSZ[199], respectively based on the strategy of increasing the scattering centres to reduce the thermal conductivity. In 2011, a comparable high ZT of 0.36 was reported for $La_{0.08}Dy_{0.12}Sr_{0.8}TiO_3$ with a small amount of $Dy_2Ti_2O_7$ as a secondary phase, which is an encouraging result albeit for a multi-phase sample[200].

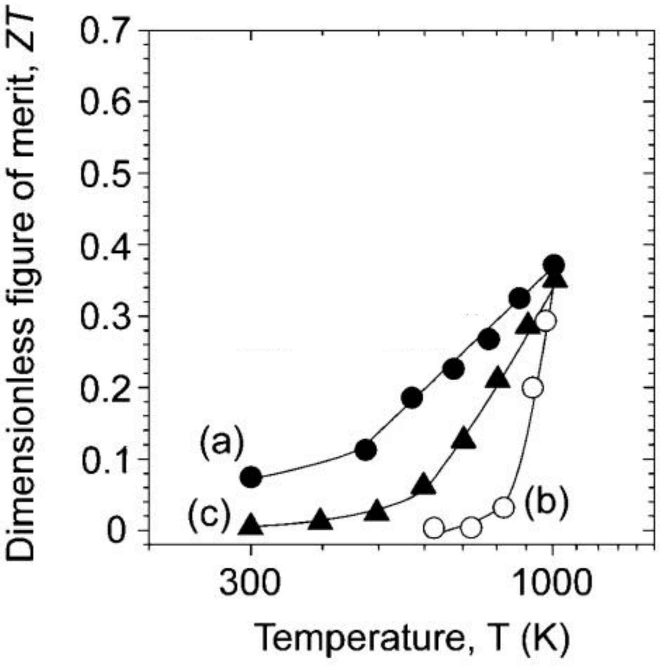

Figure 2.24 Temperature dependence of thermoelectric figure of merit (ZT) of $Sr(Ti_{0.8}Nb_{0.2})O_3$ samples[191]: (a) epitaxial film on (100)-$LaAlO_3$, (b) polycrystalline film on SiO_2 glass and (c) ceramic.

It is well known that the total thermal conductivity increases with the increase of the electrical conductivity according to the Wiedemann-Franz law. In order to further improve the power factor without increasing thermal conductivity, quantum-well (QW) structures have been employed to increase the Seebeck coefficient by restricting carrier electrons in a narrow space rather than varying the carrier concentration. Ohta *et al.* have succeeded in confining the carrier concentrations ($\sim10^{21}$ cm^{-3}) within a several unit cell thickness of $SrTiO_3$ (1.56 nm) in superlattices composed of 20 at. % Nb-doped $SrTiO_3$ interleaved in undoped $SrTiO_3$. This two-dimensional electron gas (2DEG) system exhibited an extremely high ZT of ~2.4 at 300 K for the $SrTi_{0.8}Nb_{0.2}O_3$ layer with the highest $|S|$ of ~480 μVK^{-1} at room temperature[201].

Although $SrTiO_3$ ceramics have high Seebeck coefficient and electrical conductivity, they also have high thermal conductivity (10 W m^{-1} K^{-1} at 300 K) due to the lack of effective phonon-scattering centres in the cubic perovskite structure, even with cation dopants acting as point defects. One effective way to decrease the thermal conductivity of STO is to engineer a superlattice structure[202]. A complicated structure will shorten the mean free path and so promote lower thermal conductivity. This can be achieved by exploring Ruddlesden-Popper (RP) phases as opposed to cubic perovskites. It can be envisaged that the perovskite layers of doped and reduced Ruddlesden-Popper phases should have a high conductivity without significantly suppressing the Seebeck coefficient but that disruption of the octahedral phonon modes across successive blocks separated by rock salt layers will reduce thermal conductivity compared with conventional ABO_3 perovskites. Based on the highest ZT obtained in Nb-doped $SrTiO_3$, the thermoelectric properties of Ruddlesden-Popper phases have been studied for Nb-doped compounds by Lee *et al.*, who found a highest ZT of 0.14 at 1000 K for $Sr_3Ti_{1.9}Nb_{0.1}O_7$[203]. They extended their research to A-site doped Ruddlesden-Popper phases and reported a ZT of 0.15 at 1000 K for 5 at. % La-doped $Sr_3Ti_2O_7$[204, 205]. Finally, they achieved a maximum ZT (~0.24 at 1000 K) in $(Sr_{0.95}Gd_{0.05})_3Ti_2O_7$[206, 207] and suggested that rare earth-doping is conducive to Seebeck coefficient enhancement due to its improvement of the local symmetry of the TiO_6 octahedra. Compared with $SrTiO_3$, however, the lower electrical conductivity resulting from the insulating rock-salt layers has been hypothesised to be the main obstacle to the development of good thermoelectric properties in Ruddlesden-Popper phases.

2.6 The Aim of This Project

This project aims to investigate the structure-composition-property relations of La-doped $SrTiO_3$ based thermoelectrics and related layered-perovskite compounds, with particular interest in understanding the effect of defect chemistry on the thermoelectric properties of La-doped $SrTiO_3$

and $Sr_3Ti_2O_7$. Although the defect chemistry of $SrTiO_3$ based materials has been extensively studied, there is still no research on how to apply defect chemistry models to improve thermoelectric properties of La-doped $SrTiO_3$ and related systems. Therefore, we aim to compare the thermoelectric properties of stoichiometric and non-stoichiometric La-doped $SrTiO_3$ and $Sr_3Ti_2O_7$ ceramics prepared in different atmospheres using different compensation mechanisms to optimise this class of promising n-type thermoelectric oxides.

Reference

1 M. Tegze and G. Faigel, Nature 380, 49 (1996).

2 S. N. Ruddlesden and P. Popper, Acta Crystallographica 10, 538 (1957).

3 S. N. Ruddlesden and P. Popper, Acta Crystallographica 11, 54 (1958).

4 R. K. Banyal and B. R. Prasad, Journal of Applied Physics 93, 9466 (2003).

5 Y. W. Cho, T. S. Hyun and S. K. Choi, Journal of Electroceramics 13, 251 (2004).

6 K.-I. Park, S. Xu, Y. Liu, G.-T. Hwang, S.-J. L. Kang, Z. L. Wang and K. J. Lee, Nano letters 10, 4939 (2010).

7 G. Yang, Z. Yue, J. Zhao, H. Wen, X. Wang and L. Li, Journal of Physics D: Applied Physics 39, 3702 (2006).

8 O. Guillon, J. Chang, S. Schaab, S.-J. L. Kang and C. A. Randall, Journal of the American Ceramic Society 95, 2277 (2012).

9 J.-Y. Hong, H.-Y. Lu and C. Alan Randall, Journal of the American Ceramic Society 97, 2256 (2014).

10 Z. Yan, Y. Guo, G. Zhang and J. M. Liu, Advanced Materials 23, 1351 (2011).

11 J. An, T. Usui, M. Logar, J. Park, D. Thian, S. Kim, K. Kim and F. B. Prinz, ACS Applied Materials & Interfaces 6, 10656 (2014).

12 L. Huang, Z. Chen, J. D. Wilson, S. Banerjee, R. D. Robinson, I. P. Herman, R. Laibowitz and S. O'Brien, Journal of Applied Physics 100, 034316 (2006).

13 T.-C. Huang, M.-T. Wang, H.-S. Sheu and W.-F. Hsieh, Journal of Physics: Condensed Matter 19, 476212 (2007).

14 R. Blinc, Structure and Bonding 124, 51 (2007).

15 G. H. Kwei, A. C. Lawson, S. J. L. Billinge and S.-W. Cheong, The Journal of Physical Chemistry 97, 2368 (1993).

16 Q. Zhang, T. Cagin and W. A. Goddard, Proceedings of the National Academy of Sciences of the United States of America 103, 14695 (2006).

17 M. B. Smith, K. Page, T. Siegrist, P. L. Redmond, E. C. Walter, R. Seshadri, L. E. Brus and M. L. Steigerwald, Journal of the American Chemical Society 130, 6955 (2008).

18 M. Minnekaev, K. Bulakh, A. Chouprik, W. Drube, P. Ershov, Y. Lebedinskii, K. Maksimova and A. Zenkevich, Microelectronic Engineering 109, 227 (2013).

19 N.-H. Chan and D. M. Smyth, Journal of The Electrochemical Society 123, 1584 (1976).

20 N.-H. Chan, R. K. Sharma and D. M. Smyth, Journal of the American Ceramic Society 64, 556 (1981).

21 N.-H. Chan, R. K. Sharma and D. M. Smyth, Journal of the American Ceramic Society 65, 167 (1982).

22 N.-H. Chan and D. M. Smyth, Journal of the American Ceramic Society 67, 285 (1984).

23 H.-J. Hagemann and D. Hennings, Journal of the American Ceramic Society 64, 590 (1981).

24 C.-R. Song and H.-I. Yoo, Physical Review B 61, 3975 (2000).

25 H.-I. Yoo, C.-R. Song and D.-K. Lee, Journal of Electroceramics 8, 5 (2002).

26 H. M. Chan, M. R. Harmer and D. M. Smyth, Journal of the American Ceramic Society 69, 507 (1986).

27 J. Daniels, K. H. Hardtl, D. Hennings and R. Wernicke, Philips Research Reports 31, 487 (1976).

28 F. D. Morrison, A. M. Coats, D. C. Sinclair and A. R. West, Journal of Electroceramics 6, 219 (2001).

29 G. V. Lewis and C. R. A. Catlow, Radiation Effects 73, 307 (1983).

30 D. Makovec, Z. Samardžija, U. Delalut and D. Kolar, Journal of the American Ceramic Society 78, 2193 (1995).

31 C. L. Freeman, J. A. Dawson, H.-R. Chen, J. H. Harding, L.-B. Ben and D. C. Sinclair, Journal of Materials Chemistry 21, 4861 (2011).

32 C. L. Freeman, J. A. Dawson, H.-R. Chen, L. Ben, J. H. Harding, F. D. Morrison, D. C. Sinclair and A. R. West, Advanced Functional Materials 23, 3925 (2013).

33 J. Li, S. Luo and M. A. Alim, Materials Letters 60, 720 (2006).

34 C. Jorel, C. Vallée, P. Gonon, E. Gourvest, C. Dubarry and E. Defay, Applied Physics Letters 94, 253502 (2009).

35 C.-Y. Liu, B.-Y. Chen and T.-Y. Tseng, Journal of Applied Physics 95, 5602 (2004).

36 Y. Sun, W. Zhang, Y. Xing, F. Li, Y. Zhao, Z. Xia, L. Wang, X. Ma, Q.-K. Xue and J. Wang, Scientific Reports 4, 6040 (2014).

37 T. Menke, R. Dittmann, P. Meuffels, K. Szot and R. Waser, Journal of Applied Physics 106, 114507 (2009).

38 H. Kurokawa, L. Yang, C. P. Jacobson, L. C. De Jonghe and S. J. Visco, Journal of Power Sources 164, 510 (2007).

39 Q. X. Fu, F. Tietz and D. Stöver, Journal of The Electrochemical Society 153, D74 (2006).

40 X. Zhou, N. Yan, K. T. Chuang and J. Luo, RSC Advances 4, 118 (2014).

41 K. Ueno, I. H. Inoue, H. Akoh, M. Kawasaki, Y. Tokura and H. Takagi, Applied Physics Letters 83, 1755 (2003).

42 H. Ohta, Y. Masuoka, R. Asahi, T. Kato, Y. Ikuhara, K. Nomura and H. Hosono, Applied Physics Letters 95, 113505 (2009).

43 K. Park, J. S. Son, S. I. Woo, K. Shin, M.-W. Oh, S.-D. Park and T. Hyeon, Journal of Materials Chemistry A 2, 4217 (2014).

44 W. J. Weber, R. C. Ewing, C. R. A. Catlow, T. Diaz de la Rubia, L. W. Hobbs, C. Kinoshita, Hj. Matzke, A. T. Motta, M. Nastasi, E. K. H. Salje, E. R. Vance and S. J. Zinkle, Journal of Materials Research 13, 1434 (1998).

45 T. Riste, E.J. Samuelsen, K. Otnes and J. Feder, Solid State Communications 9, 1455 (1971).

46 G. Shirane and Y. Yamada, Physical Review 177, 858 (1969).

47 K. Tsuda and M. Tanaka, Acta Crystallographica Section A 51, 7 (1995).

48 R. Leapman, L. Grunes and P. Fejes, Physical Review B 26, 614 (1982).

49 A. Müller and K. H. Härdtl, Applied Physics A 49, 75 (1989).

50 R. Waser, Solid State Ionics 75, 89 (1995).

51 C. Shin, H. Yoo and C. Lee, Solid State Ionics 178, 1081 (2007).

52 I. Bykov, M. Makarova, V. Trepakov, A. Dejneka, L. Yurchenko, A. Jäger and L. Jastrabik, Physica Status Solidi (b) 250, 821 (2013).

53 A. Koehl, D. Kajewski, J. Kubacki, C. Lenser, R. Dittmann, P. Meuffels, K. Szot, R. Waser and J. Szade, Physical Chemistry Chemical Physics 15, 8311 (2013).

54 R. Hagenbeck and R. Waser, Journal of Applied Physics 83, 2083 (1998).

55 M. Savinov, V. A. Trepakov, P. P. Syrnikov, V. Železný, J. Pokorný, A. Dejneka, L. Jastrabík and P. Galinetto, Journal of Physics: Condensed Matter 20, 095221 (2008).

56 G. Xiao, S. Nuansaeng, L. Zhang, S. Suthirakun, A. Heyden, H.-C. z. Loye and F. Chen, Journal of Materials Chemistry A 1, 10546 (2013).

57 N.-H. Chan, R. K. Sharma and D. M. Smyth, Journal of The Electrochemical Society 128, 1762 (1981).

58 M. J. Akhtar, Z. U. N. Akhtar, R. A. Jackson and C. R. A. Catlow, Journal of the American Ceramic Society 78, 421 (1995).

59 T. Tanaka, K. Matsunaga, Y. Ikuhara and T. Yamamoto, Physical Review B 68 (2003).

60 B. Liu, V. R. Cooper, H. Xu, H. Xiao, Y. Zhang and W. J. Weber, Physical Chemistry Chemical Physics 16, 15590 (2014).

61 N. G. Eror and U. Balachandran, Journal of Solid State Chemistry 40, 85 (1981).

62 U. Balachandran and N. G. Eror, Journal of the American Ceramic Society 64, c-75 (1981).

63 J. E. Sunstrom IV, S. M. Kauzlarich and P. Klavins, Chemistry of Materials 4, 346 (1992).

64 M. Higuchi, K. Aizawa, K. Yamaya and K. Kodaira, Journal of Solid State Chemistry 92, 573 (1991).

65 S. A. Howard, J. K. Yau and H. U. Anderson, Journal of Applied Physics 65, 1492 (1989).

66 S. Hashimoto, L. Kindermann, F. W. Poulsen and M. Mogensen, Journal of Alloys and Compounds 397, 245 (2005).

67 U. Balachandran and N. G. Eror, Journal of The Electrochemical Society 129, 1021 (1982).

68 B. Odekirk, U. Balachandran, N. G. Eror and J. S. Blakemore, Communications of the American Ceramic Society 66, C-22 (1983).

69 B. F. Flandermeyer, A. K. Agarwal, H. U. Anderson and M. M. Nasrallah, Journal of Materials Science 19, 2593 (1984).

70 R. Moos, T. Bischoff, W. Menesklou and K. H. Härdtl, Journal of Materials Science 32, 4247 (1997).

71 A. Müller and K. H. Härdtl, Applied Physics A 65, 291 (1997).

72 J. Canales-Vázquez, M. J. Smith, J. T. S. Irvine and W. Zhou, Advanced Functional Materials 15, 1000 (2005).

73 C.-D. Savaniu and J. T. S. Irvine, Journal of Materials Chemistry 19, 8119 (2009).

74 C.-D. Savaniu, D. N. Miller, J. T. S. Irvine and M. Menon, Journal of the American Ceramic Society 96, 1718 (2013).

75 P. D. Battle, J. E. Bennett, J. Sloan, R. J. D. Tilley and J. F. Vente, Journal of Solid State Chemistry 149, 360 (2000).

76 C. J. Howard, G. R. Lumpkin, R. I. Smith and Z. Zhang, Journal of Solid State Chemistry 177, 2726 (2004).

77 T. J. Seebeck, Abhandlungen der Königlichen Akademie der Wissenschaften zu Berlin, 265 (1823).

78 J. C. Peltier, Annales de Chimie et de Physique 56, 371 (1834).

79 G. J. Snyder and E. S. Toberer, Nature Materials 7, 105 (2008).

80 D. M. Rowe ed., *CRC Handbook of Thermoelectrics* (CRC Press, Boca Raton, 1995).

81 R. Venkatasubramanian, C. Watkins, D. Stokes, J. Posthill and C. Caylor, Electron Devices Meeting, Washington, DC, 367 (2007).

82 M. S. Dresselhaus, G. Chen, Z. F. Ren, G. Dresselhaus, A. Henry and J.-P. Fleurial, JOM 61, 86 (2009).

83 C.-T. Hsu, D.-J. Yao, K.-J. Ye and B. Yu, Journal of Renewable and Sustainable Energy 2, 013105 (2010).

84 D. Dai, Y. Zhou and J. Liu, Renewable Energy 36, 3530 (2011).

85 C.-T. Hsu, G.-Y. Huang, H.-S. Chu, B. Yu and D.-J. Yao, Applied Energy 88, 1291 (2011).

86 C. Wood, Reports on Progress in Physics 51, 459 (1988).

87 D. M. Rowe, Renewable Energy 16, 1251 (1999).

88 B. C. Sales, MRS Bulletin 23, 15 (1998).

89 T. M. Tritt and M. A. Subramanian, MRS Bulletin 31, 188 (2006).

90 G. S. Nolas, J. Poon and M. Kanatzidis, MRS Bulletin 31, 199 (2006).

91 G. Sebald, D. Guyomar and A. Agbossou, Smart Materials and Structures 18, 125006 (2009).

92 D. Nemir and J. Beck, Journal of Electronic Materials 39, 1897 (2010).

93 A. J. Minnich, M. S. Dresselhaus, Z. F. Ren and G. Chen, Energy & Environmental Science 2, 466 (2009).

94 M. Jonson and G. D. Mahan, Physical Review B 21, 4223 (1980).

95 M. Cutler, J. Leavy and R. Fitzpatrick, Physical Review 133, A1143 (1964).

96 M. Cutler, R. L. Fitzpatrick and J. F. Leavy, Journal of Physics and Chemistry of Solids 24, 319 (1963).

97 M. Ohtaki, Journal of the Ceramic Society of Japan 119, 770 (2011).

98 J. P. Heremans, V. Jovovic, E. S. Toberer, A. Saramat, K. Kurosaki, A. Charoenphakdee, S. Yamanaka and G. J. Snyder, Science 321, 554 (2008).

99 O. Yamashita and N. Sadatomi, Journal of Applied Physics 88, 245 (2000).

100 J. P. Doumerc, M. Blangero, M. Pollet, D. Carlier, J. Darriet, R. Berthelot, C. Delmas and R. Decourt, Journal of Electronic Materials 38, 1078 (2009).

101 J. R. Sootsman, D. Y. Chung and M. G. Kanatzidis, Angewandte Chemie 48, 8616 (2009).

102 R. Keyes, Physical Review 115, 564 (1959).

103 H. Kleinke, Chemistry of Materials 22, 604 (2010).

104 B. C. Sales, B. C. Chakoumakos, D. Mandrus and J. W. Sharp, Journal of Solid State Chemistry 146, 528 (1999).

105 J. Dong, O. F. Sankey, G. K. Ramachandran and P. F. McMillan, Journal of Applied Physics 87, 7726 (2000).

106 B. C. Sales, B. C. Chakoumakos and D. Mandrus, Physical Review B 61, 2475 (2000).

107 C. M. Bhandari and D. M. Rowe, Journal of Physics C: Solid State Physics 11, 1787 (1978).

108 K. Koumoto, I. Terasaki and R. Funahashi, MRS Bulletin 31, 206 (2006).

109 S. Li, R. Funahashi, I. Matsubara, K. Ueno and H. Yamada, Journal of Materials Chemistry 9, 1659 (1999).

110 M. Shikano and R. Funahashi, Applied Physics Letters 82, 1851 (2003).

111 R. Funahashi, I. Matsubara and S. Sodeoka, Applied Physics Letters 76, 2385 (2000).

112 R. Funahashi and M. Shikano, Applied Physics Letters 81, 1459 (2002).

113 J. J. Shen, X. X. Liu, T. J. Zhu and X. B. Zhao, Journal of Materials Science 44, 1889 (2009).

114 J. C. Caylor, K. Coonley, J. Stuart, T. Colpitts and R. Venkatasubramanian, Applied Physics Letters 87, 023105 (2005).

115 A. I. Hochbaum, R. Chen, R. D. Delgado, W. Liang, E. C. Garnett, M. Najarian, A. Majumdar and P. Yang, Nature 451, 163 (2008).

116 T. C. Harman, P. J. Taylor, M. P. Walsh and B. E. LaForge, Science 297, 2229 (2002).

117 R. Venkatasubramanian, E. Siivola, T. Colpitts and B. O'Quinn, Nature 431, 597 (2001).

118 J. Yang and F. R. Stabler, Journal of Electronic Materials 38, 1245 (2009).

119 Q. Li, Z. Lin and J. Zhou, Journal of Electronic Materials 38, 1268 (2009).

120 E. S. Toberer, A. F. May and G. J. Snyder, Chemistry of Materials 22, 624 (2010).

121 M. G. Kanatzidis, Chemistry of Materials 22, 648 (2010).

122 K. Salzgeber, P. Prenninger, A. Grytsiv, P. Rogl and E. Bauer, Journal of Electronic Materials 39, 2074 (2010).

123 J. W. Fergus, Journal of the European Ceramic Society 32, 525 (2012).

124 L. I. Anatychuk, Yu. Yu. Rozver and D. D. Velichuk, Journal of Electronic Materials 40, 1206 (2011).

125 B. Poudel, Q. Hao, Y. Ma, Y. Lan, A. Minnich, B. Yu, X. Yan, D. Wang, A. Muto, D. Vashaee, X. Chen, J. Liu, M. S. Dresselhaus, G. Chen and Z. Ren, Science 320, 634 (2008).

126 P. F. P. Poudeu, J. D'Angelo, A. D. Downey, J. L. Short, T. P. Hogan and M. G. Kanatzidis, Angewandte Chemie 118, 3919 (2006).

127 J. Androulakis, C.-H. Lin, H.-J. Kong, C. Uher, C.-I. Wu, T. Hogan, B. A. Cook, T. Caillat, K. M. Paraskevopoulos and M. G. Kanatzidis, Journal of the American Chemical Society 129, 9780 (2007).

128 J. R. Sootsman, H. Kong, C. Uher, J. J. D'Angelo, C. I. Wu, T. P. Hogan, T. Caillat, and M. G. Kanatzidis, Angewandte Chemie 47, 8618 (2008).

129 X. W. Wang, H. Lee, Y. C. Lan, G. H. Zhu, G. Joshi, D. Z. Wang, J. Yang, A. J. Muto, M. Y. Tang, J. Klatsky, S. Song, M. S. Dresselhaus, G. Chen and Z. F. Ren, Applied Physics Letters 93, 193121 (2008).

130 G. Joshi, H. Lee, Y. Lan, X. Wang, G. Zhu, D. Wang, R. W. Gould, D. C. Cuff, M. Y. Tang, M. S. Dresselhaus, G. Chen and Z. Ren, Nano letters 8, 4670 (2008).

131 L. Hicks and M. Dresselhaus, Physical Review B 47, 12727 (1993).

132 L. Hicks and M. Dresselhaus, Physical Review B 47, 16631 (1993).

133 H. Ohta, K. Sugiura and K. Koumoto, Inorganic Chemistry 47, 8429 (2008).

134 W. Koshibae, K. Tsutsui and S. Maekawa, Physical Review B 62, 6869 (2000).

135 S.-i. Shamoto, Y. Hasegawa and T. Kajitani, Japanese Journal of Applied Physics 45, 6395 (2006).

136 B. Dutta, J. Battogtokh, D. McKewon, I. Vidensky, N. Dutta and I. L. Pegg, Journal of Electronic Materials 36, 746 (2007).

137 N. Li, Y. Jiang, G. Li, C. Wang, J. Shi and D. Yu, Journal of Alloys and Compounds 467, 444 (2009).

138 C. D. Ling, K. Aivazian, S. Schmid and P. Jensen, Journal of Solid State Chemistry 180, 1446 (2007).

139 H. Fukutomi, Y. Konno, K. Okayasu, M. Hasegawa and H. Nakatsugawa, Materials Science and Engineering: A 527, 61 (2009).

140 T. Tyson, Z. Chen, Q. Jie, Q. Li and J. Tu, Physical Review B 79 (2009).

141 M. Karppinen, H. Fjellvåg, T. Konno, Y. Morita, T. Motohashi and H. Yamauchi, Chemistry of Materials 16, 2790 (2004).

142 M. Jansen and R. Hoppe, Zeitschrift für anorganische und allgemeine Chemie 480, 104 (1974).

143 I. Terasaki, Y. Sasago and K. Uchinokura, Physical Review B 56, R12685 (1997).

144 I. Terasaki, 24st Int. Conf. Thermoelectrics, 301 (2005).

145 K. Fujita, T. Mochida and K. Nakamura, Japanese Journal of Applied Physics 40, 4644 (2001).

146 K. Park, K. U. Jang, H. C. Kwon, J. G. Kim and W. S. Cho, Journal of Alloys and Compounds 419, 213 (2006).

147 K. Park and J. H. Lee, Materials Letters 62, 2366 (2008).

148 N. V. Nong, S. Yanagiya, S. Monica, N. Pryds and M. Ohtaki, Journal of Electronic Materials 40, 716 (2011).

149 N. Van Nong, N. Pryds, S. Linderoth and M. Ohtaki, Advanced materials 23, 2484 (2011).

150 R. Funahashi, I. Matsubara, H. Ikuta, T. Takeuchi, U. Mizutani and S. Sodeoka, Japanese Journal of Applied Physics 39, L1127 (2000).

151 Y. Liu, Y. Lin, L. Jiang, C.-W. Nan and Z. Shen, Journal of Electroceramics 21, 748 (2007).

152 H. Su, Y. Jiang, X. Lan, X. Liu, H. Zhong and D. Yu, Physica Status Solidi (a) 208, 147 (2011).

153 F. P. Zhang, Q. M. Lu and J. X. Zhang, Journal of Alloys and Compounds 484, 550 (2009).

154 Y. Wang, Y. Sui, J. Cheng, X. Wang and W. Su, Journal of Alloys and Compounds 477, 817 (2009).

155 Y. Wang, Y. Sui, J. Cheng, X. Wang, J. Miao, Z. Liu, Z. Qian and W. Su, Journal of Alloys and Compounds 448, 1 (2008).

156 Q. Yao, D. L. Wang, L. D. Chen, X. Shi and M. Zhou, Journal of Applied Physics 97, 103905 (2005).

157 M. Mikami and R. Funahashi, Journal of Solid State Chemistry 178, 1670 (2005).

158 F. Delorme, C. F. Martin, P. Marudhachalam, D. Ovono Ovono and G. Guzman, Journal of Alloys and Compounds 509, 2311 (2011).

159 W. Paszkowicz, J. Piętosa, S. M. Woodley, P. A. Dłużewski, M. Kozłowski and C. Martin, Powder Diffraction 25, 46 (2012).

160 B. Zhan, J. Lan, Y. Liu, Y. Lin, Y. Shen and C. Nan, Journal of Materials Science & Technology 30, 821 (2014).

161 M. Ohtaki, H. Koga, T. Tokunaga, K. Eguchi and H. Arai, Journal of Solid State Chemistry 120, 105 (1995).

162 P. X. Thao, T. Tsuji, M. Hashida and Y. Yamamura, Journal of the Ceramic Society of Japan 111, 544 (2003).

163 G. Xua, R. Funahashi, Q. Pu, B. Liu, R. Tao, G. Wang and Z. Ding, Solid State Ionics 171, 147 (2004).

164 D. Flahaut, T. Mihara, R. Funahashi, N. Nabeshima, K. Lee, H. Ohta and K. Koumoto, Journal of Applied Physics 100, 084911 (2006).

165 Y. Wang, Y. Sui and W. Su, Journal of Applied Physics 104, 093703 (2008).

166 Y. Wang, Y. Sui, H. Fan, X. Wang, Y. Su, W. Su and X. Liu, Chemistry of Materials 21, 4653 (2009).

167 L. Pi, S. Hébert, C. Martin, A. Maignan and B. Raveau, Physical Review B 67 (2003).

168 L. Bocher, M. H. Aguirre, D. Logvinovich, A. Shkabko, R. Robert, M. Trottmann and A. Weidenkaff, Inorganic Chemistry 47, 8077 (2008).

169 J. Lan, Y.-H. Lin, H. Fang, A. Mei, C.-W. Nan, Y. Liu, S. Xu and M. Peters, Journal of the American Ceramic Society 93, 2121 (2010).

170 R. Kabir, T. Zhang, R. Donelson, D. Wang, R. Tian, T. T. Tan, B. Gong and S. Li, Physica Status Solidi (a) 211, 1200 (2014).

171 M. Ohtaki, K. Araki and K. Yamamoto, Journal of Electronic Materials 38, 1234 (2009).

172 M. Ohtaki, T. Tsubota, K. Eguchi and H. Arai, Journal of Applied Physics 79, 1816 (1996).

173 K. H. Kim, S. H. Shim, K. B. Shim, K. Niihara and J. Hojo, Journal of the American Ceramic Society 88, 628 (2005).

174 K. Park, K. Y. Ko, W. S. Seo, W. S. Cho, J. G. Kim and J. Y. Kim, Journal of the European Ceramic Society 27, 813 (2007).

175 K. Park and J. K. Seong, Journal of Alloys and Compounds 464, 1 (2008).

176 H. Yamaguchi, Y. Chonan, M. Oda, T. Komiyama, T. Aoyama and S. Sugiyama, Journal of Electronic Materials 40, 723 (2011).
177 N. Ma, J. F. Li, B. P. Zhang, Y. H. Lin, L. R. Ren and G. F. Chen, Journal of Physics and Chemistry of Solids 71, 1344 (2010).
178 Y. Kinemuchi, M. Mikami, K. Kobayashi, K. Watari and Y. Hotta, Journal of Electronic Materials 39, 2059 (2010).
179 J. P. Wiff, Y. Kinemuchi, H. Kaga, C. Ito and K. Watari, Journal of the European Ceramic Society 29, 1413 (2009).
180 S. Saini, P. Mele, H. Honda, K. Matsumoto, K. Miyazaki and A. Ichinose, Journal of Electronic Materials 43, 2145 (2014).
181 S. Saini, P. Mele, H. Honda, D. J. Henry, P. E. Hopkins, L. Molina-Luna, K. Matsumoto, K. Miyazaki and A. Ichinose, Japanese Journal of Applied Physics 53, 060306 (2014).
182 S. Ohta, T. Nomura, H. Ohta and K. Koumoto, Journal of Applied Physics 97, 034106 (2005).
183 S. Ohta, T. Nomura, H. Ohta, M. Hirano, H. Hosono and K. Koumoto, Applied Physics Letters 87, 092108 (2005).
184 T. Okuda, K. Nakanishi, S. Miyasaka and Y. Tokura, Physical Review B 63 (2001).
185 H. Muta, K. Kurosaki and S. Yamanaka, Journal of Alloys and Compounds 392, 306 (2005).
186 K. Kato, M. Yamamoto, S. Ohta, H. Muta, K. Kurosaki, S. Yamanaka, H. Iwasaki, H. Ohta and K. Koumoto, Journal of Applied Physics 102, 116107 (2007).
187 C. Yu, M. L. Scullin, M. Huijben, R. Ramesh and A. Majumdar, Applied Physics Letters 92, 191911 (2008).
188 C. Yu, M. L. Scullin, M. Huijben, R. Ramesh and A. Majumdar, Applied Physics Letters 92, 092118 (2008).
189 J. Ravichandran, W. Siemons, D.-W. Oh, J. T. Kardel, A. Chari, H. Heijmerikx, M. L. Scullin, A. Majumdar, R. Ramesh and D. G. Cahill, Physical Review B 82 165126-1 (2010).
190 H. Muta, K. Kurosaki and S. Yamanaka, Journal of Alloys and Compounds 350, 292 (2003).
191 S. Ohta, H. Ohta and K. Koumoto, Journal of the Ceramic Society of Japan 114, 102 (2006).
192 J. Liu, C. L. Wang, W. B. Su, H. C. Wang, J. C. Li, J. L. Zhang and L. M. Mei, Journal of Alloys and Compounds 492, L54 (2010).
193 Y. Cui, J. R. Salvador, J. Yang, H. Wang, G. Amow and H. Kleinke, Journal of Electronic Materials 38, 1002 (2009).
194 J. Liu, C. L. Wang, W. B. Su, H. C. Wang, P. Zheng, J. C. Li, J. L. Zhang and L. M. Mei, Applied Physics Letters 95, 162110 (2009).
195 J. Liu, H. C. Wang, W. B. Su, C. L. Wang, J. L. Zhang and L. M. Mei, Solid State Sciences 12, 134 (2010).
196 N. Okinaka, L. Zhang and T. Akiyama, ISIJ International 50, 1300 (2010).

197 N. Wang, L. Han, H. He, Y. Ba and K. Koumoto, Journal of Alloys and Compounds 497, 308 (2010).

198 N. Wang, H. He, X. Li, L. Han and C. Zhang, Journal of Alloys and Compounds 506, 293 (2010).

199 N. Wang, H. Li, Y. Ba, Y. Wang, C. Wan, K. Fujinami and K. Koumoto, Journal of Electronic Materials 39, 1777 (2010).

200 H. C. Wang, C. L. Wang, W. B. Su, J. Liu, Y. Sun, H. Peng and L. M. Mei, Journal of the American Ceramic Society 94, 838 (2011).

201 H. Ohta, S. Kim, Y. Mune, T. Mizoguchi, K. Nomura, S. Ohta, T. Nomura, Y. Nakanishi, Y. Ikuhara, M. Hirano, H. Hosono and K. Koumoto, Nature Materials 6, 129 (2007).

202 G. Chen, T. Zeng, T. Borca-Tasciuc and D. Song, Materials Science and Engineering: A 292, 155 (2000).

203 K. H. Lee, S. W. Kim, H. Ohta and K. Koumoto, Journal of Applied Physics 100, 063717 (2006).

204 K. H. Lee, Y. F. Wang, S. W. Kim, H. Ohta and K. Koumoto, International Journal of Applied Ceramic Technology 4, 326 (2007).

205 Y. F. Wang, K. H. Lee, H. Ohta and K. Koumoto, Ceramics International 34, 849 (2008).

206 Y. Wang, K. H. Lee, H. Hyuga, H. Kita, H. Ohta and K. Koumoto, Journal of Electroceramics 24, 76 (2008).

207 Y. Wang, K. H. Lee, H. Ohta and K. Koumoto, Journal of Applied Physics 105, 103701 (2009).

Chapter 3: Experimental Procedure

3.1 Ceramic Processing Procedure

3.1.1 Powder Preparation and Calcination

Ceramics were prepared from $SrCO_3$ (99.90%, Sigma Aldrich), $CaCO_3$ (99%, Sigma Aldrich), La_2O_3 (99.99%, Sigma Aldrich) and TiO_2 (99.90%, Sigma Aldrich) by a solid state reaction method. Strontium carbonate and calcium carbonate were dried in a chamber furnace at 180 ℃ for 24 hours. Titanium (IV) dioxide and Lanthanum (III) oxide were dried at 900 ℃ for 3 hours, then cooled down to 300 ℃. All the hot dry raw materials were stored in a vacuum desiccator to cool down and to avoid weight gain by moisture. Stoichiometric amounts of dry raw materials were weighed with a precision of ± 0.0001 g based on compositions in Table 3.1. Starting powders were mixed using an attrition mill for 60 minutes with yttria-stabilised zirconia (YSZ) media in iso-propanol. After being dried at ~80 °C and sieved through a 300 μm mesh, mixed powders were calcined at ~1373 to 1623 K for 3 or 12 hours in an alumina crucible to decompose the carbonate and to homogenise the reactants. The heating and cooling rates were both 5 ℃/min. Finally, the powder was re-milled for 45 minutes, dried and sieved again to obtain a smaller particle size for sintering.

3.1.2 Pellets and Sintering

About ~0.4 to 2.5 g of powder were uniaxially pressed for about 1 min into pellets of 8 mm diameter with ~2.5 mm thickness and 30 mm diameter with ~1.5 mm thickness, respectively. ~2 g of powder were also uniaxially pressed into bar samples of 40 mm in length, 5 mm in width and ~3 mm thickness. Pellets and bar samples were then vacuumed in a glove and were isostatically pressed using a Cold Isostatic Press (Autoclave Engineers, Snap-tite, Inc.) at ~200 MPa.

Samples were then placed in an alumina boat with equal distance between each one, and sintered at 1773 K for 6 hours at a heating rate of 5 ℃/min in air, nitrogen or N_2/5%H_2. Various cooling rates were used, eg. 2, 5, 10, 20 and 30 ℃/min. Platinum foil was placed between the boat crucible and pellets to avoid reaction when sintering in air and nitrogen, but not in N_2/5%H_2 (powder having the same compositions as the samples was used instead of Pt foil), since Pt melts in this atmosphere at such high temperature.

3.1.3 Density Measurements

The density measurement was conducted based on the Archimedes principle. A bulk ceramic was weighed in air on a Mettler-Toledo AG balance (Laboratory & Weighing Technologies, CH-8606 Greifensee, Switzerland) to an accuracy of 0.0001g (m_1), and then was immersed into a beaker containing distilled water and the balance value was recorded (m_2). The water temperature was recorded to check the density. The density of the samples was calculated using the equation below:

$$\rho_{\text{bulk}} = \rho_{\text{H2O}} \times m_1/(m_1 - m_2) \qquad 3\text{-}1$$

where:

m_1: weight of sample in air (g),

m_2: balance reading of sample immersed in the distilled water (g),

ρ_{H2O}: density of distilled water at the experimental temperature (kg m^{-3}),

ρ_{bulk}: bulk density of the sample (kg m^{-3}).

The theoretical density was calculated based on the following equation:

$$\rho_{theory} = \frac{N \times \sum_{i=1}^{n} A_i}{V_C N_A} \qquad 3\text{-}2$$

where:

N: number of atoms per unit cell,

A: atomic weight of the element i (kg mol^{-1}),

V_c: Volume of unit cell (m^3), it is obtained from XRD data of the crushed pellets.

N_A: Avogadro’s number (atoms mol^{-1}).

Table 3-1 Fabricated compositions in the La-doped Sr and Ca based systems.

Compositions	La content
$(Sr_{1-x}La_x)_3Ti_2O_7$	0.00, 0.01, 0.02, 0.05, 0.10
$(Sr_{1-3y/2}La_y)_3Ti_2O_7$	0.01, 0.02, 0.05, 0.10
$(Sr_{1-z}La_z)_3Ti_{2-3z/4}O_7$	0.01, 0.02, 0.05, 0.10
$(Ca_{1-x}La_x)_3Ti_2O_7$	0.00, 0.01, 0.02, 0.05
$Sr_{1-x}La_xTiO_3$	0.00, 0.10, 0.20, 0.30, 0.40, 0.50, 0.60, 0.70, 0.80
$Sr_{1-3y/2}La_yTiO_3$	0.05, 0.10, 0.125, 0.15, 0.175, 0.20, 0.30, 0.40, 0.50, 0.60, 0.63, 0.67
$Sr_{1-z}La_zTi_{1-z/4}O_3$	0.10, 0.20, 0.30, 0.40, 0.50, 0.60, 0.70, 0.80

3.2 Structure Analysis

3.2.1 Particle Size Analysis (PSA)

Particle size distribution was performed on a Coulter LS130 laser analyser (Beckman Coulter Ltd., High Wycombe, Bucks, UK) to check the particle diameters of the raw materials, mixed powder and calcined powder after attrition milling. A small amount of powder was deflocculated by 5% volume aqueous acrylic polymer solution of Dispex N40 on a glass and then poured into a beaker by adding distilled water. The beaker was placed in an ultrasonic device to de-agglomerate the powder. Three runs were repeated and the run length was 300 seconds.

3.2.2 Thermogravimetric Analysis (TGA)

A Netzsch STA 449 F3 Jupiter - Simultaneous TGA-DSC was used to measure the weight variation of samples as a function of temperature in air with a high resolution of 1 μg over the entire weighing range. A Rhodium furnace with forced air cooling system was chosen to obtain accurate high temperature TG data. In order to be consistent with the experimental conditions, powders were put on top of an aluminium plate with a piece of platinum pad and then measured in air with 5 °C/min heating rate up to 1000 °C and also a 5 °C/min cooling rate.

3.2.3 X-Ray Diffraction (XRD)

A high resolution STOE STADI-P diffractometer (STOE & Cie GmbH, Darmstadt, Germany) with a linear position sensitive detector (PSD) was used for raw materials, calcined powders and crushed pellets with CuKα ($\lambda = 1.5406$ Å) radiation. The operating voltage and current were 40 kV and 30 mA, respectively. Either raw materials or calcined powder and crushed pellets were placed on acetate discs, mixed with a small blob of glue to form slurry and then dried carefully using a hot air blower. Subsequently, the mounted sample was put into the specimen holder and covered with a plate. The scan was conducted from 15 to 80 degrees, with a step size of 0.01 °.

A Siemens D500 diffractometer was also utilised for data collection of samples with CuKα ($\lambda = 1.5406$ Å) radiation. Samples were pressed lightly onto the top of a mound of putty in the plastic holder to keep the same level with the top of the holder. Diffractograms were collected across the 2θ-range of 15 to 80 degrees with a step size of 0.02 ° or 0.05 ° at a rate of 1 °/min.

The subsequent data were both handled and analysed using the computer program “STOE WinXPow”.[1]

3.2.4 Scanning Electron Microscopy (SEM)

Cut samples were mounted on aluminium stubs with conductive silver paste (Agar Scientific Ltd., Stansted, UK), while raw powders were mounted using double-side carbon tapes. A ~50 nm conductive carbon layer was then sputtered onto the surface for better Energy Dispersive Spectroscopy (EDS) signals.

Ceramic microstructure was studied using a scanning electron microscopy (JEOL JSM-6400, Tokyo, Japan) with a Link analytical energy dispersive spectroscopy (EDS) X-ray detector (Link Analytical Ltd., UK) and an FEI Inspect F Scanning Electron Microscope (SEM). Samples were carbon sputtered for Energy Dispersive Spectroscopy (EDS). Secondary electron and backscattered images were obtained from the fractured sections and surfaces of pellets. The accelerating voltage was either 15 or 20 kV.

3.2.5 Transmission Electron Microscopy (TEM)

A slice of pellet or bar sample was mounted on a Gatan Disc Grinder using a thermo-setting resin. Double sides were initially thinned to about 15~30 μm using a series of grinding papers (800, 1200 and 4000 grit SiC papers) and then was mounted on a ~3 mm diameter copper ring with a 1 mm diameter hole in the middle. A Gatan dual ion mill machine (Model 600, Pleasanton, California, USA) was used for milling with the ion beam at an angle of 12 ~ 15 degrees to the surface in order to obtain a very small hole with thin edges in the centre. The operated gun voltage and combined gun current were 4 kV and 0.5 mA, respectively. Finally, a Fischione low angle ion milling & system (Model 1010, E.A. Fischione Instruments, Inc., USA) was also employed for final milling with accelerating voltage of 3 kV and a current of 3 mA at an angle of 6 degrees.

A Philips EM 420 microscope was used to observe the diffraction patterns and microstructure of TEM samples. JEOL JEM 3010 UHR TEM with a point resolution of 0.17 nm at 300 kV was also employed for digital image acquisition using its high resolution slow-scan CCD camera.

3.3 Electrical Characterization

3.3.1 Impedance Spectroscopy (IS)

Impedance spectroscopy (IS) is a technique for the measurement of electrical properties of material-electrode systems. The main advantage of IS is its ability to separate the electro-active regions of a sample into different components: bulk, grain boundary, surface layer and electrode-related effects. Therefore, the homogeneity of electrical properties can be characterised by IS.

The general method of IS involves the application of an alternating voltage across the material over a wide frequency range. An equivalent circuit can be identified to establish the link between different elements in the circuit and the electrically distinct regions. Parallel resistance (R) and capacitance (C) elements are commonly used to characterise different regions of ceramic samples[2]. Capacitance values and their possible corresponding elements are listed in Table 3-2.

Table 3-2 Capacitance values and their possible interpretation[3].

Capacitance (F)	Phenomenon Responsible
10^{-12}	Bulk
10^{-11}	Secondary phases
10^{-11}-10^{-8}	Grain boundary
10^{-10}-10^{-9}	Bulk ferroelectric
10^{-9}-10^{-7}	Surface layers
10^{-7}-10^{-5}	Sample-electrode interface
10^{-4}	Electrochemical reactions

IS measurements were performed on an Agilent E4980A with a frequency range of 20 Hz - 2 MHz and an HP 4192A impedance analyser over the frequency range of 5 Hz - 13 MHz. It also has a variable internal direct voltage bias that can be used to check the electrode effect of the sample. Low temperature IS measurements were carried out in the range of 10 to 320 K. High temperature IS measurements were carried out in a tube furnace at temperatures ranging from ~25 to 800 ℃ in different atmospheres. The data were analysed using the software program “ZView2”.[4]

3.3.2 Seebeck Coefficient and Conductivity Measurements

Under steady-state conditions, a differential method was exploited to calculate the Seebeck coefficient from the linear fit of multiple electric potential/temperature difference data points rather than one because of its ability to eliminate the offset voltages generated by thermocouple inhomogeneity and nonequilibrium contact interfaces[5].

A Probostat (Norwegian Electro Ceramic AS) was used to measure both Seebeck coefficients and electrical conductivities at the same temperatures. A rectangular-shape bar sample of ~20 mm in length and 3 mm in width and thickness was mounted with silver electrodes on each end and connected to two voltage probes at 1/3 and 2/3 of the length. The temperatures at both end faces were measured with thermocouples. The thermocouple tips should touch the end faces of the bar sample. The hot side of the bar sample was connected to the positive terminal of the voltmeter.

The standard linear four probe method was employed for the electrical conductivity measurements. Before four probe measurements, every sample was polished to ensure electrical homogeneity along the width direction checked by impedance spectroscopy (IS). A constant current was generated and passed through the sample along the length direction using the connected Pt-wire ‘‘hand’’ electrodes, which are the same electrodes used for the voltage measurement of the Seebeck coefficient. Two more probes at 1/3 and 2/3 of the length of the sample were used to measure the total voltage V, which contains the voltage at current I and the voltage of the thermal contribution. The reversed current operation was necessary to cancel the Seebeck voltage contributions. The sample resistance R is given by:

$$R = \frac{\left(V(I^{+})+S\Delta T\right)-\left(V(I^{-})+S\Delta T\right)}{I^{+}-I^{-}} = \frac{2V(I^{+})}{2I^{+}} \qquad 3\text{-}3$$

The calculated R is used to calculate the conductivity,

$$\sigma = \frac{L}{RA} \qquad 3\text{-}4$$

where A is the area of cross sectional area of the sample and L is the distance between the middle two voltage probes[6].

3.3.3 Thermal Conductivity Measurements

A square sample of 10 mm × 10 mm with about 1 ~ 1.5 mm in thickness was prepared for thermal conductivity measurements. The sample was cleaned with isopropanol first. Then graphite spray was applied on top of both sides of the sample in a sweeping motion.

Thermal conductivity measurements were performed using a thermal properties analyser (Anter FlashlineTM 3000, Pittsburgh, PA 15235, USA) with High Speed Xenon Discharge (HSXD) pulse source. The specific heat capacity was measured by alternating between reference and sample. The thermal conductivity was calculated using the following equation:

$$\lambda = \alpha \, \rho \, C_{\mathrm{p}} \qquad 3\text{-}5$$

where α is the thermal diffusivity, C_{p} is the related values of specific heat capacity and ρ is the density.

Reference

1 N. Hirose and A. R. West, Journal of the American Ceramic Society 79 (6), 1633 (1996).

2 STOE WinXPow Version 2.10. 2004, Computer Program, STOE & Cie GmbH Hilpertstr, Darmstadt.

3 D. C. Sinclair, A. R. West and J. T. S. Irvine, Advanced Materials 2 (3), 132 (1990).

4 ZView2. 1990-2010, Computer Program, Derek Johnson, Scribner Associates, Inc.

5 J. Martin, T. Tritt and C. Uher, Journal of Applied Physics 108 (12), 121101 (2010).

6 V. Ponnambalam, S. Lindsey, N. S. Hickman and Terry M. Tritt, Review of Scientific Instruments 77 (7), 073904 (2006).

Chapter 4: Raw Powder Processing

4.1 Raw Powder Characterisation

4.1.1 Powder Preparation and Calcination

Sigma-Aldrich Company Ltd supplied $SrCO_3$ with purity 99.9%. $SrCO_3$ appears as a hygroscopic white powder. From Figure 4.1, the peaks in the XRD pattern were indexed on an ICDD card [5-418] for Strontium Carbonate. The $SrCO_3$ powder consisted of rod-like particles, as shown in Figure 4.2, and no secondary phase was observed in SEM images. Figure 4.3 shows the particle diameter distribution with a mean size of 2.2 µm and d_{90} (particle diameter with 90% of the volume < d_{90}) ~5.4 µm.

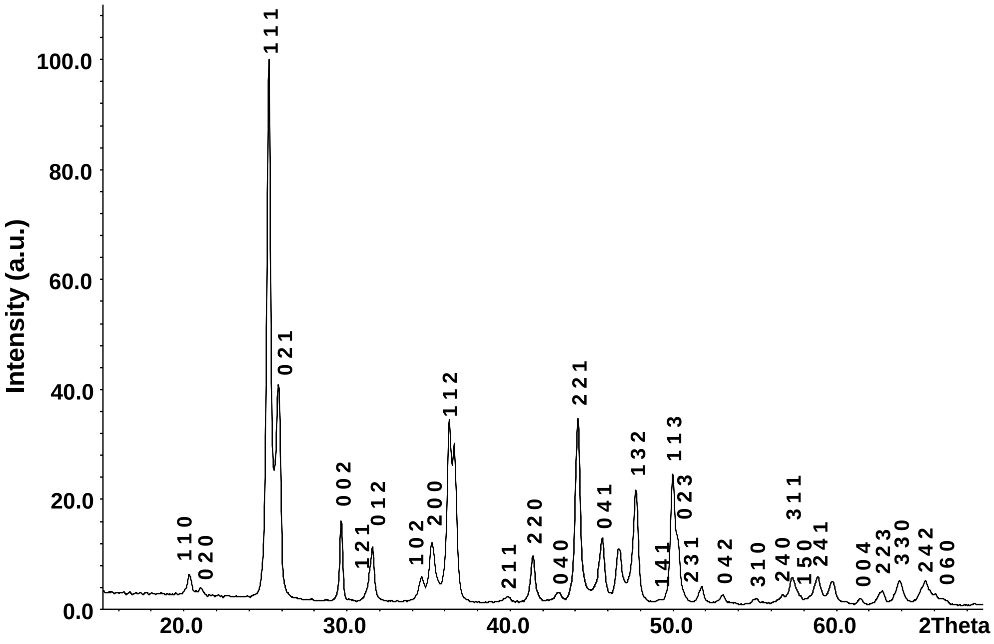

Figure 4.1 XRD trace of $SrCO_3$.

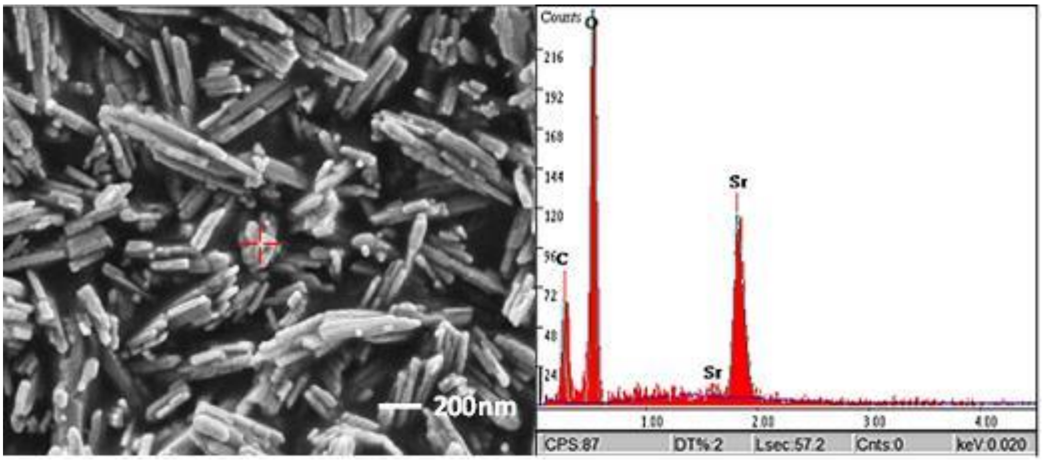

Figure 4.2 SEM image and EDS trace of $SrCO_3$.

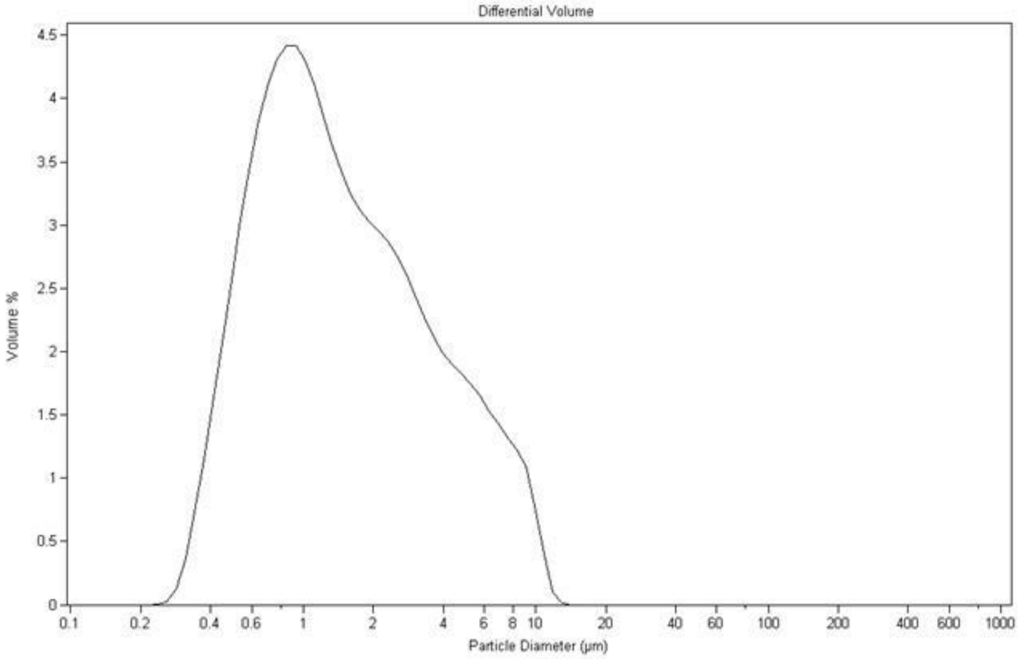

Figure 4.3 Particle size distribution of $SrCO_3$ powder.

4.1.2 Calcium Carbonate, $CaCO_3$

Calcium carbonate with 99.9% purity was obtained from Sigma-Aldrich

Company Ltd. XRD peaks indexed according to $CaCO_3$-Calcite ([5-586] ICDD card), Figure 4.4. As shown in Figure 4.5, calcium carbonate was agglomerated with blocky-like shapes but no secondary phase was observed. The mean particle size of calcium carbonate was large (~38.64 μm) with d_{90} of ~62.04 μm, Figure 4.6. Therefore, an attrition mill was required to reduce the particle size of calcium carbonate.

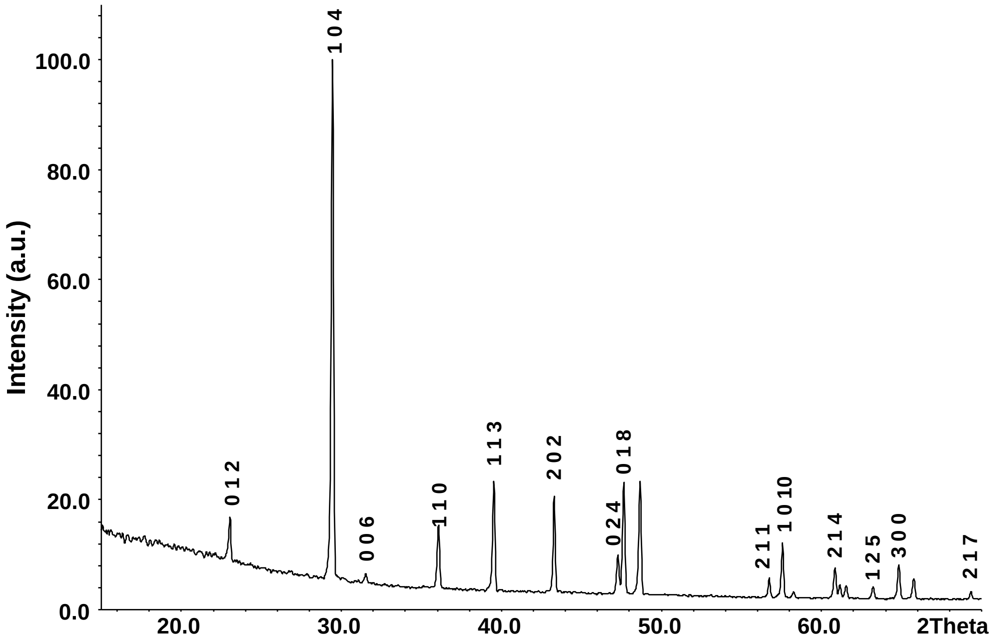

Figure 4.4 XRD trace of $CaCO_3$.

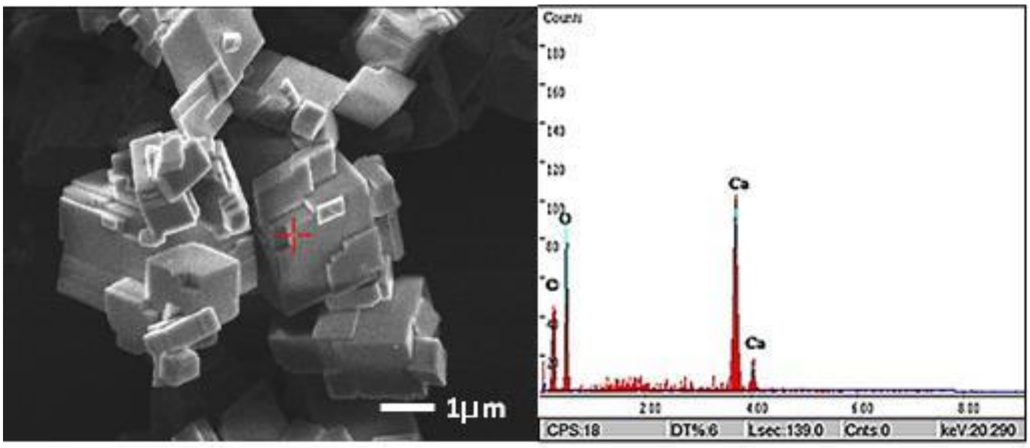

Figure 4.5 SEM image and EDS trace of $CaCO_3$.

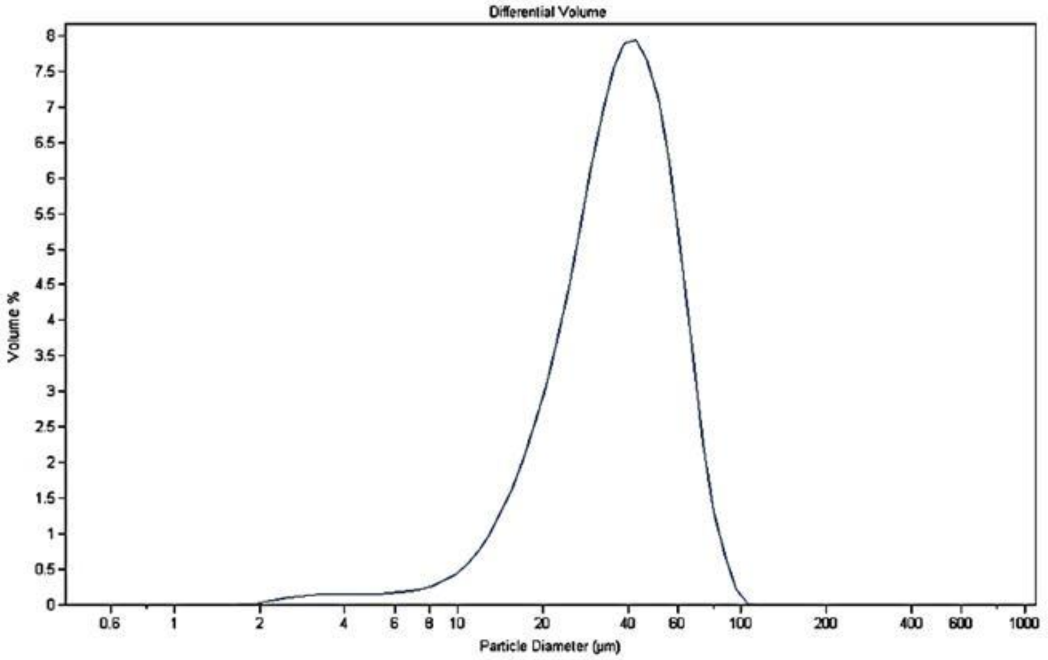

Figure 4.6 Particle size distribution of $CaCO_3$ powder.

4.1.3 Titanium (IV) Oxide, TiO_2

Titanium (IV) oxide with 99.9% purity was obtained from Sigma-Aldrich Company Ltd. As shown in Figure 4.7, XRD peaks are indexed according to TiO_2-anatase, ICDD card [21-1272]. No secondary phase was detected in SEM images from Figure 4.8. The mean particle size is small, ~0.56 μm with d_{90} of ~1.3 μm, Figure 4.9.

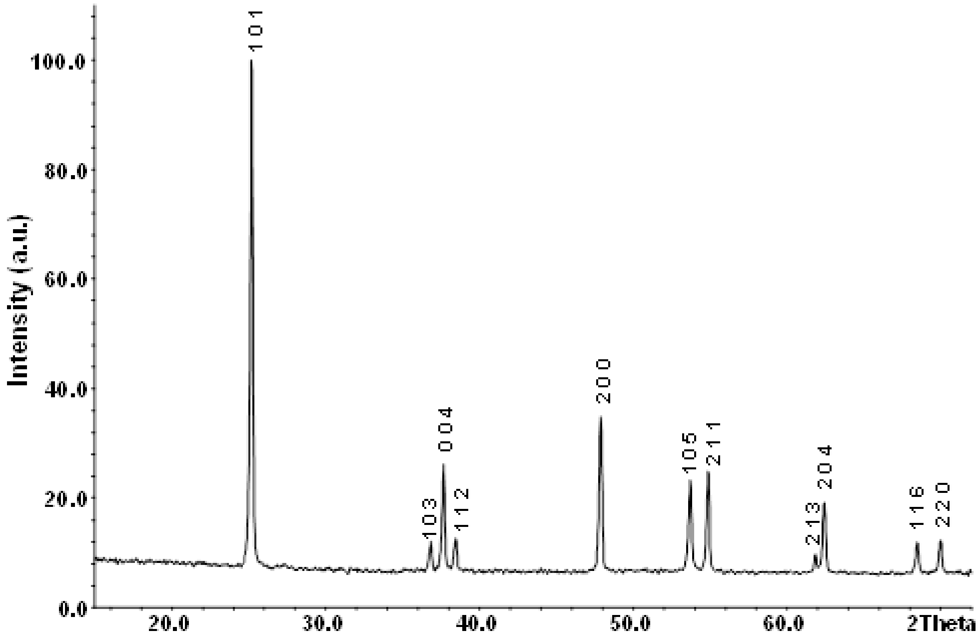

Figure 4.7 XRD trace of TiO_2.

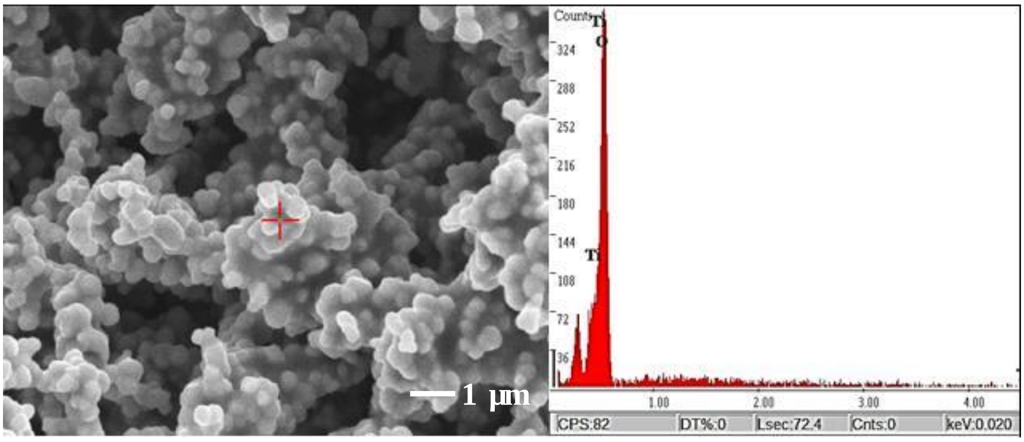

Figure 4.8 SEM image and EDS trace of TiO_2.

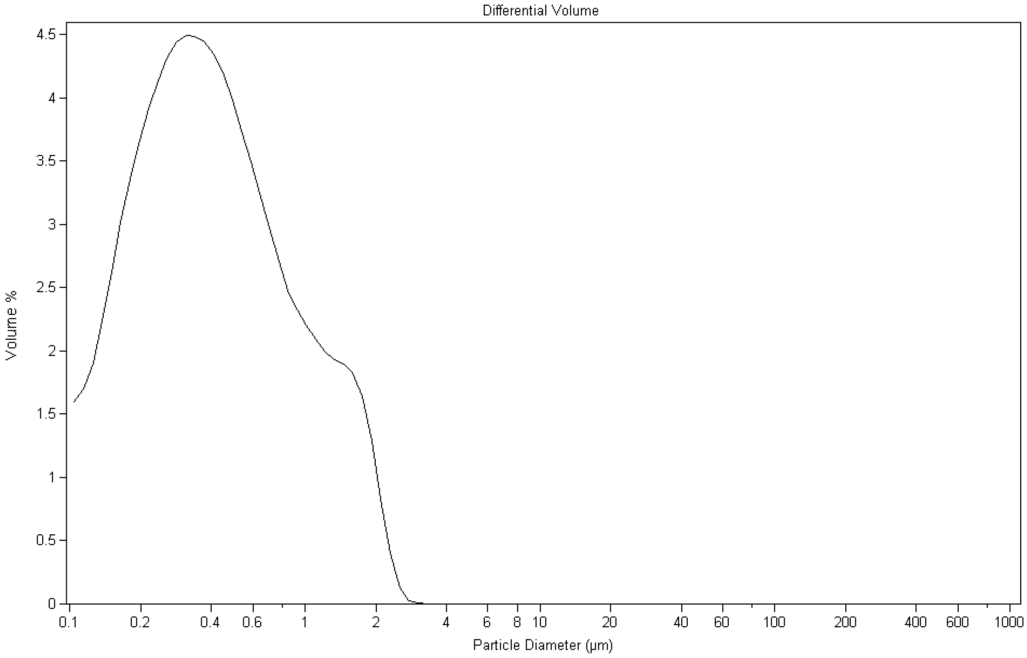

Figure 4.9 Particle size distribution of TiO_2 powder.

4.1.4 Lanthanum Oxide, La_2O_3

Lanthanum oxide with 99.99% purity was supplied by Sigma-Aldrich Company Ltd. The peaks of dried lanthanum oxide in the XRD trace corresponded well to hexagonal La_2O_3 ([5-602] ICDD card), Figure 4.10. No secondary phase was detected in SEM images, Figure 4.11. Particle size analysis shows the mean particle size is ~1 µm with d_{90} of ~2.4 µm, Figure 4.12.

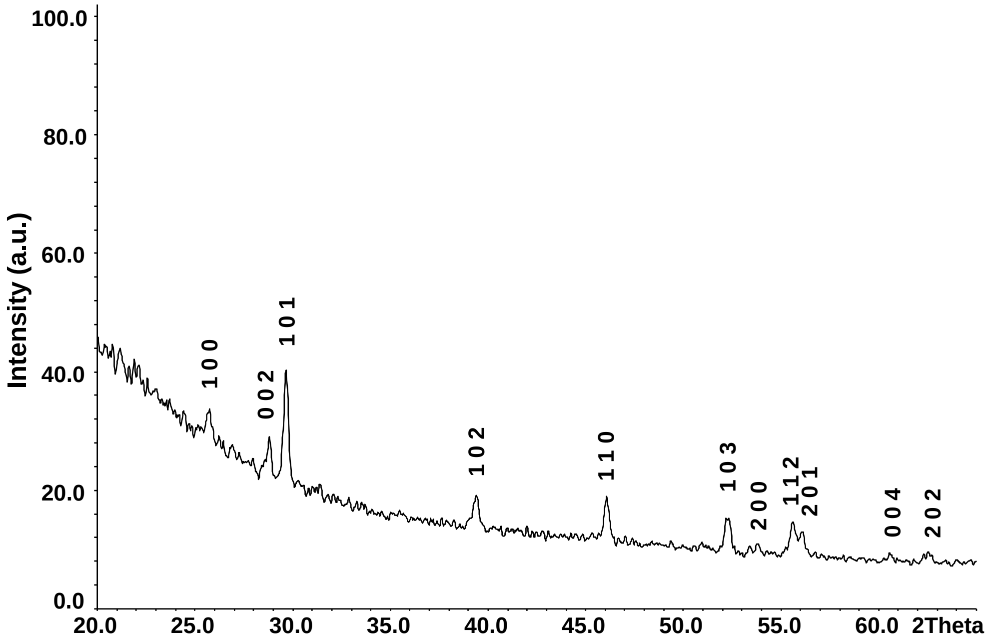

Figure 4.10 XRD trace of La_2O_3.

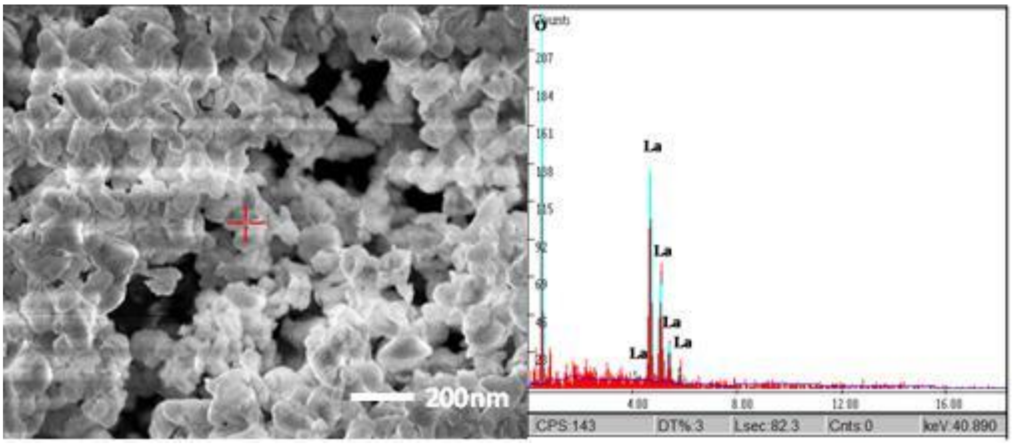

Figure 4.11 SEM image and EDS trace of La_2O_3.

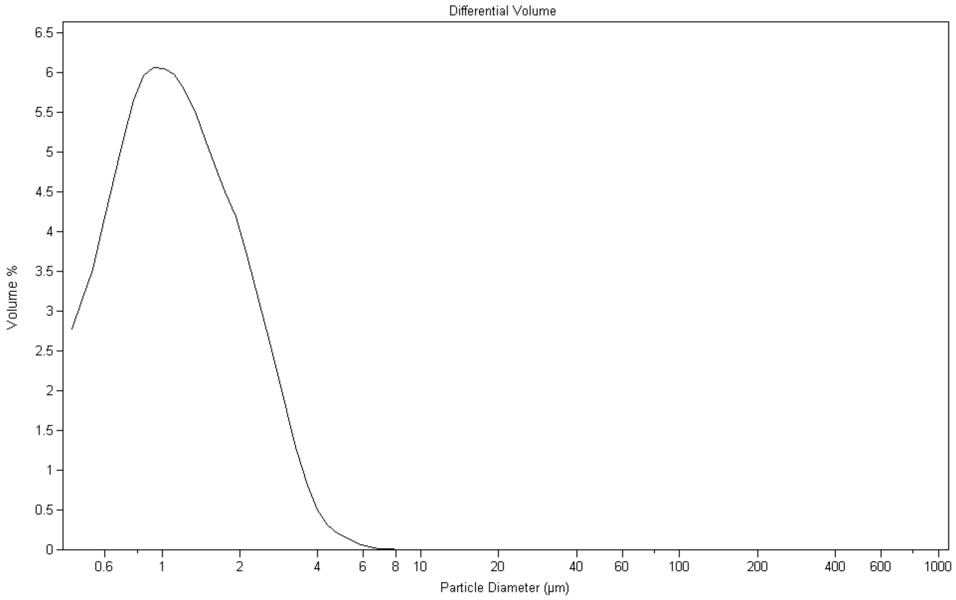

Figure 4.12 Particle size distribution of La_2O_3 powder.

4.2 Powder Processing

The particle size distribution of milled La-doped $Sr_3Ti_2O_7$ powders after calcination based on different compensation mechanisms are shown in Figure 4.13.

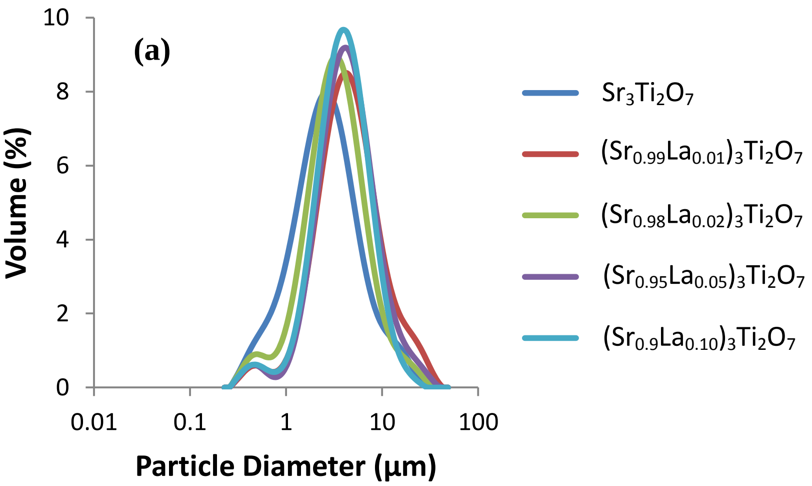

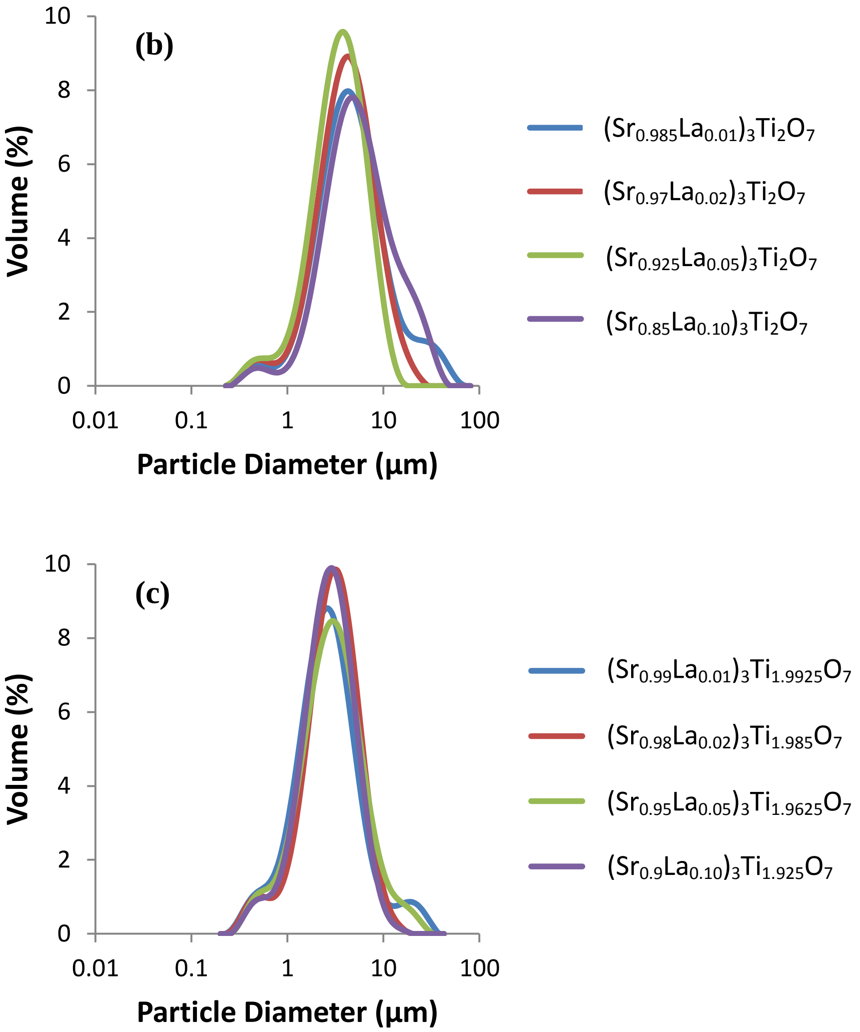

Figure 4.13 Particle size distribution of (a) $(Sr_{1-x}La_x)_3Ti_2O_7$ (x = 0.00, 0.01, 0.02, 0.05, 0.10), (b) $(Sr_{1-3y/2}La_y)_3Ti_2O_7$ (x = 0.01, 0.02, 0.05, 0.10), (c) $(Sr_{1-z}La_z)_3Ti_{2-3z/4}O_7$ (x = 0.01, 0.02, 0.05, 0.10) calcined powder after 45 minutes of attrition milling.

All as-milled powders had similar small particle distributions with mean sizes of ~5 µm and d_{90} below 15 µm, as shown in Table 4.1. Because $Sr_3Ti_2O_7$ is harder to prepare than $SrTiO_3$, higher sintering temperatures and longer holding times were used for calcination. The mean particle size of La-doped $Sr_3Ti_2O_7$ powders was larger than that La-doped $SrTiO_3$ powders.

Table 4.1 Particle sizes of calcined compositions in the La-doped $Sr_3Ti_2O_7$ series after 45 minutes of attrition milling.

Composition	x, y, z	d_{10}	d_{50}	d_{90}
$(Sr_{1-x}La_x)_3Ti_2O_7$	0.00	0.88	2.58	7.44
	0.01	1.69	4.33	12.20
	0.02	1.25	3.25	8.08
	0.05	1.75	4.18	10.30
	0.10	1.65	3.88	8.56
$(Sr_{1-3y/2}La_y)_3Ti_2O_7$	0.01	1.65	4.45	14.3
	0.02	1.56	4.10	9.62
	0.05	1.37	3.50	7.42
	0.10	1.96	5.24	14.90
$(Sr_{1-z}La_z)_3Ti_{2-3z/4}O_7$	0.01	0.96	2.57	6.75
	0.02	1.16	2.95	6.30
	0.05	1.04	2.89	7.46
	0.10	1.11	2.70	5.73

Figure 4.14 shows the particle size distribution of milled La-doped $Ca_3Ti_2O_7$ powders after calcination. All as-milled powders had small particle distributions with mean sizes of ~3 μm and d_{90} below 10 μm, as shown in Table 4.2. The attrition milling reduced the particle size of La-doped $Ca_3Ti_2O_7$ powders for sintering.

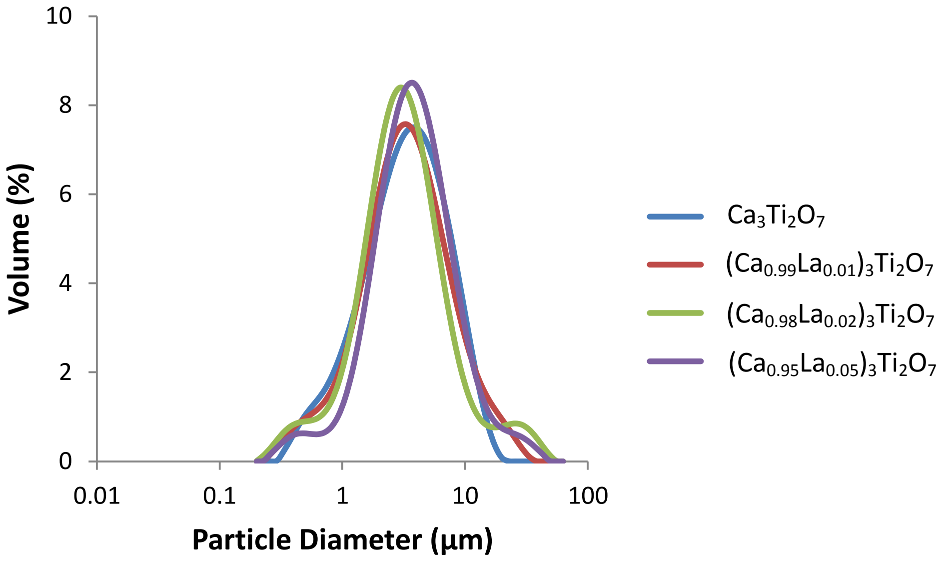

Figure 4.14 Particle size distribution of $(Ca_{1-x}La_x)_3Ti_2O_7$ (x = 0.00, 0.01, 0.02, 0.05) calcined powder after attrition milling.

Table 4.2 Particle sizes of calcined compositions in the La-doped $Ca_3Ti_2O_7$ series after 45 minutes of attrition milling.

Composition	x	d_{10}	d_{50}	d_{90}
$(Ca_{1-x}La_x)_3Ti_2O_7$	0.00	1.04	3.36	8.58
	0.01	1.06	3.28	9.67
	0.02	1.09	3.05	8.82
	0.05	1.41	3.71	9.74

The particle size distribution of milled La-doped $SrTiO_3$ powders after calcination according to different compensation mechanisms are shown in Figure 4.15. The as-milled powders were ideal for sintering with almost all particles (d_{90}) typically below 7 µm with no large agglomerates, as shown in Table 4.3.

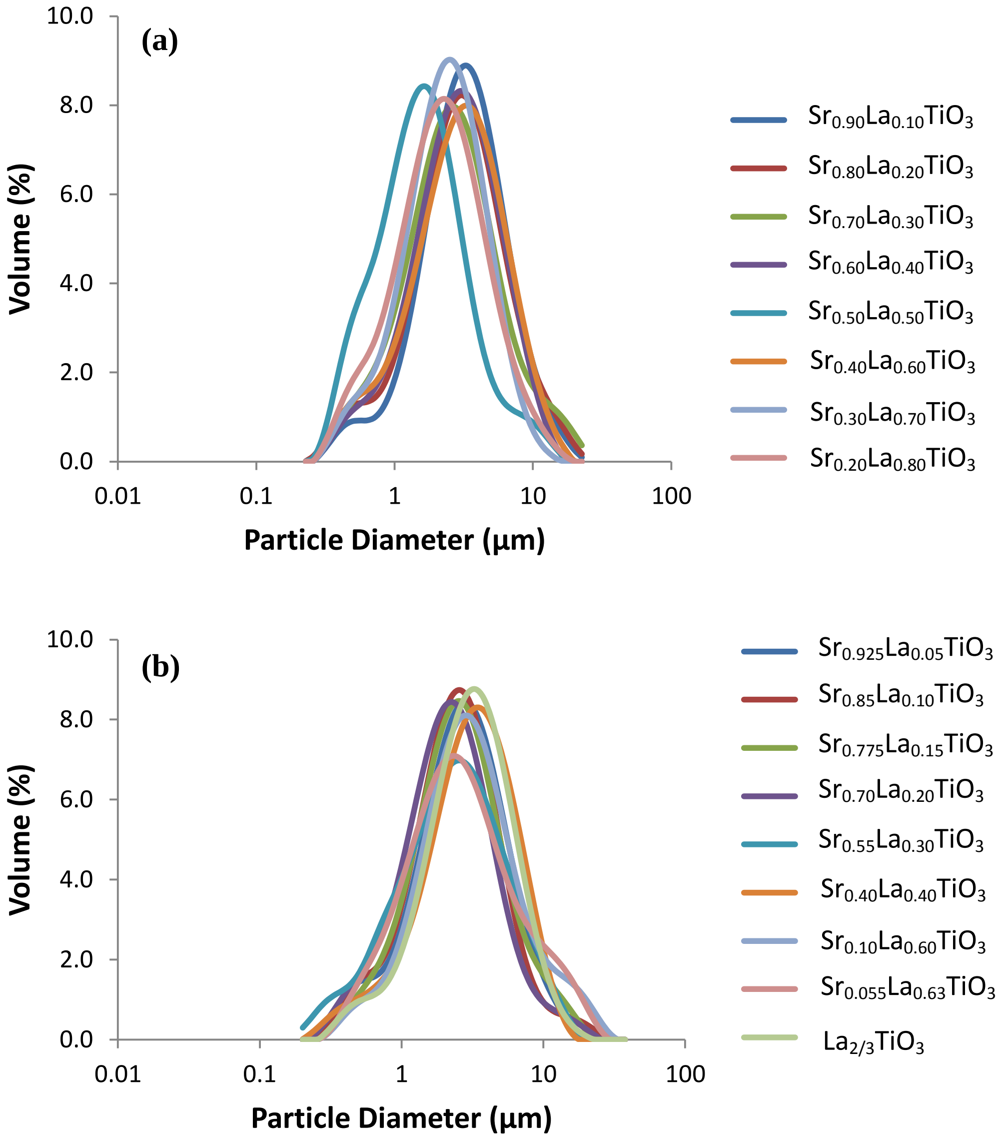

Figure 4.15 Particle size distribution of (a) $Sr_{1-x}La_xTiO_3$ (x = 0.10, 0.20, 0.30, 0.40, 0.50, 0.60, 0.70, 0.80), (b) $Sr_{1-3y/2}La_yTiO_3$ (x = 0.05, 0.10, 0.15, 0.20, 0.30, 0.40, 0.60, 0.63, 0.67) calcined powder after 45 minutes of attrition milling.

Table 4.3 Particle sizes of calcined compositions in the La-doped $SrTiO_3$ series after 45 minutes of attrition milling.

Composition	x, y	d_{10}	d_{50}	d_{90}
$Sr_{1-x}La_xTiO_3$	0.10	1.200	3.17	7.66
	0.20	0.977	2.95	7.75
	0.30	0.875	2.58	7.44
	0.40	0.982	2.84	6.88
	0.50	0.578	1.56	4.17
	0.60	0.922	2.97	7.39
	0.70	0.875	2.34	5.32
	0.80	0.755	2.18	5.67
$Sr_{1-3y/2}La_yTiO_3$	0.05	0.885	2.66	6.59
	0.10	0.851	2.42	5.90
	0.15	0.925	2.51	6.74
	0.20	0.764	2.15	5.52
	0.30	0.662	2.32	6.88
	0.40	0.984	3.10	7.33
	0.60	1.070	2.93	8.99
	0.63	0.834	2.51	9.15
	0.67	1.110	3.05	7.14

Attrition milling for 45 minutes after calcination resulted in a smaller and more homogeneous particle size distribution of the calcined particles. Single phase samples could be obtained by reducing particle size to shorten diffusion distances so that homogeneity and reaction rates are accelerated, which generally results in lower sintering temperatures and higher ceramic densities.

Chapter 5: La-doped $Sr_3Ti_2O_7$ System

5.1 Introduction

In the field of thermoelectric applications, cubic perovskite-type compounds, such as Nb-doped $SrTiO_3$, have been found to show large ZT values among the n-type oxides. However, the highest reported ZT value (0.37)[1] is still too low compared with state-of-the-art tellurium-, antimony- and germanium-based alloys (ZT ≈ 1)[2-6] because of the high thermal conductivity. Therefore, the Ruddlesden-Popper (RP) phase, $SrO(SrTiO_3)_n$ (n = integer) has attracted much attention due to its layered structure which in principle can disrupt the octahedral phonon modes to reduce thermal conductivity whilst the perovskite layers may exhibit high values of electrical conductivity and/or exhibit a large Seebeck coefficient.

The work described in section 5.2 focuses on the structure and electrical properties of undoped $Sr_3Ti_2O_7$ ceramic sintered in different atmospheres at 1500 ^oC, especially the structural stability of the Ruddlesden-Popper $Sr_3Ti_2O_7$ phase in the context of the predicted higher electrical conductivity (*n*-type) in reducing conditions based on the following defect equation in Kroger-Vink notation.

$$O_O^x \rightleftharpoons {}^1\!/_2\, O_2 + V_O^{\cdot\cdot} + 2e' \qquad \text{5-1}$$

The following section (5.3) will investigate the role of dopant mechanisms in the Ruddlesden-Popper $Sr_3Ti_2O_7$ phase. Due to the complex nature of this topic only a single dopant, La, has been chosen since it is the ideal rare earth (RE) ion to substitute onto the Sr-site ($r_{Sr^{2+}} = 1.44$ Å, CN = 12) having a similar ionic radius ($r_{La^{3+}} = 1.36$ Å, CN = 12)[7]. To understand and improve the thermoelectric properties of the La-doped RP phase, $SrO(SrTiO_3)_2$, a more comprehensive understanding of the potential doping mechanisms under different oxygen partial pressures, pO_2, is required. Electronic doping (equation 5-2) has been widely used to create free electrons in the lattice to increase σ of

La-doped $SrTiO_3$ and $Sr_3Ti_2O_7$[8-12]. However, there are at least three compensation mechanisms in La-doped $SrTiO_3$, which can also be dependent on the conditions of synthesis such as pO_2 and temperature[13-15]. These are listed as mechanisms 5-2 to 5-4 and represent electronic compensation, A-site and B-site vacancies, respectively. In the case of RP phases there is a further possibility of oxygen interstitials, as shown in mechanism 5-5. For convenience, they will be denoted as x series/e, y series/V_a and z series/V_b, respectively, for the discussion hereafter.

Of particular interest is the recent report that A-site (Sr) deficiency is found to be beneficial to σ in $La_xSr_{1-3x/2}TiO_3$ compared to stoichiometric compounds ($La_xSr_{1-x}TiO_3$) at the same oxygen partial pressure[16-18]. This may be a consequence of additional oxygen loss in metal deficient compositions that can enhance σ via mechanism 5-1.

$$La_2O_3 + TiO_2 \Rightarrow 2La_{Sr}^{\cdot} + 2e' + Ti_{Ti}^{x} + 3O_O^{x} + 1/2O_2(g) \tag{5-2}$$

$$La_2O_3 + 3TiO_2 \Rightarrow 2La_{Sr}^{\cdot} + V_{Sr}'' + 3Ti_{Ti}^{x} + 9O_O^{x} \tag{5-3}$$

$$2La_2O_3 + 3TiO_2 \Rightarrow 4La_{Sr}^{\cdot} + V_{Ti}'''' + 3Ti_{Ti}^{x} + 12O_O^{x} \tag{5-4}$$

$$La_2O_3 + 2TiO_2 \Rightarrow 2La_{Sr}^{\cdot} + O_i'' + 2Ti_{Ti}^{x} + 6O_O^{x} \tag{5-5}$$

Therefore, in section 5.3 the possible La-doping mechanisms are investigated in the $Sr_3Ti_2O_7$ RP phase in ambient (air) and reducing (N_2/5%H_2) atmospheres for which the associated electrical and power factors are reported. Furthermore, we highlight the influence of heterogeneity associated with resistive surface layers and conductive secondary phases on the electrical properties of ceramics processed under reducing atmospheres. Recognition of these heterogeneities is important,, as processing titanate-based phases under reducing conditions is a common method to induce significant levels of oxygen-loss, mechanism 5-1, and therefore n-type conduction in these materials.

The substitution of Sr with Ca (with smaller ionic radius of 1.34 Å (CN = 12)[7]) is motivated by the attempt to further improve the thermoelectric properties of the La-doped Ruddlesden-Popper phase. The structural distortion (from I4/mmm[19] to $Ccm2_1$[20]) arising from octahedral tilting and A-site cation displacements is expected to introduce disorder, enhance phonon scattering and lower thermal conductivity, especially in reduced ceramics which contain a distribution of $V_O^{\cdot\cdot}$. Therefore, the structure, microstructure and thermoelectric performance of stoichiometric La-doped $Ca_3Ti_2O_7$ ceramics based on an electronic compensation mechanism, section 5.4 are also investigated.

5.2 Undoped $Sr_3Ti_2O_7$

5.2.1 Structure and Microstructure

All $Sr_3Ti_2O_7$ ceramics were sintered at 1773 K for 6 hours. The XRD traces of crushed $Sr_3Ti_2O_7$ pellets sintered in different atmospheres are presented in Figure 5.1. All peaks could be indexed according to the $Sr_3Ti_2O_7$ ([11-633] ICDD card) single RP_2 phase after sintering in N_2 and N_2/5%H_2. Some extra peaks however, for $Sr_4Ti_3O_{10}$ ([76-741] ICDD card) RP_3 phases were detected after sintering in air.

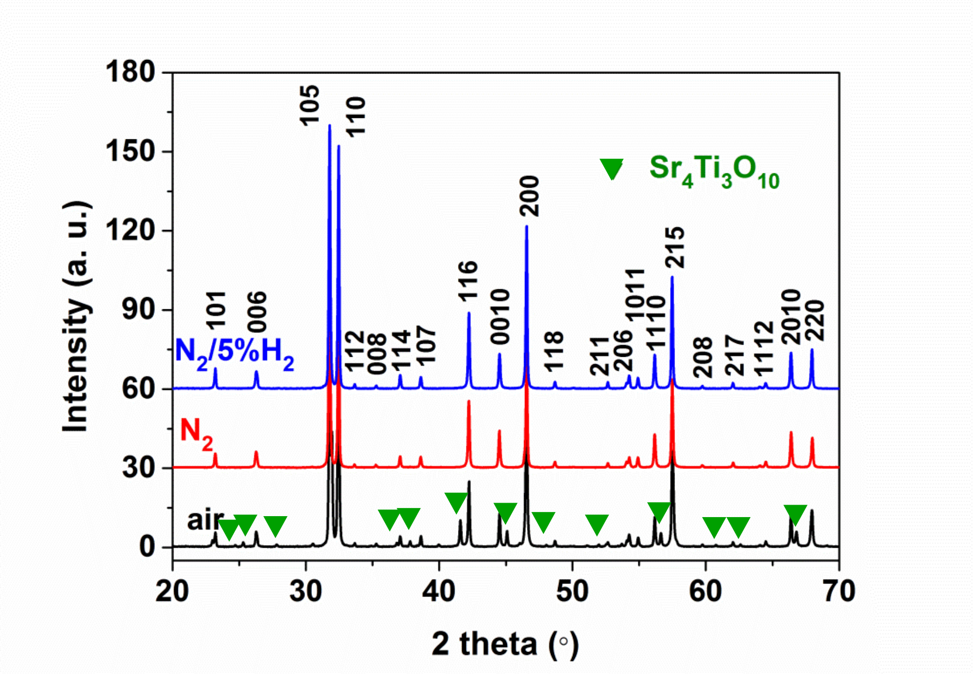

Figure 5.1 XRD traces of crushed $Sr_3Ti_2O_7$ pellets sintered in different atmospheres at 1773 K for 6 hrs.

Secondary electron images of fractured sections of Sr$_3$Ti$_2$O$_7$ pellets sintered in different atmospheres are presented in Figure 5.2. The grain size of the air sintered pellet was slightly smaller than that sintered in reducing atmospheres. Figure 5.3 shows secondary electron images of pellet surfaces sintered in different atmospheres. Tabular morphologies with rod- or plate-like grains (~10 μm) on the surface of the air sintered pellets were observed, Figure 5.3(a). From Figure 5.3(b), the surface of the N$_2$ sintered pellet was composed of spherical and rod- plate-like morphologies (~2 to 5 μm). Irregular block-like morphologies were observed on the surface of pellet sintered in N$_2$/5%H$_2$, Figure 5.3(c).

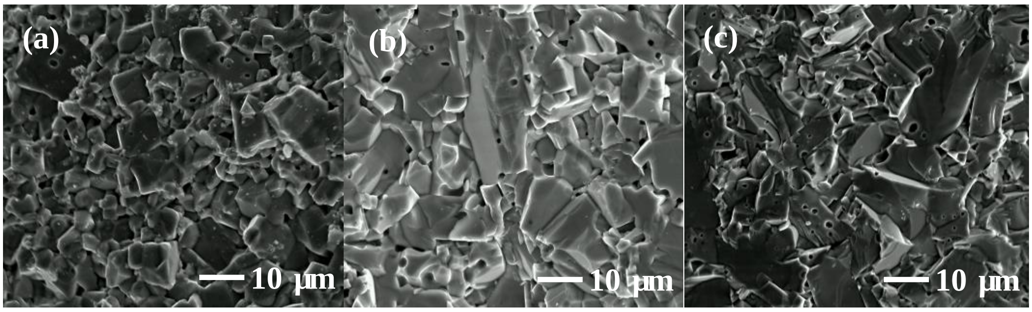

Figure 5.2 Secondary electron images of the fractured sections of Sr$_3$Ti$_2$O$_7$ pellets sintered at 1773 K for 6 hrs in different atmospheres: (a) air, (b) N$_2$, (c) N$_2$/5%H$_2$.

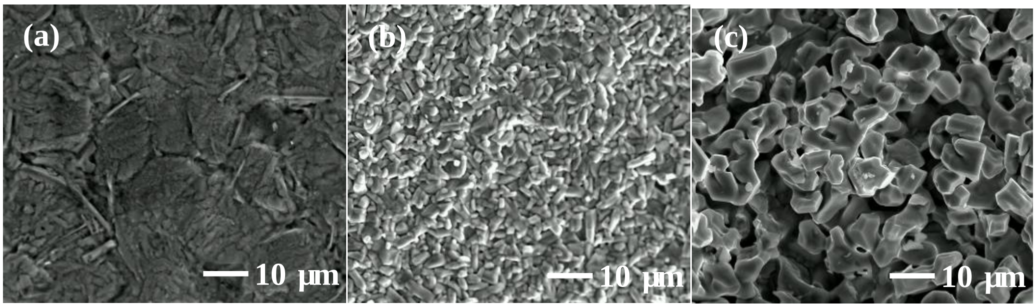

Figure 5.3 Secondary electron images of the surfaces of Sr$_3$Ti$_2$O$_7$ pellets sintered at 1773 K for 6 hrs in different atmospheres: (a) air, (b) N$_2$, (c) N$_2$/5%H$_2$.

The colour of undoped $Sr_3Ti_2O_7$ ceramics sintered in N_2/5%H_2 ($Sr_3Ti_2O_{7-\delta}$) was dark green suggesting that oxygen-loss with partial reduction of Ti^{4+} to Ti^{3+} ions had occurred within the ceramics. XRD was performed on the surface of undoped $Sr_3Ti_2O_{7-\delta}$ ceramics and on powder from crushed pellets sintered in N_2/5%H_2, Figure 5.4. The XRD pattern for the powder of crushed pellets fully indexed to $Sr_3Ti_2O_7$ ([11-633] ICDD card); however, the XRD pattern for the ceramic surface contained many additional reflections. Some of these are associated with a simple $SrTiO_3$-type cell (presumably oxygen-deficient and referred thereafter as $SrTiO_{3-\delta}$) due to the high temperature and low pO_2 employed during the synthesis. However, there are other reflections that do not index to any known phase in the ICDD database.

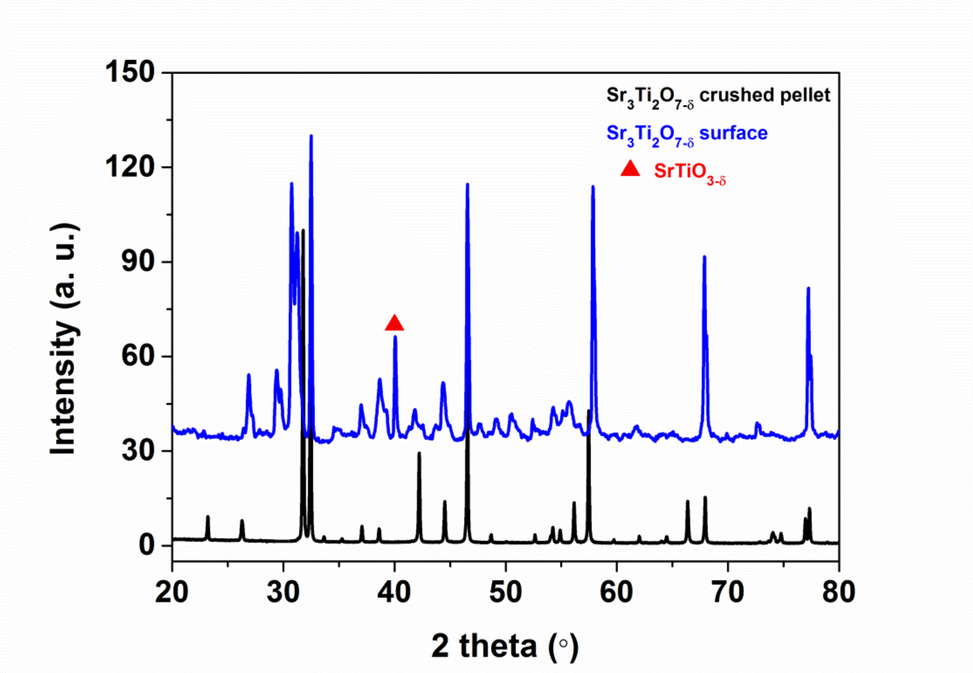

Figure 5.4 XRD traces of powder from a crushed $Sr_3Ti_2O_{7-\delta}$ pellet sintered at 1773 K for 6 hrs in N_2/5%H_2 (lower) and its surface (upper) prior to crushing.

Backscattered electron images (BEI) on a cross section of a $Sr_3Ti_2O_{7-\delta}$ pellet sintered in N_2/5%H_2 are shown in Figure 5.5. The BEI demonstrates clear evidence for the presence of a surface layer with a different composition to that of the ceramic interior. EDS analysis showed the Sr/Ti ratio to be lower in the surface layer (Sr/Ti ~1) compared to the interior of the ceramic (Sr/Ti ~3/2), Table 1.

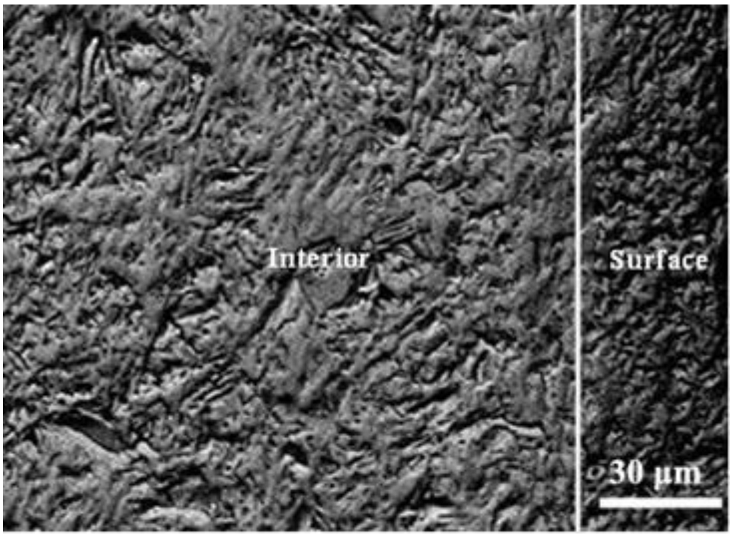

Figure 5.5 Backscattered electron images on a cross section of a $Sr_3Ti_2O_{7-\delta}$ pellet sintered at 1773 K for 6 hrs in N_2/5%H_2.

Table 5.1 Relative percentage of Sr, Ti and the Sr/Ti ratio from the interior and surface regions of $Sr_3Ti_2O_{7-\delta}$ ceramic sintered in N_2/5%H_2 at 1773 K. Theoretical values for $Sr_3Ti_2O_7$ are Sr = 60.00 %, Ti = 40.00 % with Sr/Ti = 1.50 and Sr = 50.00 %, Ti = 50.00 % with Sr/Ti = 1.00 for $SrTiO_3$.

Element	**Bulk**			**Surface layer**		
	Sr L	Ti K	Sr/Ti	Sr L	Ti K	Sr/Ti
Relative %	59.31	40.69	1.46	52.76	47.24	1.12
	62.08	37.92	1.64	52.14	47.86	1.09
	62.25	37.75	1.65	53.08	46.92	1.13
	62.61	37.39	1.67	53.37	46.63	1.14
	59.80	40.20	1.49	50.58	49.42	1.02
	60.98	39.02	1.56	49.88	50.12	1.00
Average Relative %	61.17	38.83	1.58	51.97	48.03	1.08

Figure 5.6 compares simulated (using CaRine software[21]) and experimental electron diffraction patterns of $Sr_3Ti_2O_7$ along $[100]_{I4/mmm}$ and $[110]_{I4/mmm}$ directions, respectively. Compared to the $SrTiO_3$ <100> electron diffraction pattern, weak reflections related to the number of perovskite layers in the RP phase are observed at e.g., $\{002\}_{I4/mmm}$, $\{004\}_{I4/mmm}$, $\{006\}_{I4/mmm}$ and $\{008\}_{I4/mmm}$ (0kl: k + l = 2n[22]). Bright field TEM images along [110] of $Sr_3Ti_2O_7$ samples sintered in air and $N_2/5\%H_2$ are shown in Figure 5.7, illustrating that oxygen loss leads to the formation of planar defects that exhibit strong strain contrast, consistent with the presence of dislocations or high strain stacking faults in the $Sr_3Ti_2O_7$ matrix, Figure 5.7(b). Samples sintered in air do not exhibit such high strain contrast defects but occasionally show regions of low strain stacking faults, related to disorder of the SrO layer along the c-axis, Figure 5.7(a).

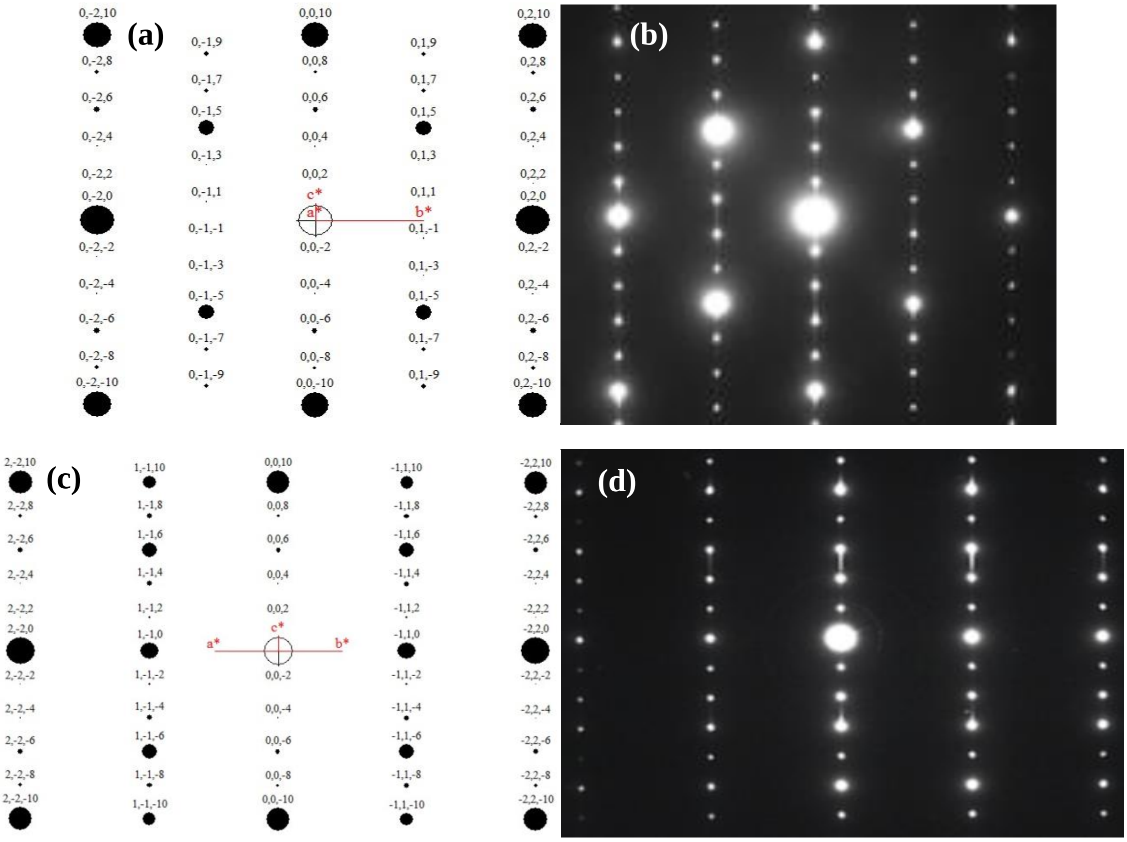

Figure 5.6 (a), (b) $[100]_{I4/mmm}$ simulated and electron diffraction patterns; (c), (d) $[110]_{I4/mmm}$ simulated and electron diffraction patterns of $Sr_3Ti_2O_7$ ceramics sintered at 1773 K for 6 hrs in air.

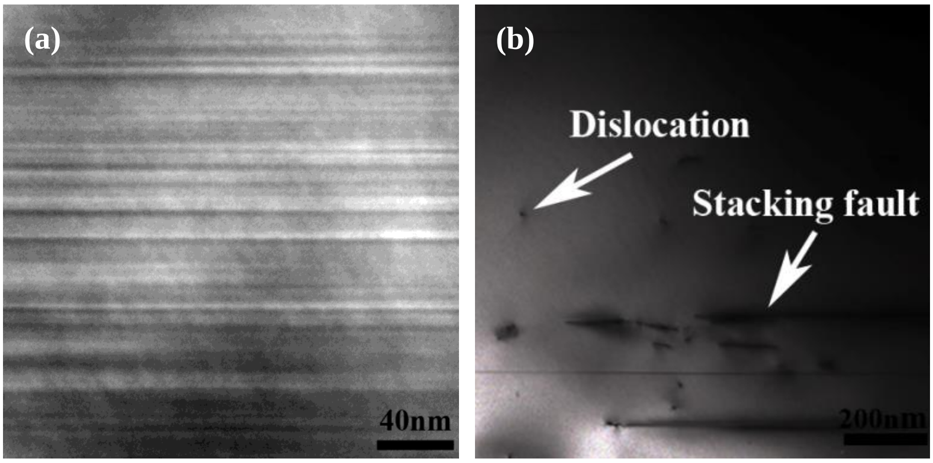

Figure 5.7 Bright field images along [110] direction of $Sr_3Ti_2O_7$ ceramics sintered at 1773 K for 6 hrs in air and N_2/5%H_2.

5.2.2 Electrical Properties

Typical Z* plots at RT for unpolished and polished $Sr_3Ti_2O_{7-\delta}$ ceramics sintered in N_2/5%H_2 were dramatically different, Figure 5.8. A Z* plot for an unpolished ceramic was dominated by a single, large arc that could not be fully resolved as the total resistivity of the sample exceeded 10 MΩ cm, Figure 5.8(a). In contrast, the Z* plot for the polished pellet shows a single arc with a total sample resistivity of ~40 kΩ cm at RT, Figure 5.8(b). This indicates that the as-sintered ceramic contains a resistive surface layer. Using the relationship $\omega RC = 1$ at the arc maximum in Figure 5.8(b) shows the associated capacitance, C, of this arc to be 173 μF/cm, consistent with a non-ohmic contact between the polished ceramic and the metal electrode. This assignment was confirmed by applying a small dc bias (<2 V) to the IS measurements which reduced the diameter of the arc and therefore the magnitude of the non-ohmic electrode contact (not shown). Inspection of high frequency data in the RT Z* plot shows the presence of a non-zero intercept of ~4 Ωcm associated with the total resistivity of the ceramic, Figure 5.8(c). Cryogenic measurements were performed in an attempt to quantify the bulk (grain) response via the presence of a high frequency Debye peak in the imaginary component of the electric modulus M″ spectrum[23, 24]. A combined -Z″ and M″ spectroscopic plot at 10 K shows a low frequency -Z″ Debye peak associated with the resistive, non-ohmic contact, however, the M″ spectrum shows an incline at high frequency indicating that the grain (bulk) response remains too conductive to measure by IS, Figure 5.8(d) at 10 K. The M″ Debye peak at intermediate frequency is attributed to a thin layer (electrode/surface) response, Figure 5.8(d), but was not investigated in detail.

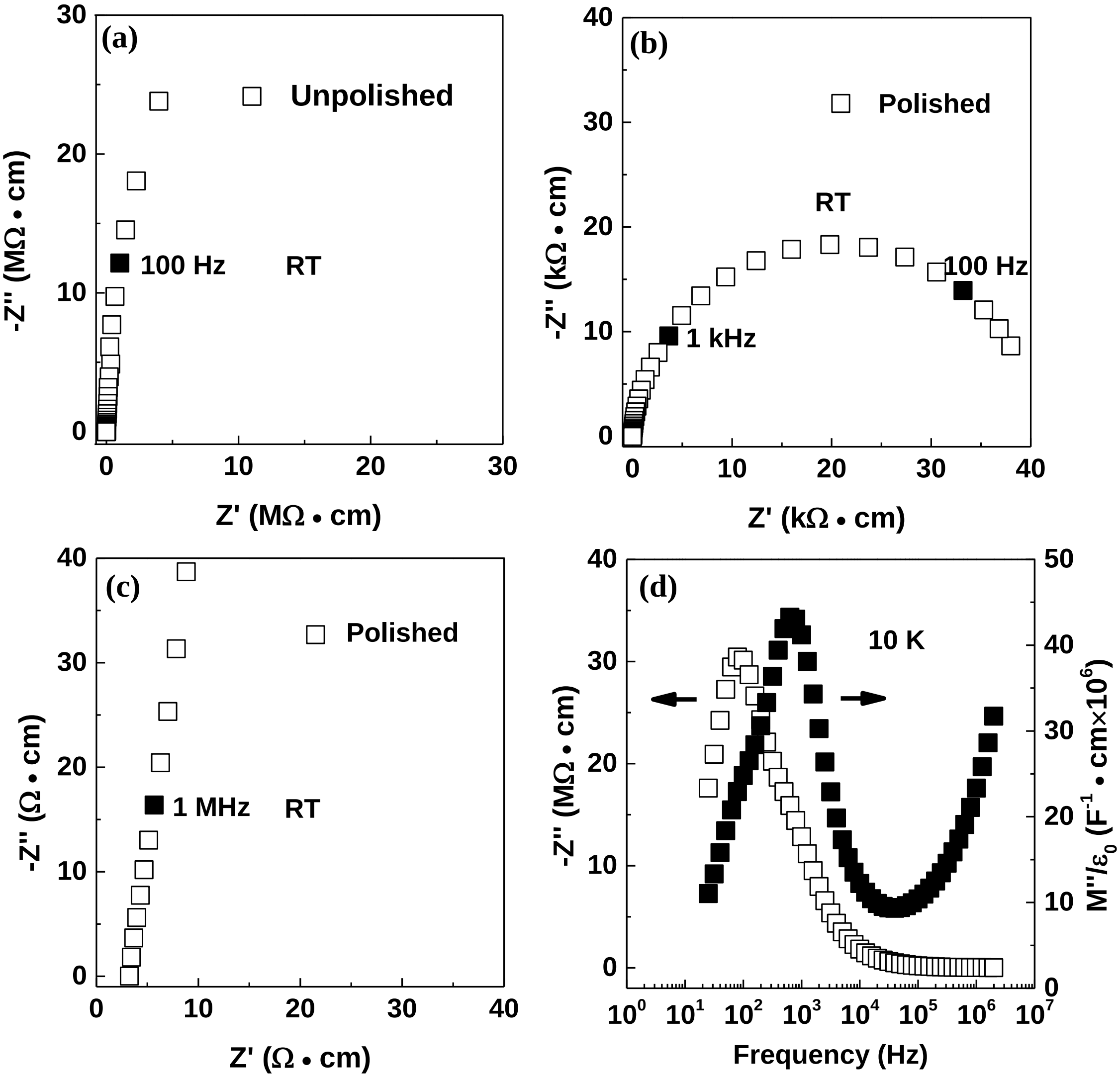

Figure 5.8 Typical RT Z* plots of (a) an unpolished Sr$_3$Ti$_2$O$_{7-\sigma}$ pellet, (b) a polished pellet, (c) inspection of high frequency data of (b); (d) combined -Z″ and M″ spectra of a polished Sr$_3$Ti$_2$O$_{7-\delta}$ pellet at 10 K, sintered at 1773 K for 6 hrs in N$_2$/5%H$_2$.

The influence of a dc bias on the N$_2$/5%H$_2$ sintered ceramic at room temperature is presented in Figure 5.9. The arc corresponded to an electrode effect (i.e. a non-ohmic contact) decreased with increasing dc bias. A Mott-Schottky plot (1/C^2 against dc bias) was in the shape of a straight line (Figure 5.9(b)). The high capacitance plateau at low frequency increased slightly with increasing dc bias but the higher frequency capacitance was unchanged.

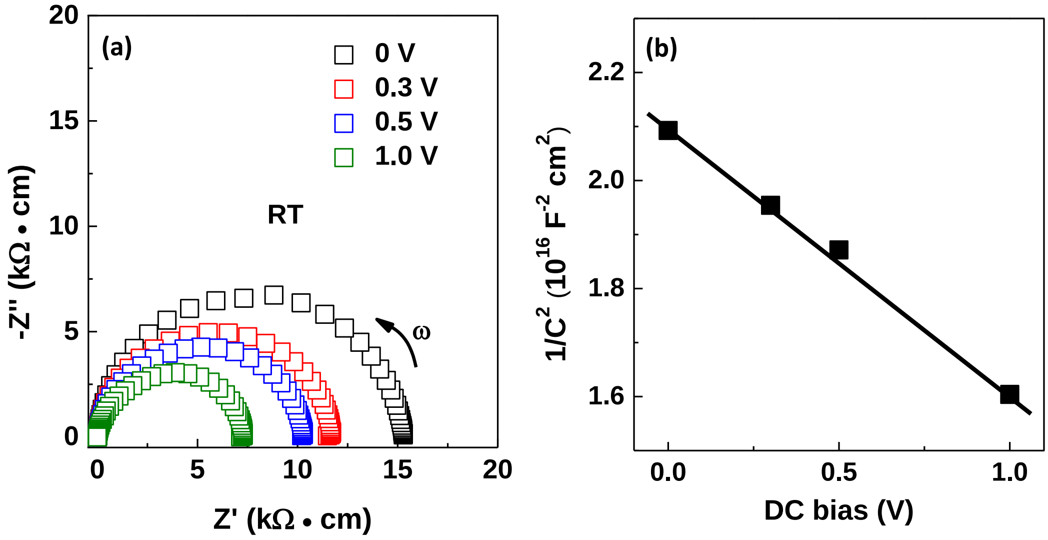

Figure 5.9 (a) Z* plots of a polished Sr$_3$Ti$_2$O$_{7-\delta}$ pellet sintered at 1773 K for 6 hrs in the N$_2$/5%H$_2$ under different dc bias. (b) Mott-Schottky plot of the capacitance associated with the non-ohmic electrode response shown in (a).

5.3 La-doped Sr$_3$Ti$_2$O$_7$

5.3.1 Structure and Microstructure

All doped samples (irrespective of e, V$_a$ or V$_b$) prepared in air were off-white in appearance and were all phase mixtures by XRD with the exception of x = 0.01 for the electronic series. Secondary phases identified included a perovskite-type SrTiO$_3$ for the e and V$_a$ series, a B-site deficient hexagonal-type perovskite SrLa$_4$Ti$_4$O$_{15}$ and an anion-excess layered-perovskite SrLa$_4$Ti$_5$O$_{17}$ for the V$_b$ series. Identifying low levels of perovskite-type SrTiO$_3$ as a secondary phase was challenging for the e series but was confirmed in x = 0.05 composition by the appearance of an additional reflection in the XRD patterns at ~40 degrees two theta (hkl = 111), Figure 5.10(a) and was confirmed by TEM (discussed later). The XRD pattern for powder from crushed pellets of x = 0.01 composition fully indexed to $Sr_3Ti_2O_7$ ([11-633] ICDD card) and there was an expansion of the unit cell volume compared to undoped $Sr_3Ti_2O_7$ prepared in air, Figure 5.10(c).

In contrast, the $N_2/5\%H_2$ sintered, electronic compensation series ceramics were single-phase by XRD up to x = 0.05. A simple cubic-type perovskite $SrTiO_{3-\delta}$ (ST) second phase (Figure 5.10(b)) was observed for x = 0.10 sintered in $N_2/5\%H_2$. The XRD patterns of the $Sr_3Ti_2O_7$-type phase in all samples were indexed on a tetragonal unit cell (space group I4/mmm) as reported in the literature[19]. XRD also showed observable secondary phases including ST, Sr_2TiO_4 and $Sr_4Ti_3O_{10}$ for the V_a and V_b series (not shown) for all values of y and z. The electronic series lattice parameter and unit cell volume values decreased smoothly with increasing x, Figures 5.10(c) and (d) respectively, therefore confirming the existence of a larger extent of solid solution when compared to ceramics prepared in air.

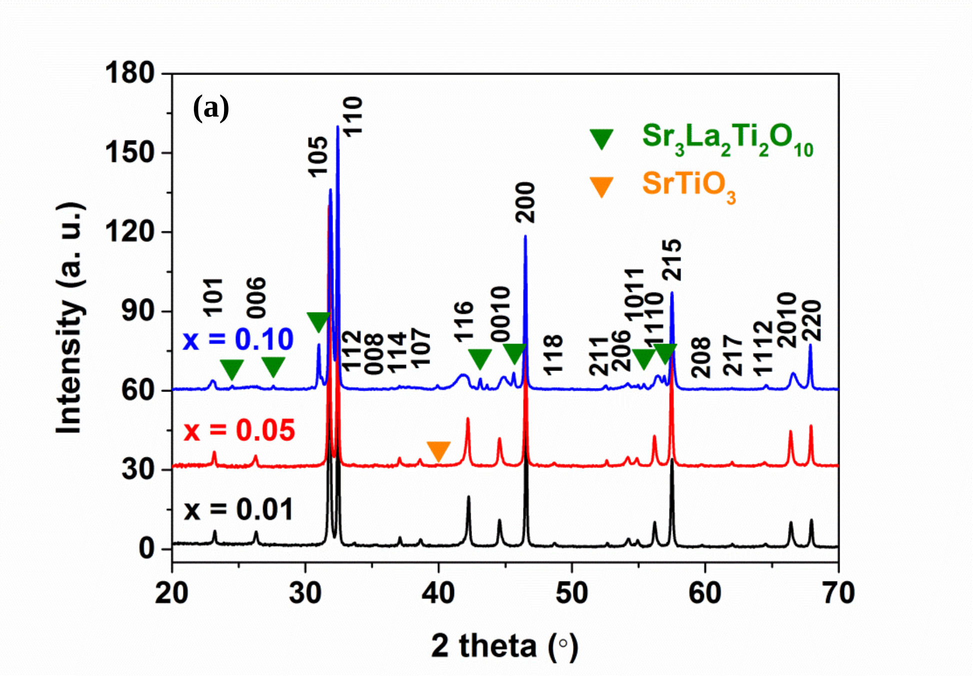

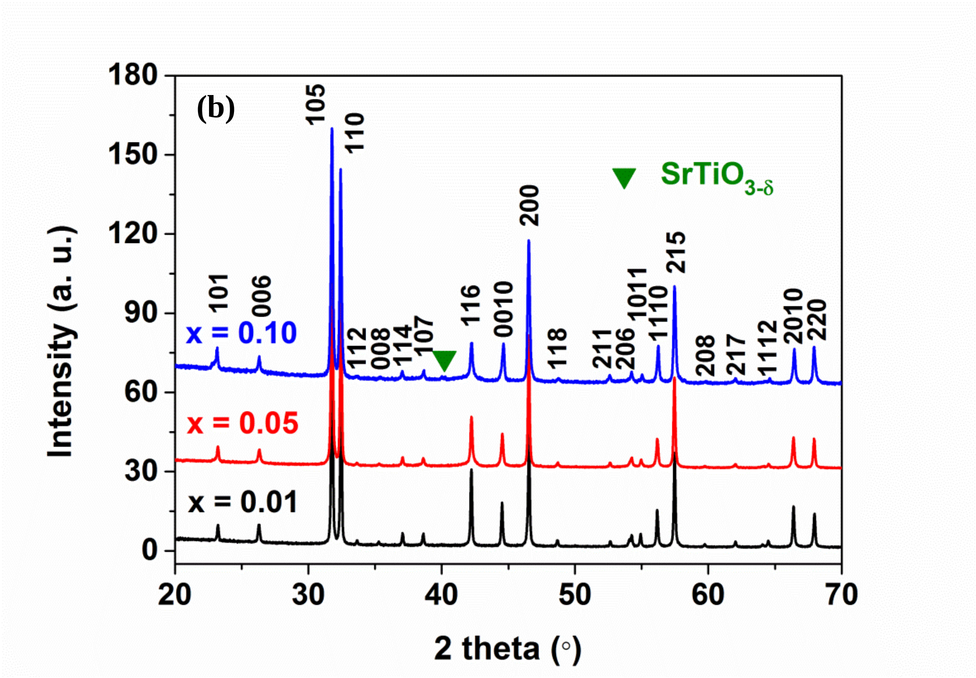
(b)
Intensity (a. u.)
2 theta (◦)
0
30
60
90
120
150
180
20
30
40
50
60
70
▼ SrTiO$_{3-\delta}$
x = 0.10
x = 0.05
x = 0.01
101
006
105
110
112
008
114
107
116
0010
200
118
211
206
1011
1110
215
208
217
1112
2010
220

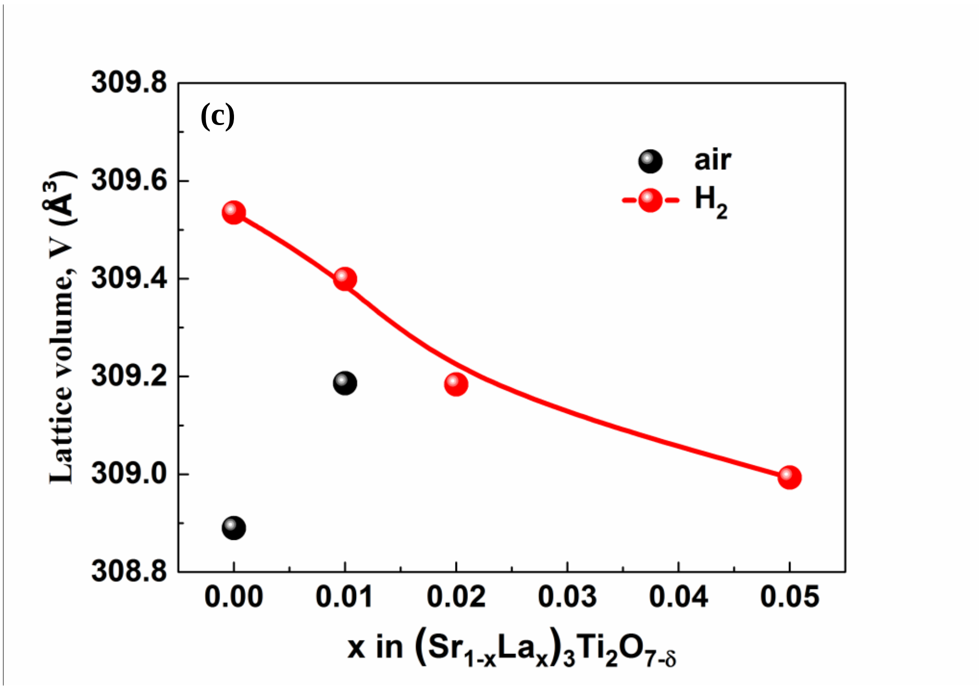
(c)
Lattice volume, V (Å^3)
x in (Sr$_{1-x}$La$_x$)$_3$Ti$_2$O$_{7-\delta}$
308.8
309.0
309.2
309.4
309.6
309.8
0.00
0.01
0.02
0.03
0.04
0.05
air
H$_2$

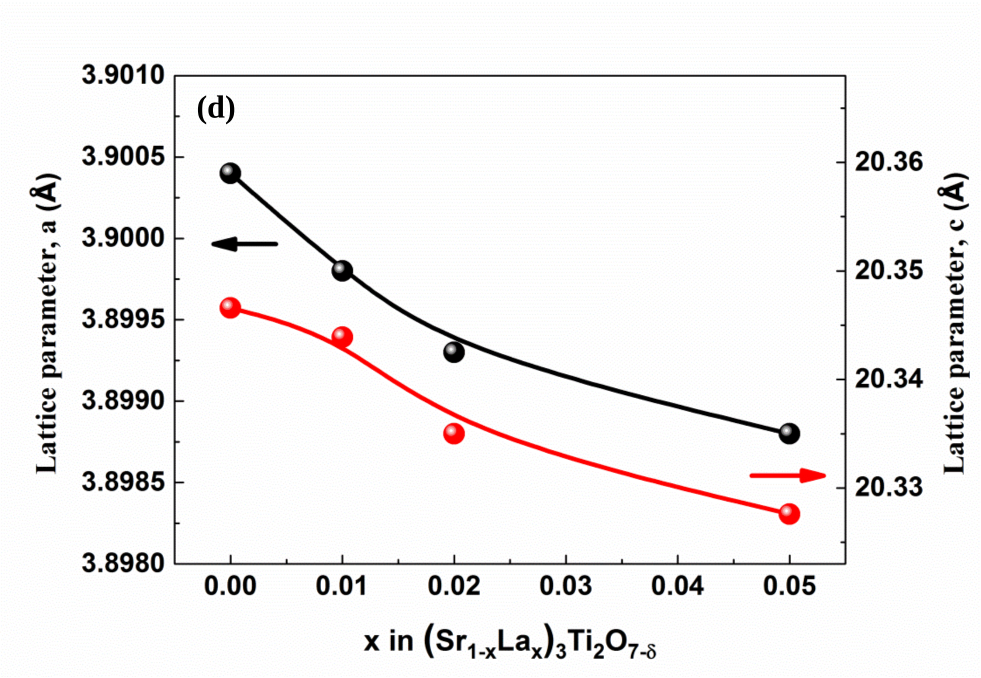

Figure 5.10 XRD patterns for $(Sr_{1-x}La_x)_3Ti_2O_7$ ceramics sintered at 1773 K for 6 hrs: (a) air sintered, (b) N_2/5%H_2 sintered, (c) unit cell volume sintered in air (black filled circles) and N_2/5%H_2 (red filled circles), (d) lattice parameters for N_2/5%H_2 sintered ceramics.

Secondary electron images of fracture surfaces for x = 0.01 and 0.05 sintered in N_2/5%H_2 show the former to have a much larger average grain size compared to the latter, Figure 5.11. The mechanism of grain growth under reducing conditions is not known at this stage.

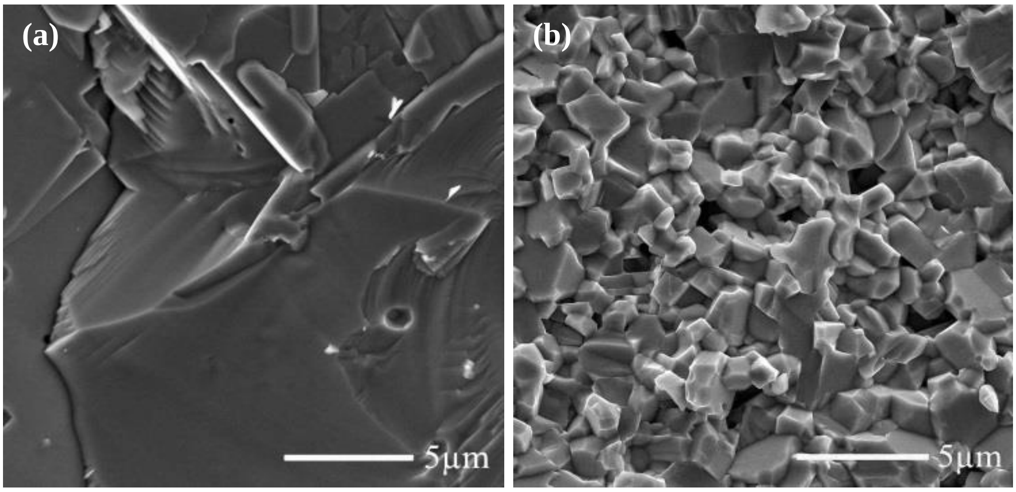

Figure 5.11 Secondary electron images of a fractured surface for (a) x = 0.01 and (b) x = 0.05 ceramics sintered at 1773 K for 6 hrs in N_2/5%H_2.

TEM images of $(Sr_{1-x}La_x)_3Ti_2O_7$ (x = 0.01, 0.05) ceramics sintered in air and N_2/5%H_2 obtained close to [110] are presented in Figure 5.12. The [110] zone axis contains the (001) plane and thus reveals information about the SrO layers and any defects in the stacking sequence, particularly in samples that were tilted off-axis to give two beam bright field diffraction contrast conditions. Faint planar defects in these images represent essentially unstrained stacking faults in the RP superstructure, as shown in Figure 5.12(c) for x = 0.01 processed in N_2/5%H_2. Unstrained stacking faults are typical of RP phases and are regions in which the SrO layer is disordered along the *c*-axis. Darker contrast planar defects were observed, e.g. for x = 0.01 processed in air, Figure 5.12(a) and arose because of deviations as a function of distance from a coherent Bragg condition and were associated with local lattice strain. Comparing Figure 5.12(b) and (d) (x = 0.05, sintered in air and N_2/5%H_2, respectively) the main difference is the clear formation of discrete blocks of $SrTiO_3$ in air sintered samples interleaved between the RP phase. In contrast, the grains in x = 0.05 sintered in N_2/5%H_2 remained essentially single-phase RP-type $Sr_3Ti_2O_7$, despite evidence of strained stacking faults in Figure 5.12(d). Note that similar defects were observed in undoped samples sintered in N_2/5%H_2, Figure 5.7(b).

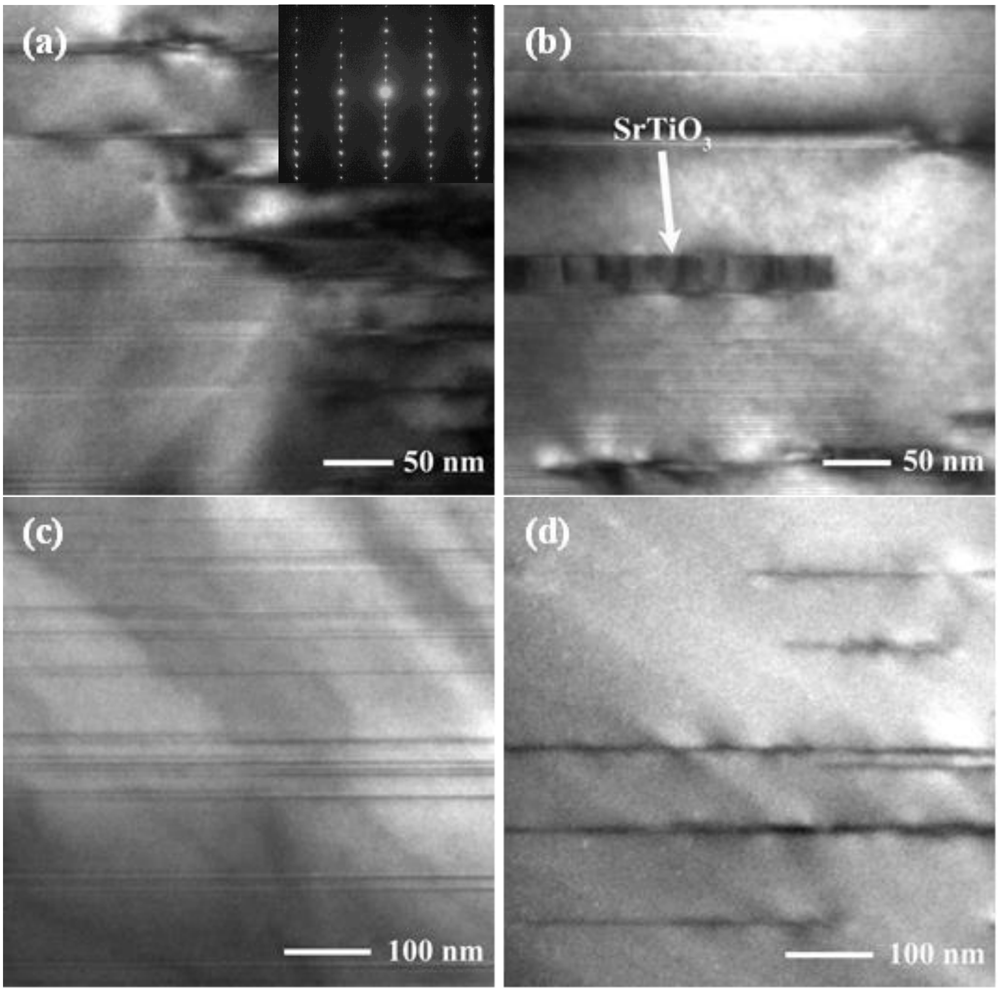

Figure 5.12 Two beam bright field TEM images of (Sr$_{1-x}$La$_x$)$_3$Ti$_2$O$_7$ ceramics sintered at 1773 K for 6 hrs obtained with the electron beam close to [110], (a) x = 0.01, (b) x = 0.05 sintered in air and (c) x = 0.01 and (d) x = 0.05 sintered in N$_2$/5%H$_2$.

5.3.2 Electrical and Thermoelectric Properties

IS measurements were employed to study the electrical properties of Sr$_3$Ti$_2$O$_7$ ceramics sintered in air. The high frequency arc in the impedance complex plane, Z*, plots was used to extract the bulk (grain) resistivity, (ρ_b) of undoped Sr$_3$Ti$_2$O$_7$ and x = 0.01 ceramics sintered in air. The bulk conductivity, $\sigma_b = 1/\rho_b$, plotted in Arrhenius-format showed x, y and z ceramics to have lower conductivity (~1 to 1.5 orders of magnitude at ~893 K) and a significantly higher activation energy for bulk conduction, E$_a$, (by ~1 eV) compared to undoped $Sr_3Ti_2O_7$, Figure 5.13.

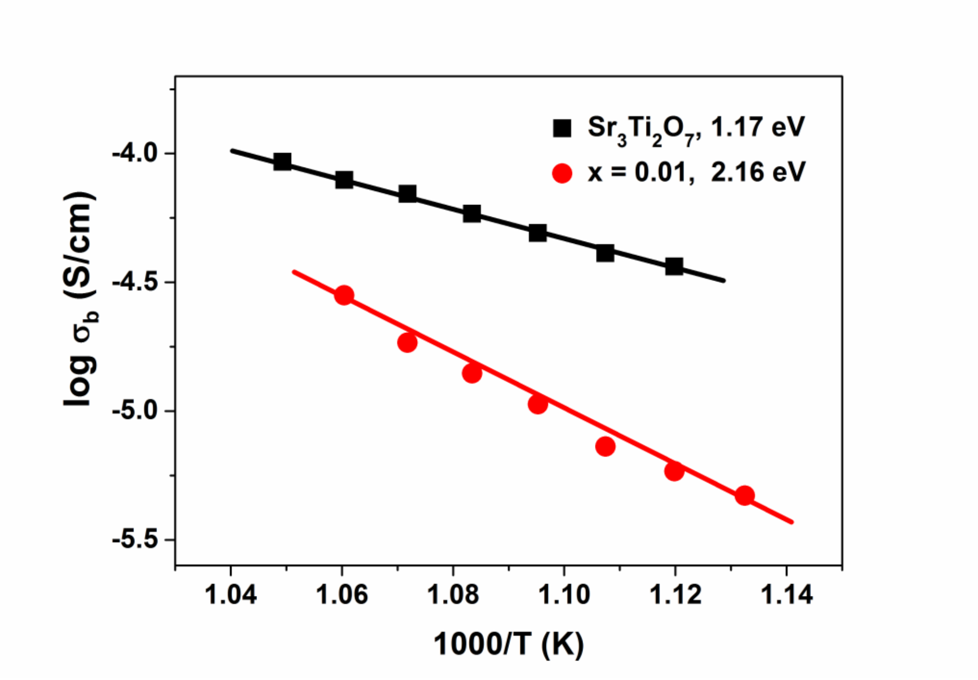

Figure 5.13 Arrhenius plots of σ_b for undoped $Sr_3Ti_2O_7$ (filled black squares) and x = 0.01 (filled red circles) ceramics sintered at 1773 K for 6 hrs in air.

For La-doped samples sintered in N_2/5%H_2, the development of resistive surface layers on ceramics also occurred and was attributed (in part) to the uptake of oxygen during the post-sintering cooling process in N_2/5%H_2. In an attempt to minimise the deleterious influence of any re-oxidation on σ (reverse reaction of mechanism 5-1), 4 probe resistivity measurements were performed on polished bars of x = 0.005 ceramics sintered in N_2/5%H_2 with various cooling rates. The temperature dependence of σ showed it to be highest and reproducible for ceramics prepared with cooling rates ≥ 5 ^{o}C/min, Figure 5.14. The results presented below for the thermoelectric properties are therefore for ceramics prepared with a cooling rate of 30 ^{o}C/min to minimise the influence of re-oxidation on σ.

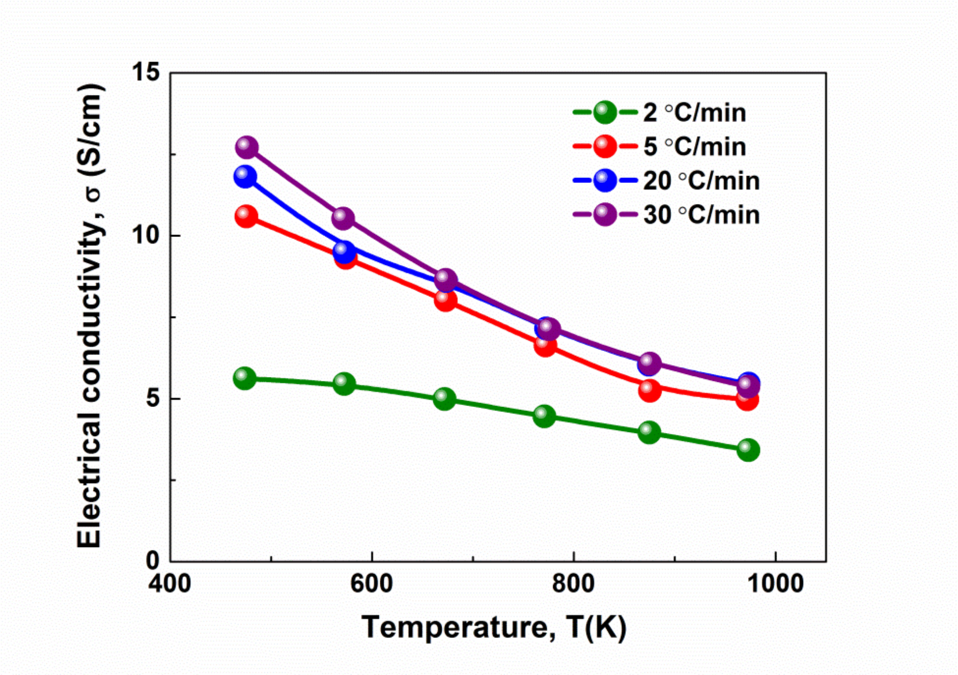

Figure 5.14 4-probe σ versus temperature of $(Sr_{0.995}La_{0.005})_3Ti_2O_{7-\delta}$ ceramics sintered at 1773 K for 6 hrs in N_2/5%H_2 with different cooling rates.

S values for the x series were negative, suggesting all samples are n-type semiconductors. The absolute S value became smaller with increasing x, Figure 5.15(a), possibly due to an increase in the carrier concentration, Figure 5.15(b). Comparison of σ at 973 K showed it to increase with x, however x = 0.01 exhibited metallic conduction whereas all other x values correspond to semiconducting behaviour. The power factor (PF) had the same trend as σ with temperature and reached a maximum of ~70 $\mu Wm^{-1}K^{-2}$ for x = 0.10 at ~973 K due to its high σ, Figure 5.15(c). x = 0.10 contained the presence of a secondary ST phase and this had a dramatic effect on the thermoelectric properties.

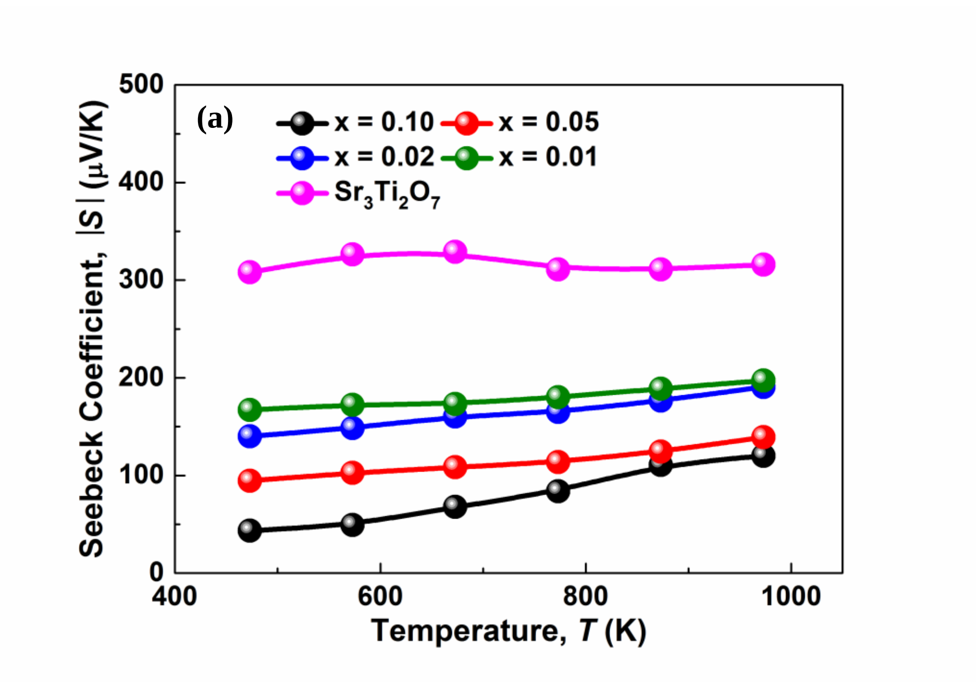
(a)
x = 0.10
x = 0.05
x = 0.02
x = 0.01
Sr3Ti2O7
Seebeck Coefficient, |S| (μV/K)
0
100
200
300
400
500
400
600
800
1000
Temperature, T (K)

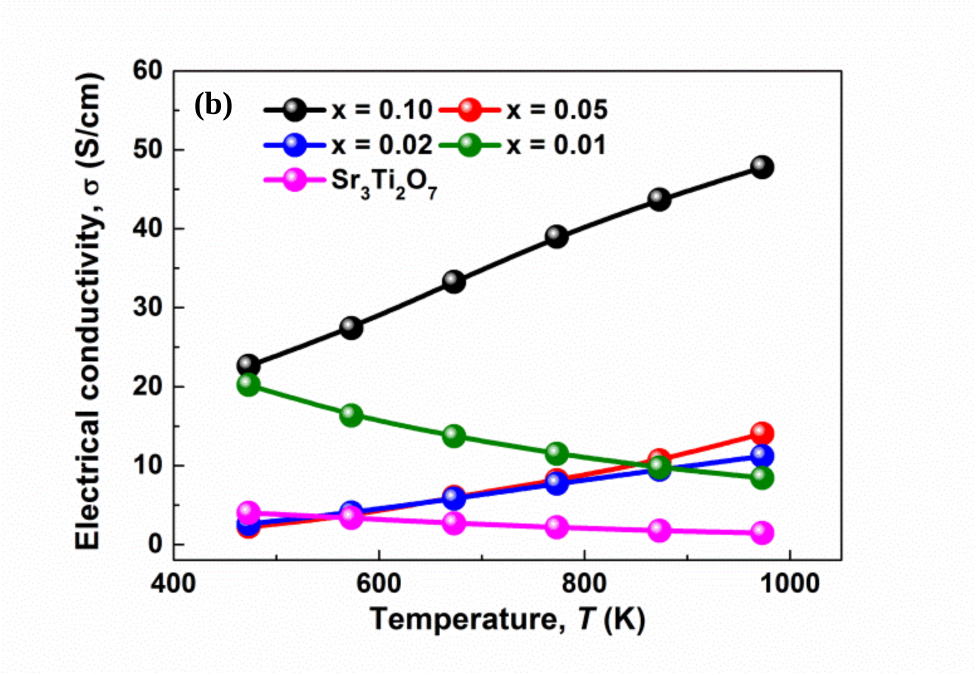
(b)
x = 0.10
x = 0.05
x = 0.02
x = 0.01
Sr3Ti2O7
Electrical conductivity, σ (S/cm)
0
10
20
30
40
50
60
400
600
800
1000
Temperature, T (K)

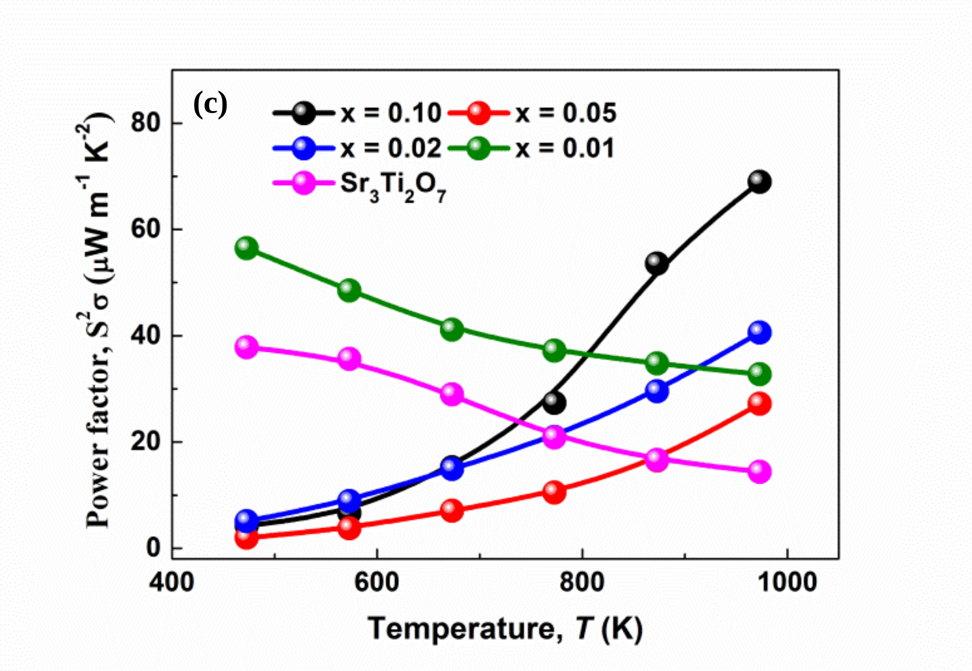

Figure 5.15 Temperature dependence of (a) S, (b) σ, and (c) PF = $S^2\sigma$ for electronic compensation series sintered at 1773 K for 6 hrs in N_2/5%H_2.

The variation of PF with La-content in $Sr_3Ti_2O_{7-\delta}$ ceramics based on the three compensation mechanisms at 973 K is shown in Figure 5.16 and reveals the highest PF of a single-phase ceramic to be obtained for x = 0.02. Interestingly, significantly higher PF values were observed for ceramics that were phase mixtures, e.g. x = 0.10 and all of y and z series contained an ST secondary phase.

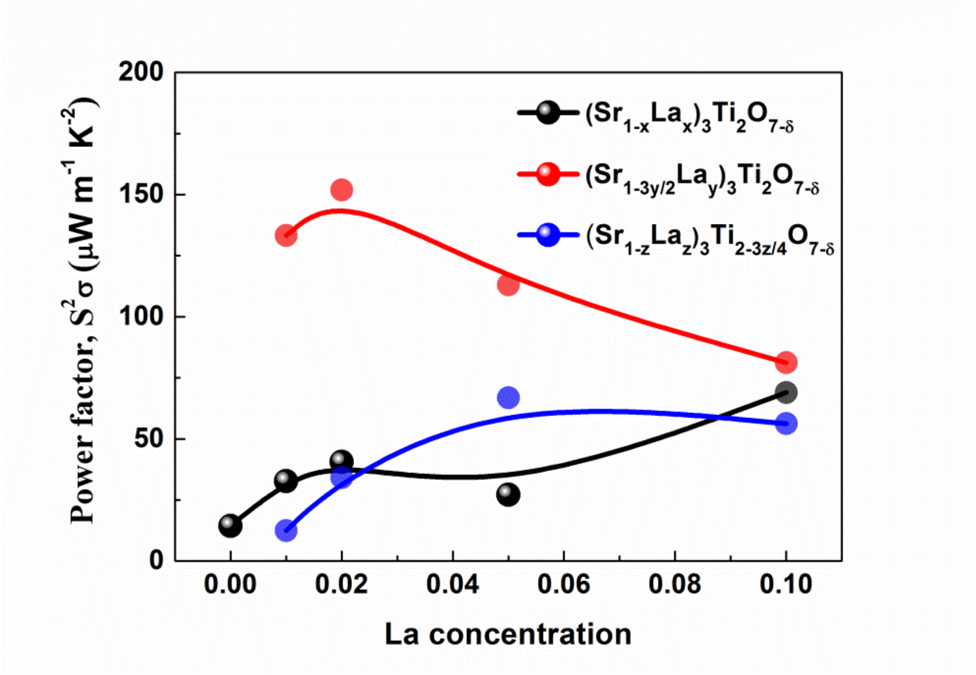

Figure 5.16 PF at 973 K versus La-content in $Sr_3Ti_2O_{7-\delta}$ ceramics sintered at 1773 K for 6 hrs in N_2/5%H_2 based on compositional series x, y and z.

5.4 La-doped $Ca_3Ti_2O_7$

For controlling the thermal conductivity without destroying the power factor of the Ruddlesden-Popper phase, $(Ca_{1-x}La_x)_3Ti_2O_7$ ($x = 0.00, 0.01, 0.02, 0.05$) ceramics have been investigated to try to disrupt phonon modes further by invoking octahedral tilting to achieve lower thermal conductivity.

5.4.1 Structure and Microstructure

The XRD traces of crushed $(Ca_{1-x}La_x)_3Ti_2O_7$ ($x = 0.00, 0.01, 0.02, 0.05$) samples sintered in N_2/5%H_2 are presented in Figure 5.17. All major peaks for $Ca_3Ti_2O_7$ samples could be indexed according to ICDD [78-2480] data. However, extra peaks associated with the presence of $Ca_4Ti_3O_{10}$ were detected in all La-doped $Ca_3Ti_2O_7$ samples. Figure 5.18 shows secondary electron images of the fractured sections of $(Ca_{1-x}La_x)_3Ti_2O_7$ ($x = 0, 0.01, 0.02, 0.05$) samples. The grain size of x = 0.05 was the largest.

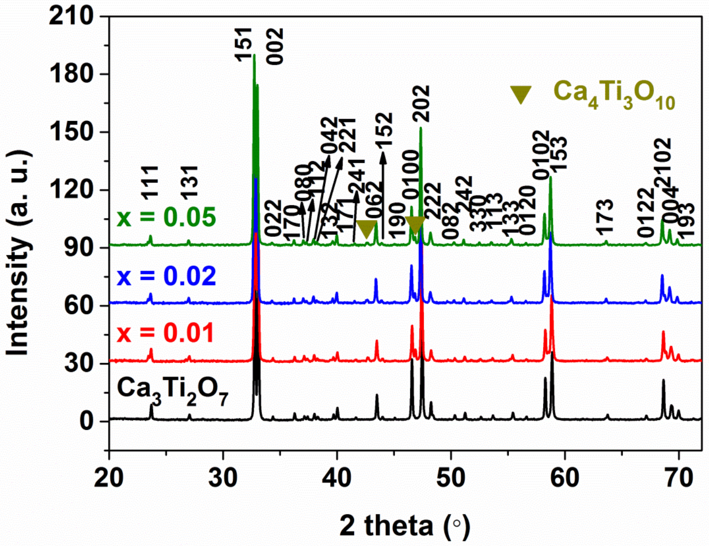

Figure 5.17 XRD traces of crushed $(Ca_{1-x}La_x)_3Ti_2O_7$ (x = 0, 0.01, 0.02, 0.05) samples sintered at 1773 K for 6 hrs in N_2/5%H_2.

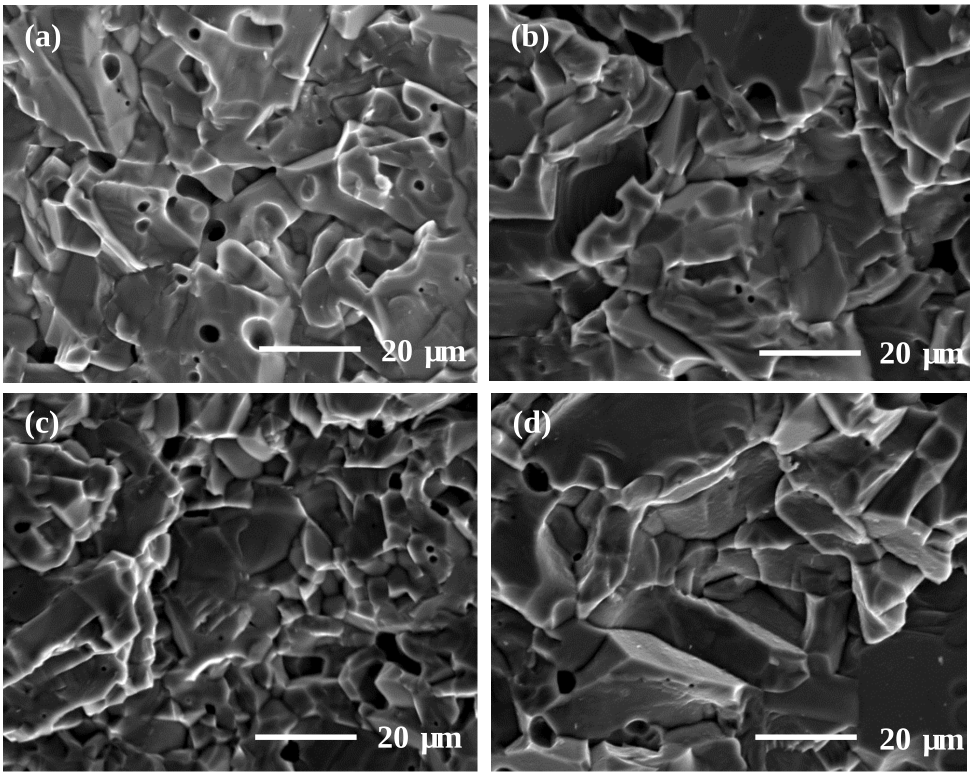

Figure 5.18 Secondary electron images of the fractured sections of $(Ca_{1-x}La_x)_3Ti_2O_7$ samples sintered at 1773 K for 6 hrs in N_2/5%H_2: (a) x = 0, (b) x = 0.01, (c) x = 0.02, (d) x = 0.05.

A dark field image of a ferroelastic boundary in air sintered Ca$_3$Ti$_2$O$_7$ is shown in Figure 5.19. The electron diffraction patterns in Figure 5.20 were from either side of the domain wall and revealed the absence and presence of superstructure reflections associated with O-octahedral rotations. The circular ribbon-like planar defect was an antiphase boundary (APB) formed by the impingement of regions of O-octahedral rotations that had nucleated out of phase.

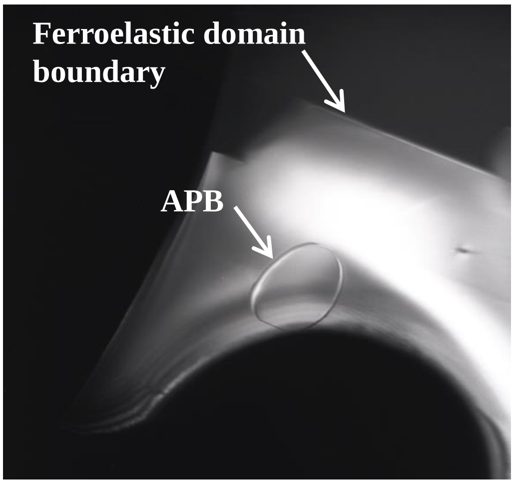

Figure 5.19 Dark field TEM images of Ca$_3$Ti$_2$O$_7$ sintered at 1773 K for 6 hrs in air. The straight line separating dark and light contrast is a ferroelastic domain boundary between two orthorhombic (tilted) variants. The ring is an antiphase boundary (APB) separating regions that have tilted out of phase.

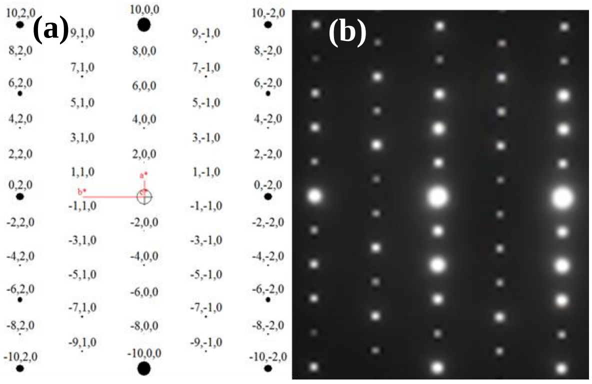

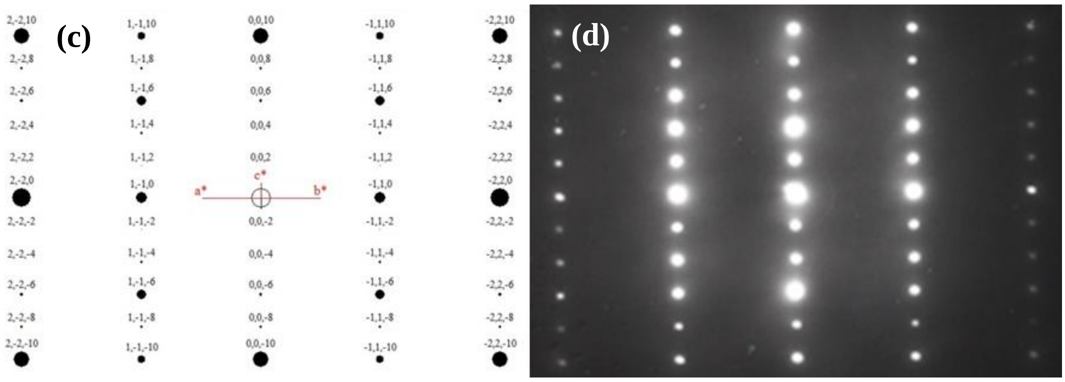

Figure 5.20 (a), (b) $[001]_{CmC21}$ simulated and electron diffraction patterns; (c), (d) $[110]_{I4/mmm}$ simulated and electron diffraction patterns of $Ca_3Ti_2O_7$ ceramics sintered at 1773 K for 6 hrs in air.

TEM images of undoped and $(Ca_{1-x}La_x)_3Ti_2O_{7-\delta}$ (x = 0.05) samples along equivalent pseudotetragonal [110] direction for orthorhombic $Cmc2_1$ structures are presented in Figure 5.21. An antiphase boundary is arrowed which is present inside an orthorhombic variant in the x = 0.05 sample. Weak contrast planar defects are also observed associated with stacking errors of the CaO layers along the *c*-axis.

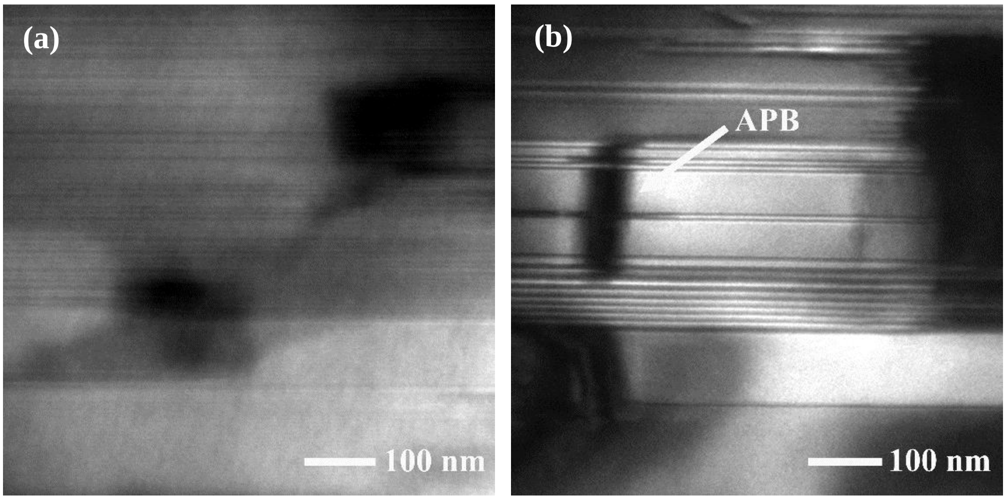

Figure 5.21 TEM images with two beam conditions along $[110]_{I4/mmm}$ of (a) $Ca_3Ti_2O_7$ and (b) $(Ca_{1-x}La_x)_3Ti_2O_{7-\delta}$ (x = 0.05) sintered at 1773 K for 6 hrs in N_2/5%H_2.

5.4.2 Thermoelectric Properties

The temperature dependence of the absolute values of Seebeck coefficient for $(Ca_{1-x}La_x)_3Ti_2O_{7-\delta}$ (x = 0.00, 0.01, 0.02, 0.05) are presented in Figure 5.22(a). The negative S values indicated that La-doped $Ca_3Ti_2O_7$ samples are also n-type semiconductors. The absolute S values were of the same order of magnitude with increasing temperature and became smaller with increasing La-doping level. The temperature dependence of electrical conductivity is given in Figure 5.22(b). The electrical conductivity increased with increasing La-doping level. The undoped $Ca_3Ti_2O_7$ exhibited the smallest electrical conductivity value and oxidised easily when the temperature exceeded ~673 K. The largest power factor was achieved for $(Ca_{1-x}La_x)_3Ti_2O_{7-\delta}$ (x = 0.05) due to its highest electrical conductivity, Figure 5.22(c).

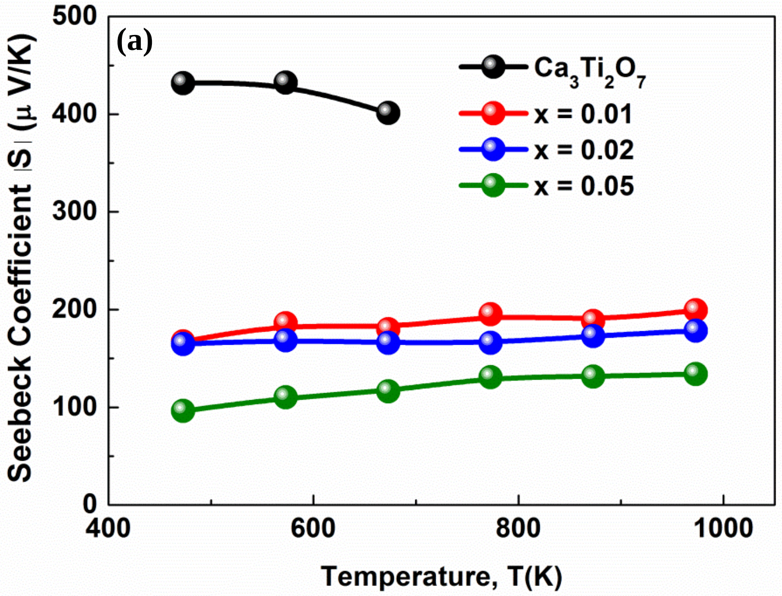

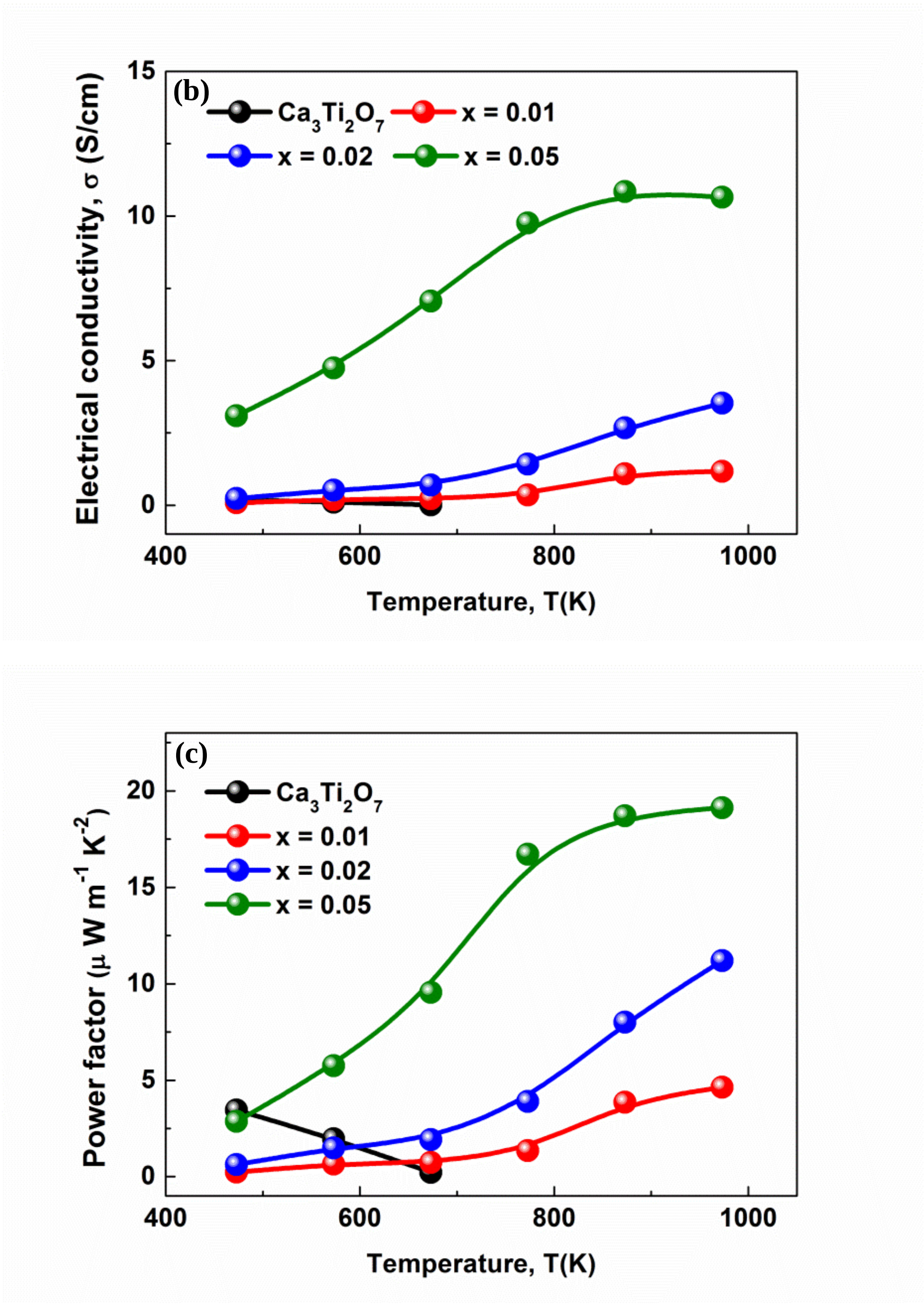

Figure 5.22 Temperature dependence of (a) S, (b) σ, and (c) PF = $S^2\sigma$ for $(Ca_{1-x}La_x)_3Ti_2O_{7-\delta}$ sintered at 1773 K for 6 hrs in the N_2/5%H_2.

5.5 Discussion and Conclusion

Undoped $Sr_3Ti_2O_7$

From Figure 5.1, single phase $Sr_3Ti_2O_7$ ceramics were fabricated successfully after sintering at 1773 K for 6 hours in N_2 and N_2/5%H_2 indicating that reduced atmospheres were beneficial for the formation of RP_2 phase. Sintering undoped $Sr_3Ti_2O_7$ in N_2/5%H_2 at 1773 K to yield dark green coloured ceramics is an effective method to remove oxygen (δ) based on equation 5-1 and therefore increase the conductivity in the interior of the ceramics; however, this method also induces compositional changes on the ceramic surfaces. XRD on an unpolished ceramic surface revealed the presence of $Sr_3Ti_2O_7$, a $SrTiO_3$-type phase and several unindexed peaks that could not be assigned to any known Sr-Ti-O phase(s) in the ICDD system, Figure 5.4. A BEI of an unpolished ceramic from SEM revealed clear evidence of a surface layer (Figure 5.5), and EDS analysis showed the surface to have a Sr/Ti ~1 compared to the expected value of ~1.5 observed from the interior of the ceramic, Table 5.1. This change in phase assemblage and composition suggests some volatilisation of Sr (possibly as SrO) in addition to oxygen-loss occurs from the ceramic surfaces under these reducing conditions at 1773 K. The local pO_2 will be more reducing at the pellet surfaces compared to the pellet interiors and this introduces a pO_2 gradient within the ceramics. This limits the level of SrO volatilisation from the ceramic interiors but is sufficient to obtain a level of oxygen-loss (δ) to induce semiconductivity in the RP $Sr_3Ti_2O_7$ phase.

IS at room temperature on an unpolished ceramic sintered in N_2/5%H_2 showed the presence of an insulating surface layer with $R > 10$ MΩ, Figure 5.8(a), that could be removed on polishing to reveal a non-ohmic electrode contact with $R \sim 40$ kΩ, Figure 5.8(b), and a total ceramic resistivity of ~4 Ωcm, Figure 5.8(c). Based on a combination of the XRD, SEM/EDS and IS results, it is proposed that the insulating surface layer(s) on ceramics sintered under reducing conditions is associated with oxygen up-take and therefore oxidation of the reduced Sr-Ti-O phases at the ceramic surfaces (including SrTiO$_{3-\delta}$ and Sr$_3$Ti$_2$O$_{7-\delta}$) during the cooling procedure.

Structure, microstructure and electrical properties of La-doped Sr$_3$Ti$_2$O$_7$

XRD and TEM results show a very limited solid solution of La into Sr$_3$Ti$_2$O$_7$ for the e series prepared in air with a small volume expansion in the unit cell of x = 0.01 compared to undoped Sr$_3$Ti$_2$O$_7$ (x = 0.00), Figure 5.10(c). A larger solid solution with $x \leq 0.05$ appears to exist for samples processed under reducing conditions with an initial expansion of the unit volume for undoped Sr$_3$Ti$_2$O$_{7-\delta}$ (x = 0.00), followed by a systematic decrease with increasing x, Figure 5.10(d). There was no appreciable solid solution for any V_a and V_b samples prepared in air or N$_2$/5%H$_2$ at 1773 K.

These results show that creation of cation vacancies (A- or B-site) via La-doping, mechanisms 5-3 and 5-4 are not favoured in RP-phases in air or reducing atmospheres which is in contrast to perovskite SrTiO$_3$ where a substantial solid solution containing A-site vacancies is known to exist[25]. All ceramics processed in air were white/yellow in appearance suggesting that they were fully oxidised and IS showed all air sintered ceramics to be electrical insulators with low bulk conductivity and high E_a (> 1 eV), confirming electronic compensation, mechanism 5-2, does not exist for La-doping of ceramics sintered in air, Figure 5.13. The lower bulk σ and higher E_a of x = 0.01 samples compared to undoped Sr$_3$Ti$_2$O$_7$ ceramics confirms that limited La-doping of the Sr$_3$Ti$_2$O$_7$ lattice does occur and that a change in conduction mechanism must also occur given the substantial increase in E_a for x = 0.01, Figure 5.13. La^{3+} is a smaller ion than Sr^{2+} so the observed increase in unit cell volume for x = 0.01 is attributed to the interstitial mechanism 5-5 that can occur in RP-type phases. The excess oxygen from the La$_2$O$_3$ may be associated with the interfaces between the RS layers and perovskite blocks in the RP structure in the form of disordered defects and/or fill up any residual oxygen vacancies in the lattice due to acceptor impurities associated with the TiO$_2$ reagent[26]. The TEM image in Figure 5.12(a) for x = 0.01 processed in air supports the idea of increased strain associated with the interstitial doping mechanism whereas the Arrhenius plot of bulk conductivity in Figure 5.13 supports the idea that the change in conduction mechanism may be associated with a suppression of extrinsic (acceptor-type) conduction in undoped $Sr_3Ti_2O_7$ with an E_a ~1.2 eV leading intrinsic conduction with $E_a > 2$ eV due to the filling up of extrinsic oxygen vacancies by the interstitial oxide ions. Unfortunately, the solid solution limit is low and it is not possible to unambiguously prove either (or both) of these possibilities.

Lattice parameters and cell volume obtained from XRD data of crushed powders from polished ceramics of the electronic series (including x = 0.00) sintered in N_2/5%H_2, Figures 5.10(d) and (c), reveal some interesting trends, especially when combined with the electrical conductivity results, Figure 5.15(b).

First, there is considerable expansion of the cell volume and a substantial increase in σ when processing ceramics under reducing conditions compared to those processed in air, as observed for both undoped (x = 0.00) and doped compositions (x = 0.01), Figure 5.10(c). In the case of x = 0.00 this can be attributed solely to oxygen-loss with partial reduction of Ti^{4+} to Ti^{3+} ions based on equation 5-1. The ionic radius of Ti^{3+} is 0.67 Å compared to 0.605 Å for Ti^{4+} (for octahedral co-ordination) and this leads to lattice expansion. The creation of oxygen vacancies can also result in lattice expansion due to a reduction in the Coulombic forces between the cations and anions in perovskites[27]. The green colour and significant σ (~1 S/cm at 1000 K) for reduced x = 0.00 ceramics is consistent with the creation of mixed Ti^{3+}/Ti^{4+} ions in the lattice whereas ceramics processed in air are fully oxidized and insulating with only Ti^{4+} ions in the lattice. In the case of x = 0.01, the larger unit cell volume of reduced ceramics compared to those processed in air can primarily be attributed to the creation of mixed Ti^{3+}, Ti^{4+} content and this is consistent with an increase in σ.

Second, despite reduced ceramics containing larger Ti^{3+} ions, cell volume decreases smoothly with increasing La-content for reduced La-doped samples, Figure 5.10(c). There is no systematic trend in σ with La-content;

however, σ and therefore Ti^{3+} content (based on the assumption that σ is dominated by carrier concentration as opposed to any changes in carrier mobility) is generally higher than that of reduced $x = 0.00$ and all are ~1 order of magnitude higher at 973 K, Figure 5.15(b). This decrease in cell volume on La-doping is in contrast to the increase in cell volume observed for the La-doped e series processed in air, Figure 5.10(c) and indicates the processing pO_2 influences the doping mechanism(s).

The increase in cell volume for $x = 0.01$ processed in air despite the smaller ionic radius of La^{3+} compared to Sr^{2+} was attributed to the interstitial doping mechanism (equation 5-5) with incorporation of excess oxygen. Under reducing conditions, the most likely scenario is that donor doping (mechanism 5-2) occurs as any interstitial oxygen ions are presumably more prone to removal under reduction compared with conventional lattice oxygen ions associated with the RP structure. Therefore, despite the production of larger Ti^{3+} ions (equation 5-2) and the possibility of creating oxygen vacancies under reducing conditions (equation 5-1), unit cell volume contraction occurs due to the partial replacement of larger Sr^{2+} with smaller La^{3+} ions on the cation sublattice. It has previously been shown[12] that RE-dopants prefer the cation site associated with the RS layer compared to the perovskite blocks in $Sr_3Ti_2O_7$ due to the lower co-ordination number of this site and the smaller ionic radius of RE-ions compared to Sr.

The electronic donor-doping compensation mechanism (equation 5-2) is well known to occur in $SrTiO_3$ at low pO_2[14,15]. With increasing La doping level, the formation of local defect clusters in the matrix (maybe La^{3+}-O-Ti^{3+}) was observed by TEM along the [001] direction of the tetragonal cell, restricting grain growth and the average grain size as shown by SEM, Figure 5.11. The TEM images also provide evidence about differences between series x samples sintered in air and $N_2/5\%H_2$. From this data, it is proposed that a reducing atmosphere not only encourages electronic compensation for La^{3+} but may also be beneficial in releasing strain between the layers, thereby facilitating substitution into the Sr-sites of the RP $Sr_3Ti_2O_{7-\delta}$ phase and therefore extending the limit of the solid solution.

For x = 0.10, a simple perovskite-type ‘SrTiO$_{3-\delta}$’ precipitates as an observable secondary phase, Figure 5.10(b). The stoichiometry of the ST perovskite phase is unknown but is likely to be oxygen-deficient due to the reducing conditions and possibly contains La on the A-site and may therefore also be A-site deficient. As discussed later, it is proposed that this ST perovskite-phase is more electrically conductive than the La-doped RP Sr$_3$Ti$_2$O$_{7-\delta}$ phase.

Thermoelectric properties of La-doped Sr$_3$Ti$_2$O$_7$

All ceramics show negative S values, confirming n-type conduction consistent with mixed Ti^{3+}, Ti^{4+} ions in the samples prepared under reducing conditions. Considering a temperature of 973 K to compare the thermoelectric properties, S drops by a factor of ~2-3 in series x up the solid solution limit of ~0.05 but the high temperature σ (at 973 K) has increased by ~1 order of magnitude (for all x) compared to x = 0.00. This shows that the La doping mechanism has increased the carrier concentration, as all samples have been treated under the same reducing conditions so any conductivity due to oxygen-loss should be similar in all samples, irrespective of x. If the doping mechanism is electronic compensation (equation 5-2), σ should increase systematically with x. However, x = 0.01, 0.02 and 0.05 all have similar σ at 973 K. In addition, x = 0.01 shows metallic temperature-dependent behaviour whereas 0.02 and 0.05 show semiconducting temperature-dependent behaviour, Figure 5.15(b), so the conduction mechanisms are different. The switch from metallic to semiconducting behaviour with increasing x may be related to extended defects/clusters/strain trapping of the conduction electrons. For the single-phase samples in series x, the PF (at 973 K) has a dome shape with a maximum of ~40 μW m^{-1} K^{-2} (for x ~0.02) that reflects the balance between a decrease in S with an increase in σ with increasing x, Figure 5.16. This behaviour is consistent with the general observation that an increase in carrier concentration leads to a lower Seebeck coefficient[27].

It is interesting to consider the thermoelectric properties of x = 0.10 ceramics in series x as they contain secondary phases, including a cubic $SrTiO_{3-\delta}$ (ST)-type phase, Figure 5.10(b). This has a dramatic effect on the thermoelectric properties. The electrical conductivity is now a factor of ~50 higher than x = 0.00 and 5 times higher than x ~0.01 - 0.05 so clearly this secondary ST-type phase must be much more conductive than the RP phase. S drops for x = 0.10 ceramics as would be expected for its higher σ but this multi-phase ceramic has the highest PF for series x with a value of ~60 μW m^{-1} K^{-2}, Figure 5.16. Series y and z are also multi-phase ceramics that contain a highly conducting ST-type phase. Generally, PF values are higher in the y series compared to those in the x series. At 973 K, z = 0.10 with ST-type phase has the highest PF of this series with a value comparable to that of x = 0.10. These results suggest that the cubic ST-type perovskite phase(s) have higher σ than any La-doped RP phase and are therefore more suitable for thermoelectric applications than RP phases. It also suggests that care should be taken when reporting high PF or ZT values for Rare-earth doped RP-phases where phase purity has been confirmed only by Laboratory XRD as the thermoelectric properties can be significantly influenced by low levels of perovskite-type phases that are difficult to detect via such characterisation.

La-doped $Ca_3Ti_2O_7$

Single-phase $Ca_3Ti_2O_7$ can be fabricated successfully under reducing conditions. However, $Ca_4Ti_3O_{10}$ phases were detected in La-doped $Ca_3Ti_2O_7$ samples. The electrical conductivity increases with increasing La-doping level when sintered in N_2/5%H_2 indicating the role of La as an electron donor in $Ca_3Ti_2O_7$ ceramics. The semiconducting behavior of La-doped $Ca_3Ti_2O_7$ may be as a result of the insulating CaO layer blocking electron movement at low temperature.

Conclusion

To conclude, the electrical conductivity of $Sr_3Ti_2O_7$ and $Ca_3Ti_2O_7$ Ruddlesden-Popper phase is still too low even after La-doping for the development of good thermoelectric properties. It is proposed that the insulating SrO and CaO rock-salt layers in Ruddlesden-Popper type layered materials create an electrical barrier for electron mobility and therefore limit electrical conductivity[28]. However, reducing conditions are conducive towards electronic doping of La in (Sr, Ca)$_3$Ti$_2$O$_{7-\delta}$ ceramics. The heterogeneity of La-doped $Sr_3Ti_2O_7$ ceramics prepared under reducing conditions has a significant impact on the measured thermoelectric properties. Compared to $SrTiO_3$, σ of La-doped RP $Sr_3Ti_2O_{7-\delta}$ prepared under reducing conditions where both oxygen loss (equation 5-1) and electronic 'donor'-doping of La on the Sr-sites (equation 5-2) occurs remain too low for the development of good thermoelectric properties at elevated temperatures, e.g. 973 K.

Reference

1 S. Ohta, T. Nomura, H. Ohta, M. Hirano, H. Hosono and K. Koumoto, Applied Physics Letters 87, 092108 (2005).
2 J. Yang and F. R. Stabler, Journal of Electronic Materials 38, 1245 (2009).
3 Q. Li, Z. Lin and J. Zhou, Journal of Electronic Materials 38, 1268 (2009).
4 E. S. Toberer, A. F. May and G. J. Snyder, Chemistry of Materials 22, 624 (2010).
5 M. G. Kanatzidis, Chemistry of Materials 22, 648 (2010).
6 K. Salzgeber, P. Prenninger, A. Grytsiv, P. Rogl and E. Bauer, Journal of Electronic Materials 39, 2074 (2010).
7 R. D. Shannon, Acta Crystallographica Section A: Foundations and Advances 32, 751 (1976).
8 J. Liu, C. L. Wang, W. B. Su, H. C. Wang, P. Zheng, J. C. Li, J. L. Zhang and L. M. Mei, Applied Physics Letters 95, 162110 (2009).
9 J. Ravichandran, W. Siemons, D.-W. Oh, J. T. Kardel, A. Chari, H. Heijmerikx, M. L. Scullin, A. Majumdar, R. Ramesh and D. G. Cahill, Physical Review B 82 165126-1 (2010).
10 A. Kikuchi, N. Okinaka and T. Akiyama, Scripta Materialia 63, 407 (2010).
11 Y. Wang, K. H. Lee, H. Hyuga, H. Kita, H. Ohta and K. Koumoto, Journal of Electroceramics 24, 76 (2008).
12 Y. F. Wang, K. H. Lee, H. Ohta and K. Koumoto, Ceramics International 34, 849 (2008).
13 N. G. Eror and U. Balachandran, Journal of Solid State Chemistry 40, 85 (1981).
14 U. Balachandran and N. G. Eror, Journal of The Electrochemical Society 129, 1021 (1982).

15 B. F. Flandermeyer, A. K. Agarwal, H. U. Anderson and M. M. Nasrallah, Journal of Materials Science 19, 2593 (1984).
16 C.-D. Savaniu and J. T. S. Irvine, Journal of Materials Chemistry 19, 8119 (2009).
17 C.-D. Savaniu, D. N. Miller, J. T. S. Irvine and M. Menon, Journal of the American Ceramic Society 96, 1718 (2013).
18 I. Akin, M. Li, Z. Lu and D. C. Sinclair, RSC Advances 4, 32549 (2014).
19 S. N. Ruddlesden and P. Popper, Acta Crystallographica 11, 54 (1958).
20 M. M. Elcombe, E. H. Kisi, K. D. Hawkins, T. J. White, P. Goodman and S. Matheson, Acta Crystallographica Section B: Structural Science 47, 305 (1991).
21 CaRIne Crystallography 3.1. Computer Program, DIVERGENT S. A. Centre de Transfert 60200, France.
22 K. R. Udayakumar and Alastair N. Cormack, Journal of the American Ceramic Society 71, C469 (1988).
23 D. C. Sinclair and A. R. West, Journal of Materials Science Letters 7, 823 (1988).
24 D. C. Sinclair and A. R. West, Journal of Applied Physics 66, 3850 (1989).
25 A. D. Aljaberi and J. T. S. Irvine, Journal of Materials Chemistry A 1, 5868 (2013).
26 N.-H. Chan, R. K. Sharma and D. M. Smyth, Journal of the American Ceramic Society 65, 167 (1982).
27 M. Cutler, J. Leavy and R. Fitzpatrick, Physical Review 133, A1143 (1964).
28 N. Sirikanda, H. Matsumoto and T. Ishihara, Solid State Ionics 181, 315 (2010).

Chapter 6: La-doped $SrTiO_3$ System

6.1 Introduction

As discussed in Chapter 5, the $SrTiO_3$ second phase appeared electrically more conductive than the La-doped $Sr_3Ti_2O_{7-\delta}$ matrix. Overall, the electrical conductivity of the Ruddlesden-Popper (RP) phase, $SrO(SrTiO_3)_2$ was still too low even after La-doping due to the formation of electrical barriers resulting from insulating SrO rocksalt layers in the Ruddlesden-Popper structure. Thus, the ZT value of the RP phase was smaller than that of $SrTiO_3$. Therefore, La-doped $SrTiO_3$ is the subject of Chapter 6 with similar dopant strategies to those adopted in Chapter 5.

It is known that incorporation of La^{3+} ions in $SrTiO_3$ can lead to Sr-site vacancies due to the low electrostatic potential of the Sr-site[1] or an intergrowth of $SrTiO_3$ and $La_2Ti_2O_7$ in oxidising conditions[2] or creates electrons from partial reduction of Ti in reducing conditions[3]. Furthermore, Sr-site deficiency leads to higher electrical conductivity in $Sr_{1-3y/2}La_yTiO_3$ compared to stoichiometric compounds ($Sr_{1-x}La_xTiO_3$) prepared at the same oxygen partial pressure[4]. The introduction of A-site and oxygen deficiency in the starting compositions has been conceived as a worthy scenario for higher ZT values. In this chapter, there is an attempt to improve the thermoelectric properties of La-doped $SrTiO_3$ by engineering oxygen vacancy and A-site or B-site deficiency to decrease the thermal conductivity without destroying the electrical conductivity.

This chapter utilises the dopant strategies for $SrTiO_3$ described in equations 6-1 to 6-3 but eventually focuses on $Sr_{1-3y/2}La_yTiO_3$ ceramics with A-site deficiency (equation 6-2):

x series: $La_2O_3 + 2TiO_2 \Rightarrow 2La_{Sr}^{\cdot} + 2e' + 2Ti_{Ti}^{x} + 6O_O^{x} + 1/2O_2(g)$ 6-1

y series: $La_2O_3 + 3TiO_2 \Rightarrow 2La_{Sr}^{\cdot} + V_{Sr}'' + 3Ti_{Ti}^{x} + 9O_O^{x}$ 6-2

z series: $2La_2O_3 + 3TiO_2 \Rightarrow 4La_{Sr}^{\cdot} + V_{Ti}'''' + 3Ti_{Ti}^{x} + 12O_O^{x}$ 6-3

As in chapter 5, these mechanisms will be denoted as x series/e, y series/V_a and z series/V_b, respectively.

6.2 Undoped $SrTiO_3$

6.2.1 Structure and Microstructure

All $SrTiO_3$ ceramics were sintered at 1773 K for 6 hours. Figure 6.1 shows the XRD traces of a polished $SrTiO_3$ pellet and its surface sintered in $N_2/5\%H_2$. All peaks could be indexed according to cubic perovskite $SrTiO_3$ ([35-734] ICDD card) for the polished pellet. However, second phases including TiO were detected on the unpolished surface.

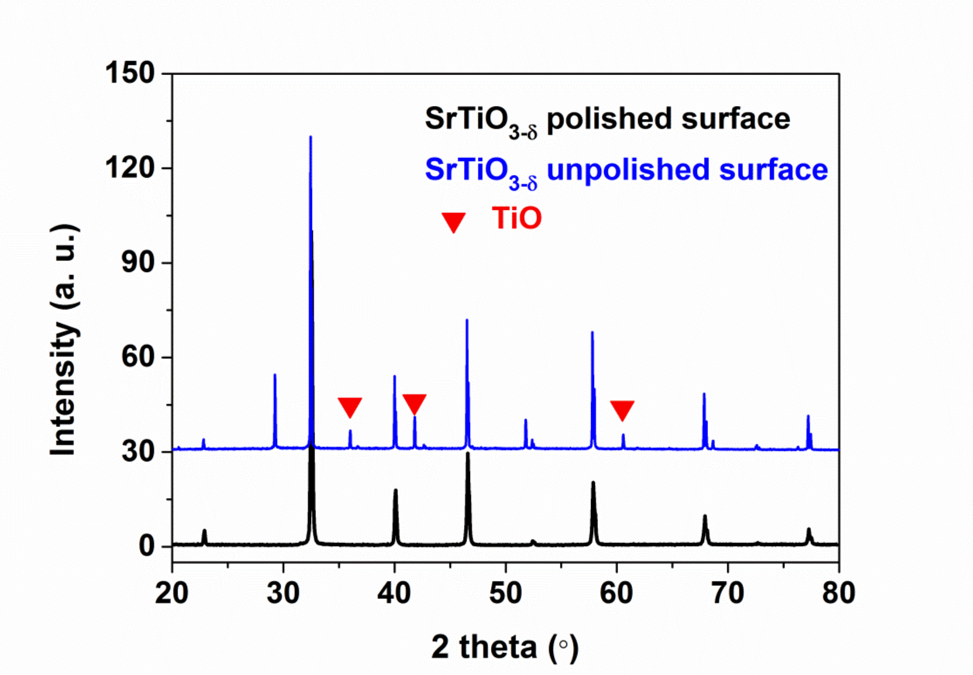

Figure 6.1 XRD patterns of a polished $SrTiO_3$ pellet (lower) and its surface (upper) prior to polishing after being sintered in $N_2/5\%H_2$ at 1773 K for 6 hrs.

Secondary electron images of the fracture surface of a $SrTiO_3$ pellet sintered in $N_2/5\%H_2$ at 1773 K along with backscattered images are shown in Figure 6.2. The interior was homogeneous, as shown in Figure 6.2(b). A thin surface layer with a similar composition but smaller grain size to that of the ceramic interior appeared, Figure 6.2(c) and (d).

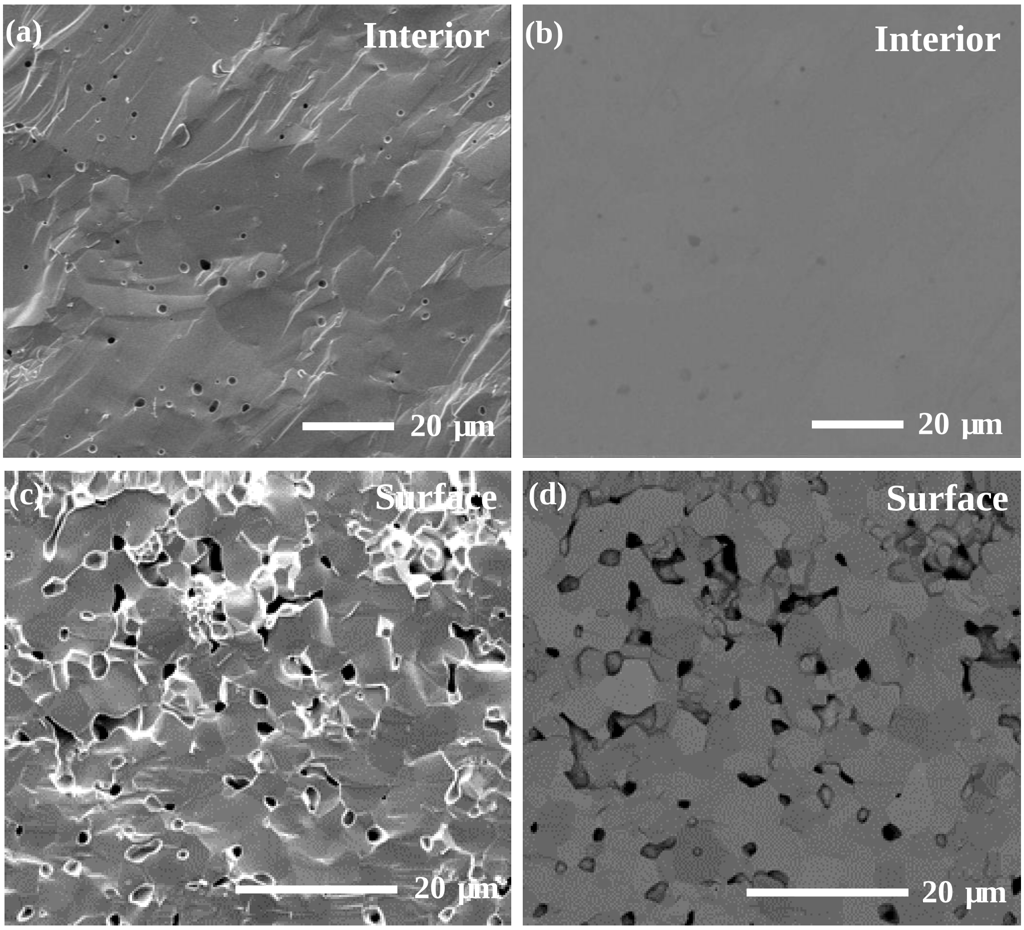

Figure 6.2 Secondary electron and backscattered images of the fracture surface of a $SrTiO_3$ pellet sintered in $N_2/5\%H_2$ at 1773 K for 6 hrs.

6.2.2 Electrical Properties

Typical room temperature Y′ and combined -Z″, M″ spectra of an unpolished $SrTiO_3$ and polished pellet sintered in $N_2/5\%H_2$ at 1773 K are shown in Figure 6.3(a) and (b). The unpolished and polished pellet all showed non-ohmic contacts due to their high electrical conductivity. However, the electrical conductivity of the polished $SrTiO_3$ pellet was higher than the unpolished one, Figure 6.3(a).

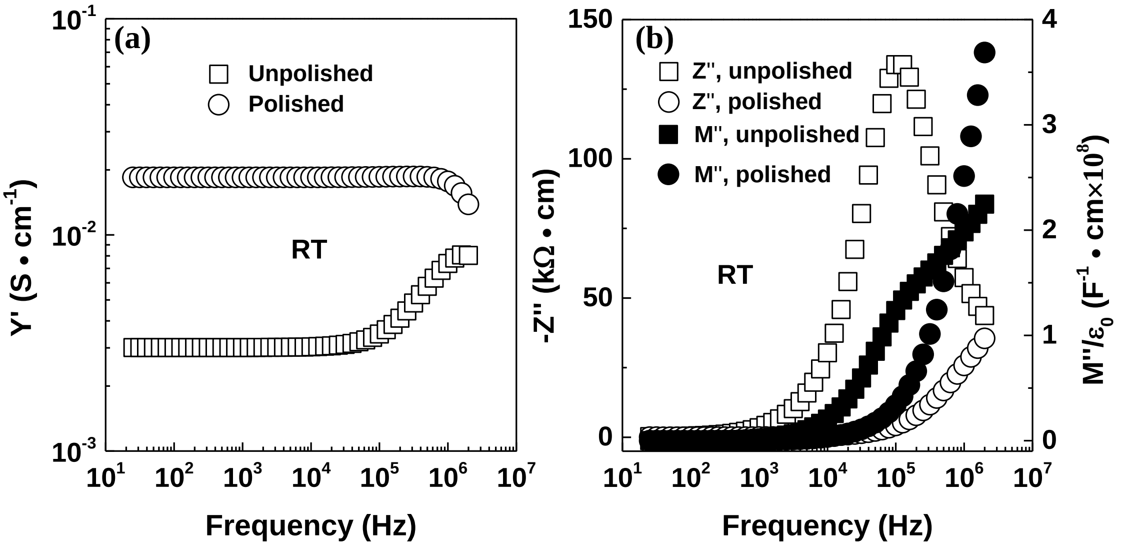

Figure 6.3 Typical Y′ (a) and combined -Z″, M″ spectra (b) at room temperature of an unpolished and polished $SrTiO_3$ pellet sintered in N_2/5%H_2 at 1773 K for 6 hrs.

6.3 La-doped $SrTiO_3$

6.3.1 Structure and Microstructure

Figure 6.4 shows the XRD traces of crushed $Sr_{1-x}La_xTiO_3$, $Sr_{1-3y/2}La_yTiO_3$ and $Sr_{1-z}La_zTi_{1-z/4}O_3$ ceramics sintered in air and N_2/5%H_2 at 1773 K for 6 hours. The solid solubility limit for the electronic compensation series sintered in air ($x \leq 0.30$) was smaller than those of ceramics sintered in N_2/5%H_2 ($x \leq 0.60$), Figure 6.4(a) and (b). The secondary phase peaks of air and N_2/5%H_2 sintered ceramics that contained $SrLa_4Ti_5O_{17}$ (n = 5) and $Sr_2La_4Ti_6O_{20}$ (n = 6) phases with derivative layer perovskite structures matched to data reported by Irvine *et al.*[2]. The V_a series sintered in air were single phase up to y = 0.63 with primitive cubic cells at $y \leq 0.40$ and orthorhombic structures from 0.50 to 0.63 but y = 2/3 contained $La_2Ti_2O_7$ second phase, Figure 6.4(c). The N_2/5%H_2 sintered ceramics were cubic-type perovskite cells up to y = 0.20, and contained an extra peak labelled with an asterisk from y = 0.30 to the end member, Figure 6.4(d). For the V_b series, the structures were cubic at $z \leq 0.20$, then cubic-hexagonal mixture phases, and finally became hexagonal $Sr_2La_4Ti_5O_{18}$ at z = 0.70. The $SrLa_4Ti_4O_{15}$ phase was observed at z = 0.80 for air sintered samples, Figure 6.4(e). However, for $N_2/5\%H_2$ sintered compositions, the structures were cubic at $z \leq 0.15$, then contained La_2O_3 secondary phase at $0.20 \leq z \leq 0.40$ and became a cubic-hexagonal mixture of phases up to z = 0.80, Figure 6.4(f).

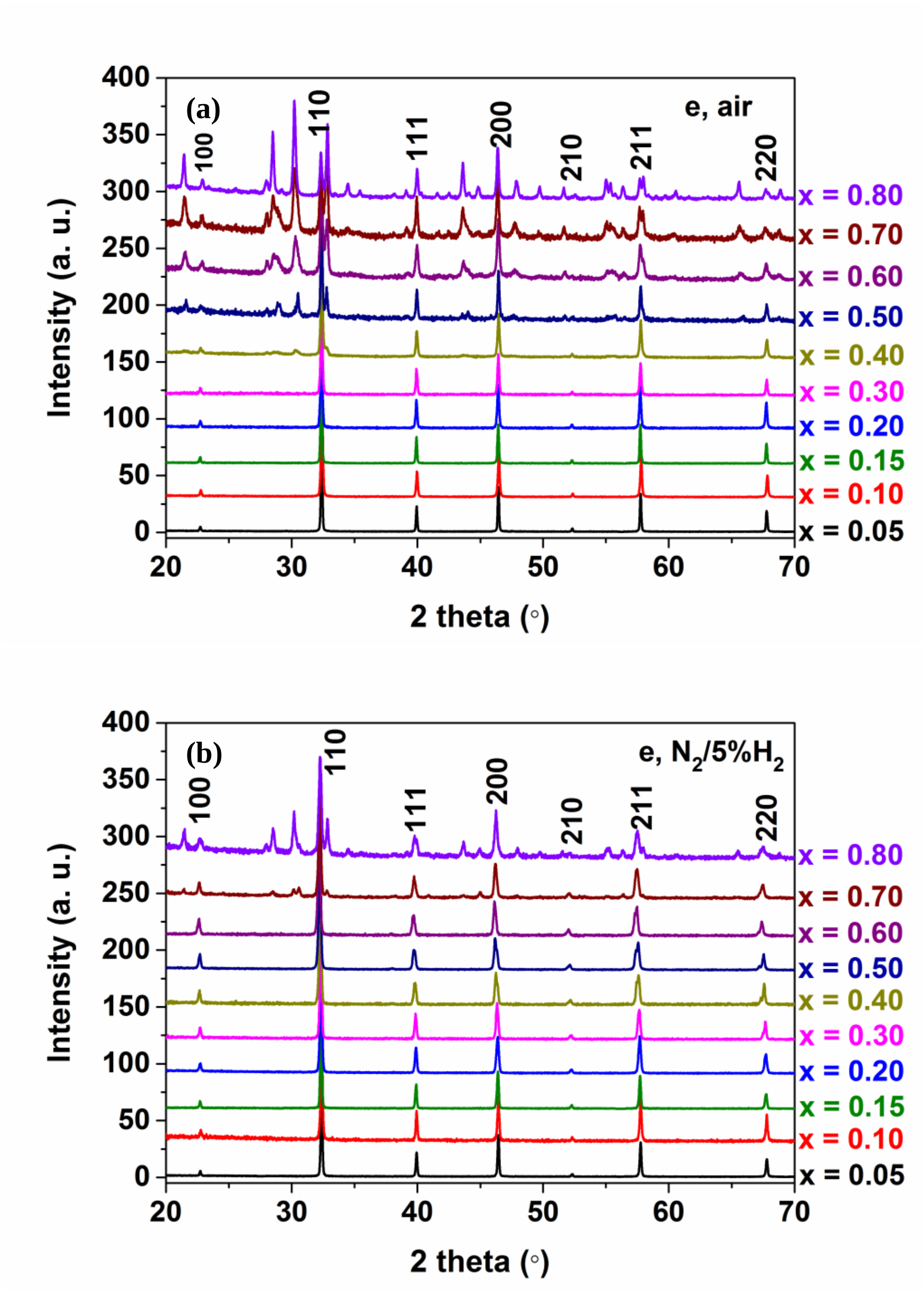

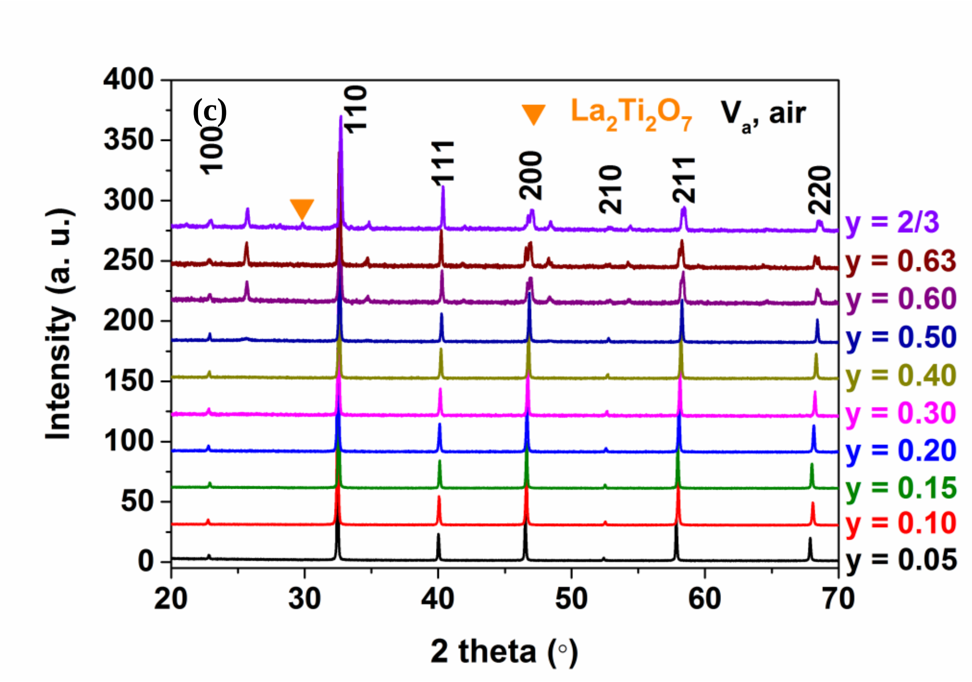
(c)
▼ La2Ti2O7
Va, air
100
110
111
200
210
211
220
Intensity (a. u.)
400
350
300
250
200
150
100
50
0
2 theta (◦)
20
30
40
50
60
70
y = 2/3
y = 0.63
y = 0.60
y = 0.50
y = 0.40
y = 0.30
y = 0.20
y = 0.15
y = 0.10
y = 0.05

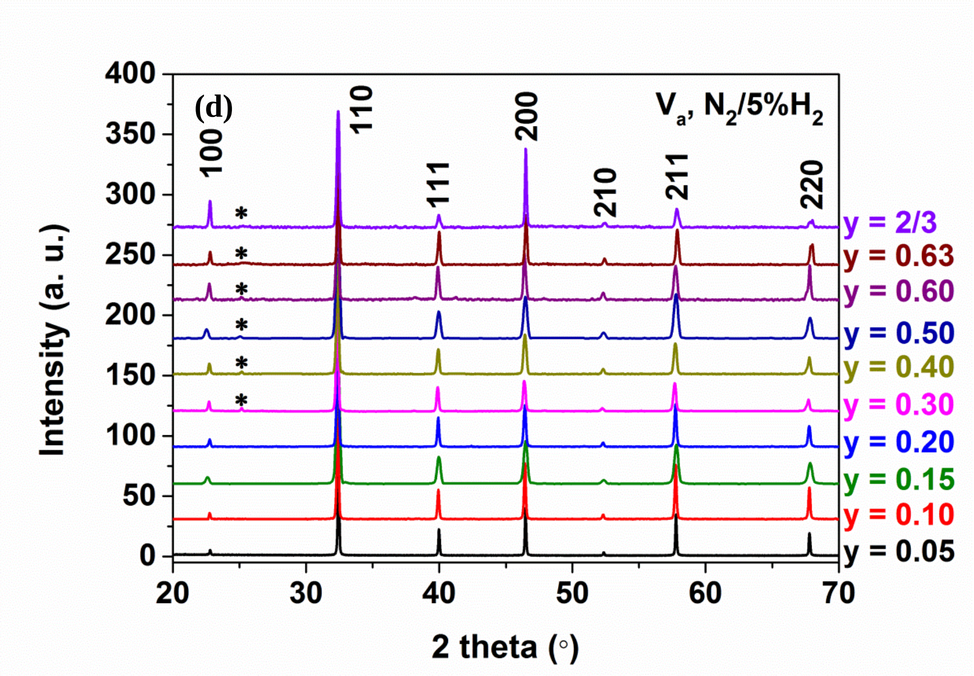
(d)
Va, N2/5%H2
100
110
111
200
210
211
220
*
Intensity (a. u.)
400
350
300
250
200
150
100
50
0
2 theta (◦)
20
30
40
50
60
70
y = 2/3
y = 0.63
y = 0.60
y = 0.50
y = 0.40
y = 0.30
y = 0.20
y = 0.15
y = 0.10
y = 0.05

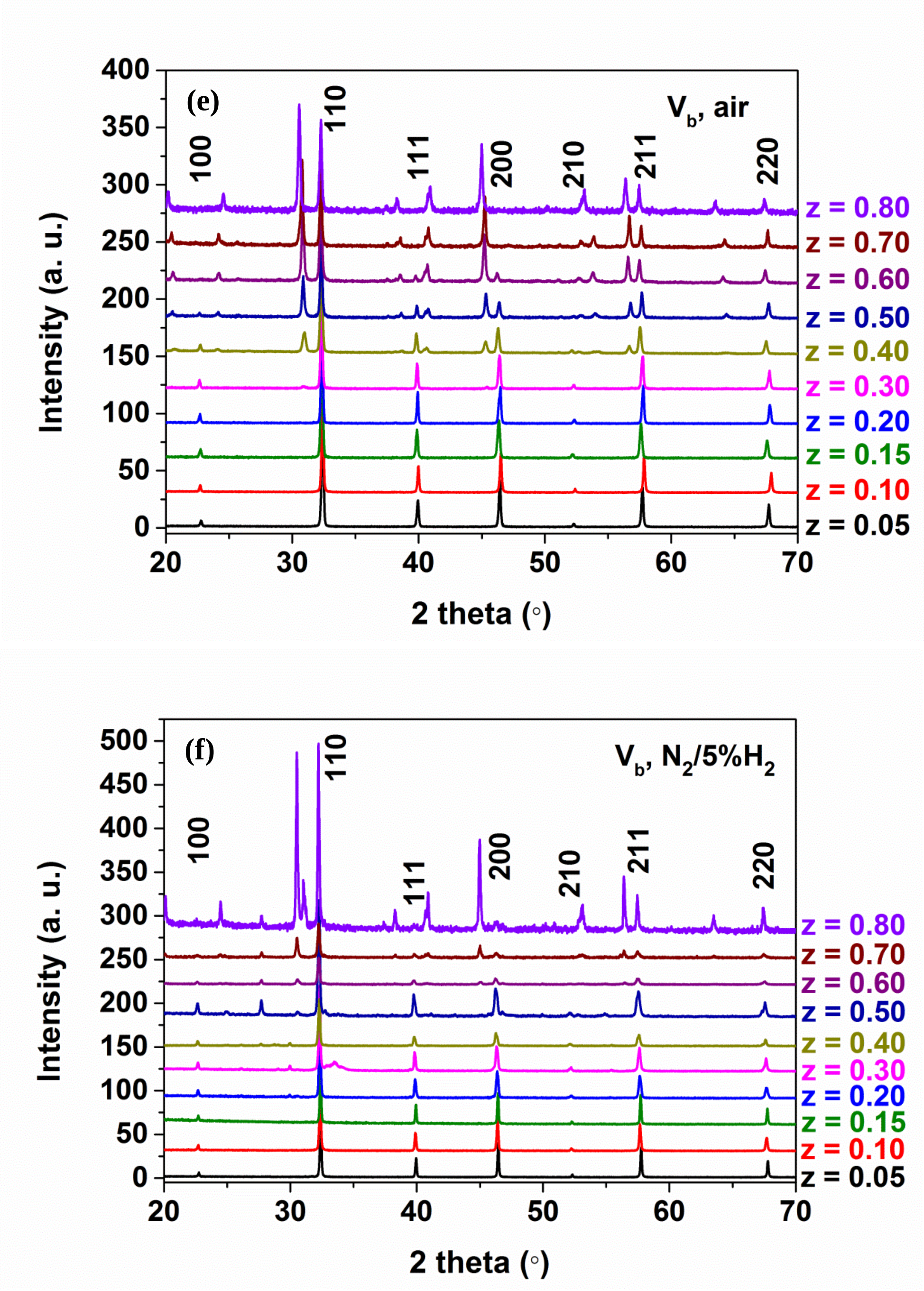

Figure 6.4 XRD traces of crushed pellets for $Sr_{1-x}La_xTiO_3$, $Sr_{1-3y/2}La_yTiO_3$ and $Sr_{1-z}La_zTi_{1-z/4}O_3$ sintered in air and N_2/5%H_2 at 1773 K for 6 hrs.

As can be seen from Figure 6.5, for the electronic series, a metrically cubic structure was retained for x = 0.30 in air. Samples sintered in N_2/5%H_2 had a cubic to tetragonal transition at x ≈ 0.30. Overall, a metrically cubic structure was easier to retain in the air sintered V_a series in comparison to other defect dopant strategies. The unit cell volume parameter decreased and then increased as y increased uniformly, indicative of a cubic to orthorhombic transition, as shown in Figure 6.5. However, the unit cell volume parameter for the $N_2/5\%H_2$ sintered samples increased up to y = 0.20 and then decreased with increasing y, suggesting that a phase transition point was around y = 0.20 ~ 0.30 that was consistent with the extra peak observed at $y \geq 0.30$, as seen from Figure 6.4(d). For the V_b series, solid solubility was small both in air and $N_2/5\%H_2$.

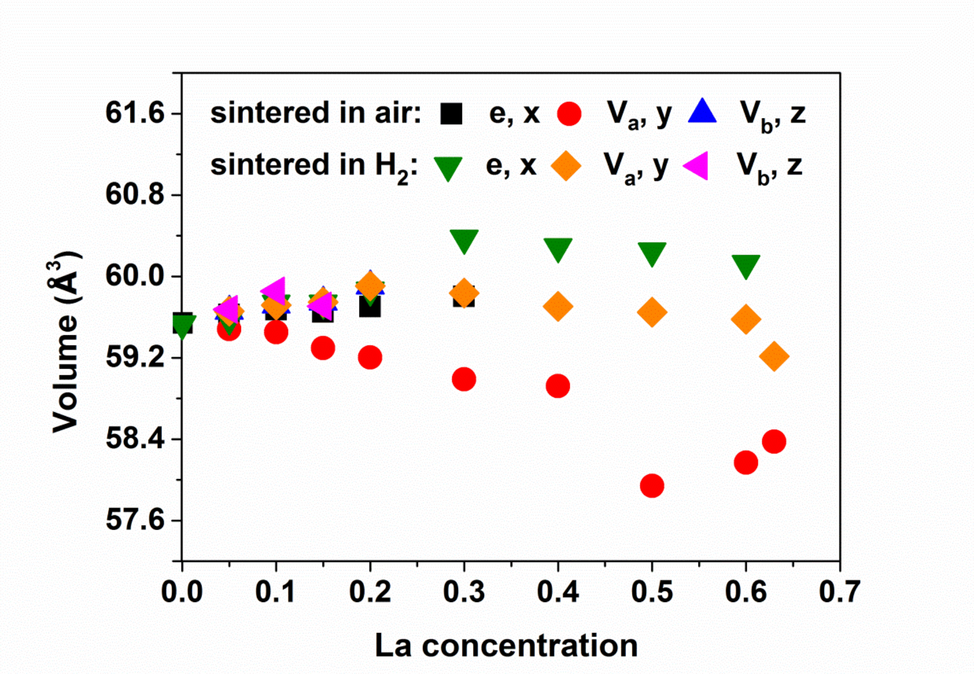

Figure 6.5 Dependence of unit cell volume on La concentration for $Sr_{1-x}La_xTiO_3$, $Sr_{1-3y/2}La_yTiO_3$ and $Sr_{1-z}La_zTi_{1-z/4}O_3$ sintered in air and $N_2/5\%H_2$ at 1773 K for 6 hrs.

The grain size of stoichiometric La-doped $SrTiO_3$ ceramics sintered in $N_2/5\%H_2$ at 1773 K for 6 hours reduced from ~5 μm to ~1 μm with increasing x. Strip- or plate-like grains were obtained at high La concentrations, x = 0.80.

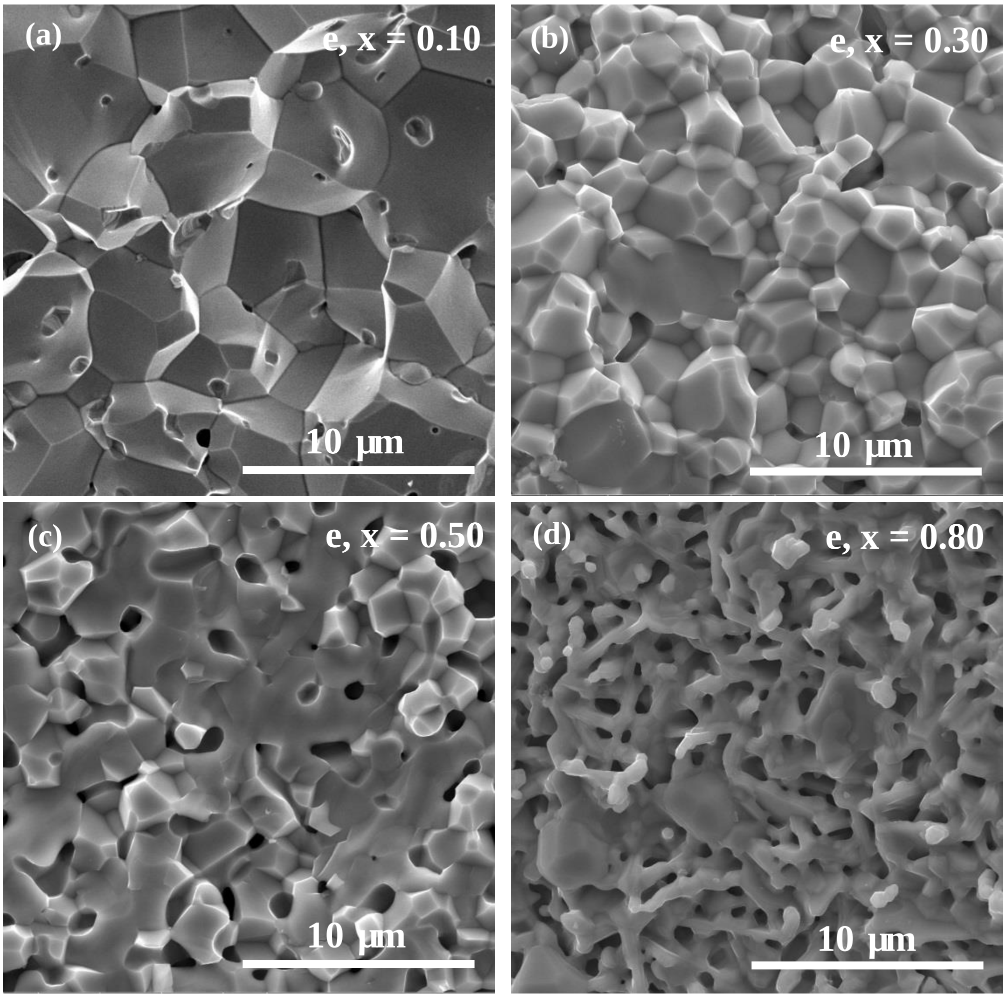

Figure 6.6 Secondary electron images of the surfaces of $Sr_{1-x}La_xTiO_3$ ceramics sintered in N_2/5%H_2 at 1773 K for 6 hrs: (a) 0.10, (b) 0.30, (c) 0.50, (d) 0.80.

As shown in Figure 6.7, V_a series samples sintered in N_2/5%H_2 had small grain sizes (~5 μm) at y = 0.10. With increasing y, grain sizes increased to ~20 μm until $y \geq 0.30$ and finally rod-like grains were obtained at $La_{2/3}TiO_3$.

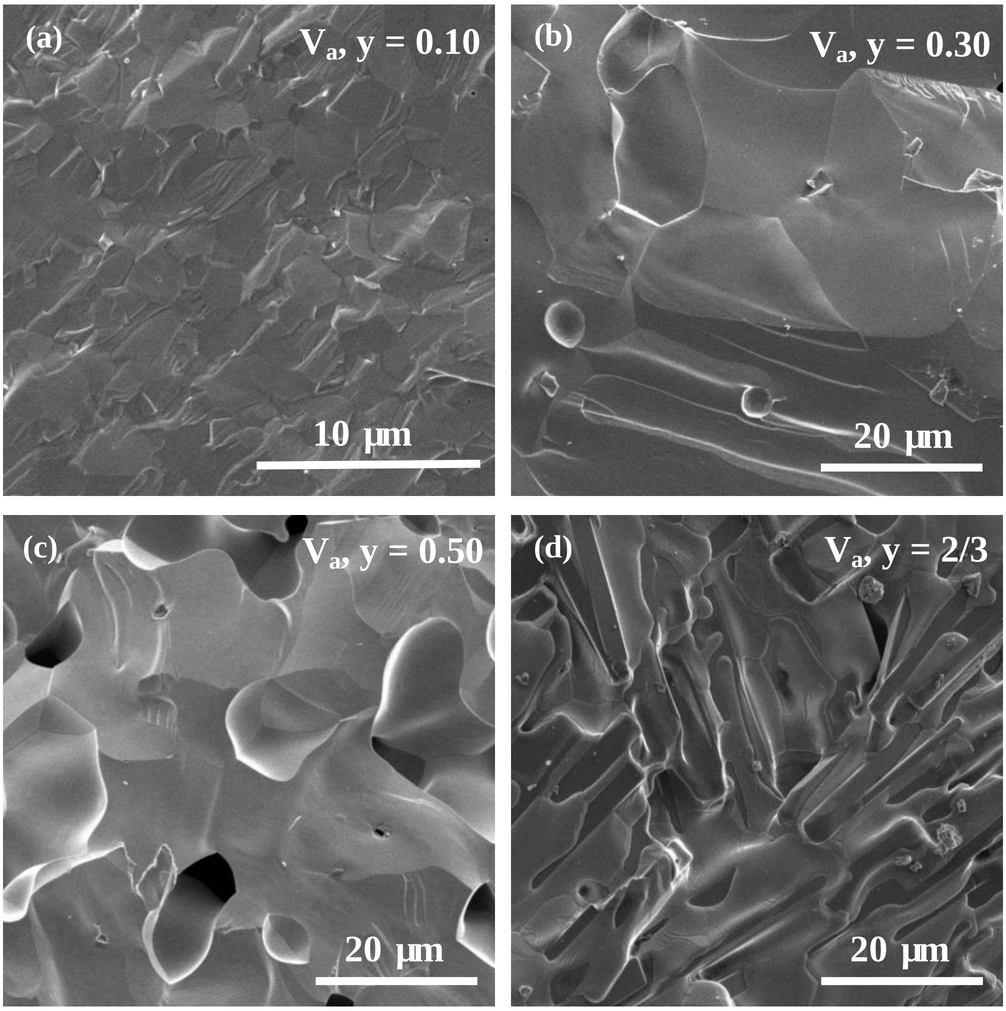

Figure 6.7 Secondary electron images of the surfaces of $Sr_{1-3y/2}La_yTiO_3$ ceramics sintered in N_2/5%H_2 at 1773 K for 6 hrs: (a) 0.10, (b) 0.30, (c) 0.50, (d) 2/3.

For the V_b series, the grain size of z = 0.10 was ~500 nm and then increased significantly to ~5 µm for z = 0.30, then decreased to ~2 µm. Rod-like grains were also obtained at z = 0.80, Figure 6.8.

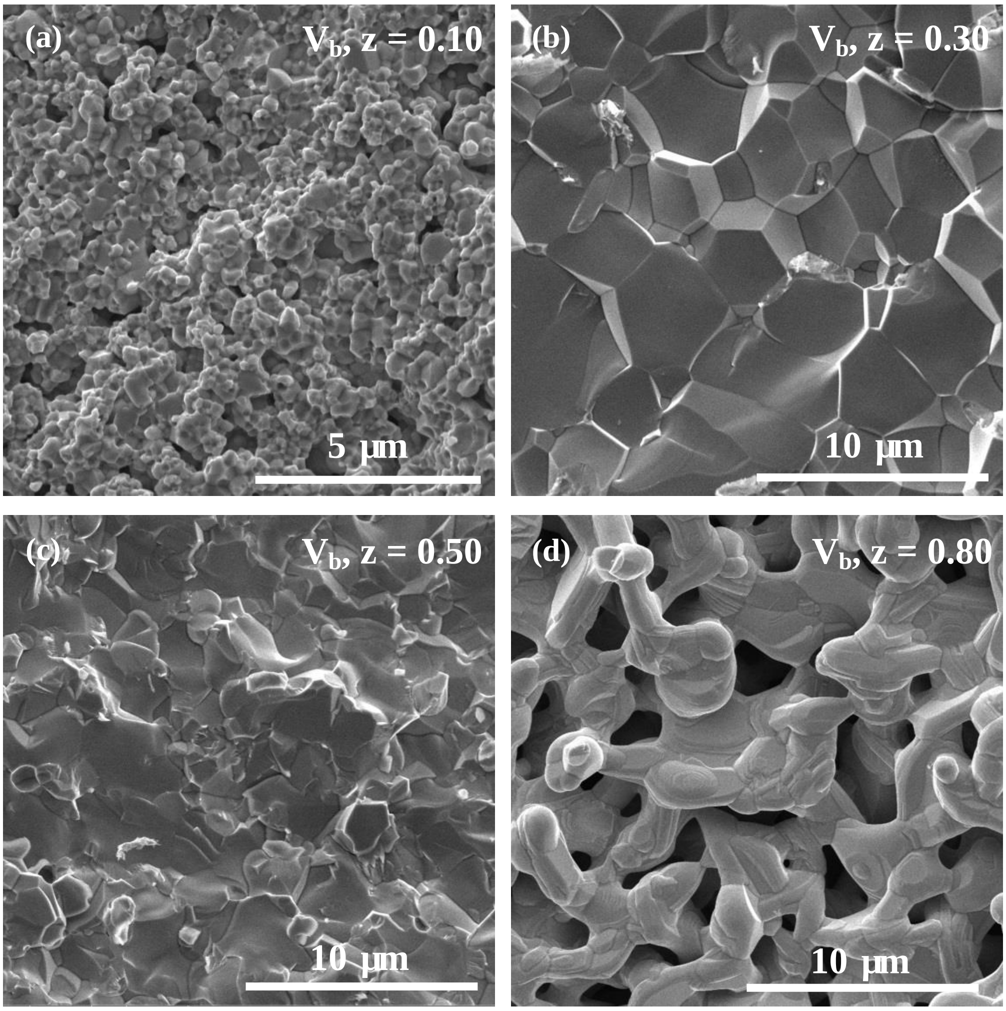

Figure 6.8 Secondary electron images of the surfaces of $Sr_{1-z}La_zTi_{1-z/4}O_3$ ceramics sintered in N_2/5%H_2 at 1773 K for 6 hrs: (a) 0.10, (b) 0.30, (c) 0.50, (d) 0.80.

Thermogravimetric analysis (TGA)

As shown in Figure 6.9(a), for the electronic series sintered in N_2/5%H_2 at 1773 K, oxygen uptake increased with increasing La concentration up to x = 0.60 except x = 0.10 and then decreased with increasing x for x = 0.70 and 0.80 samples. The colour of samples after TGA remained black for x = 0.10 but was white for all other samples. A complex phase assemblage was obtained after TGA, as shown in Table 6.1.

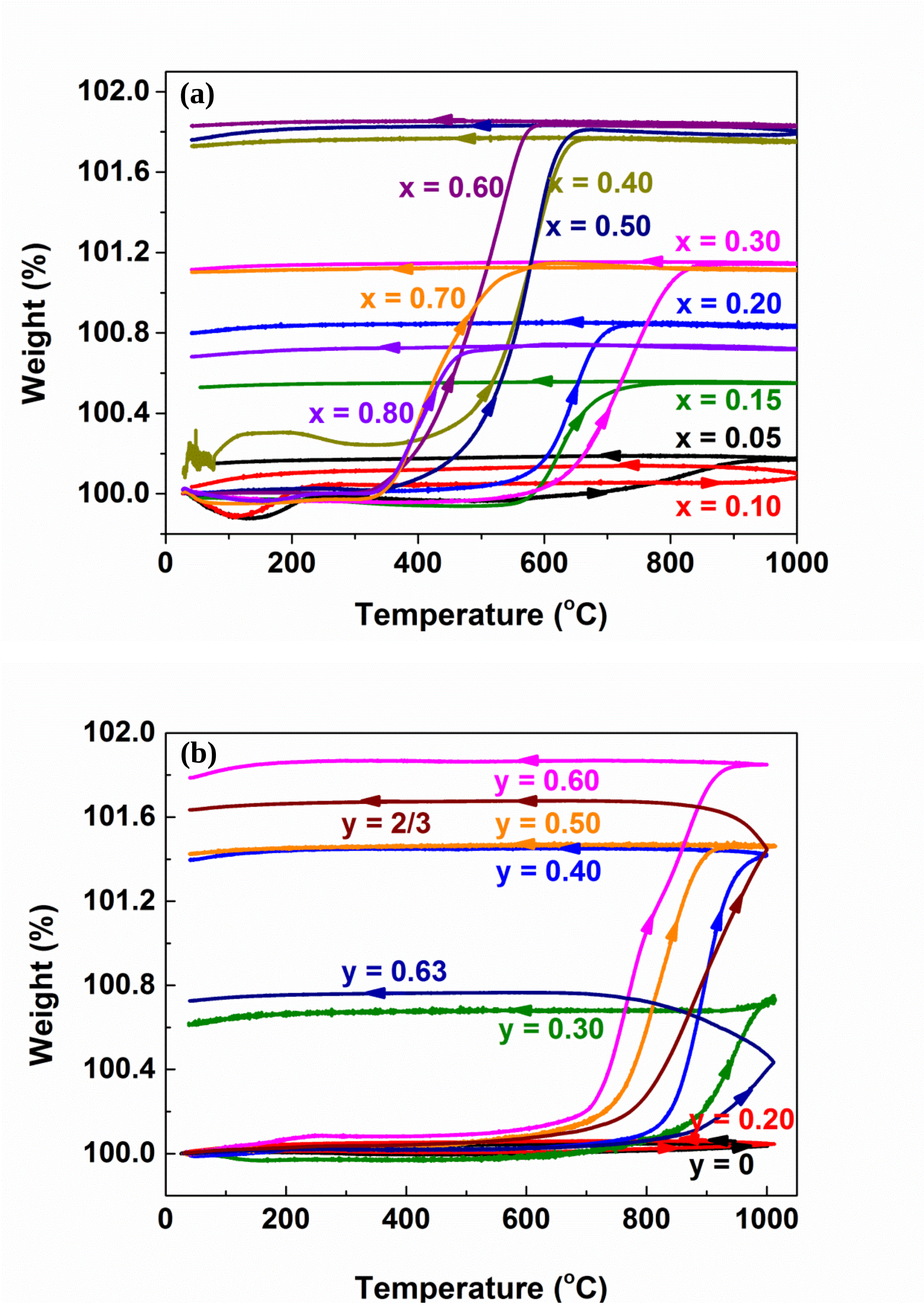

Figure 6.9 Thermogravimetric analysis recording the oxidation in air up to 1000 °C of (a) $Sr_{1-x}La_xTiO_{3-\delta}$ and (b) $Sr_{1-3y/2}La_yTiO_{3-\delta}$ ceramics sintered in N_2/5%H_2 at 1773 K for 6 hrs.

From Figure 6.9(b), for the V_a series, samples with $y \leq 0.20$ prepared in N_2/5%H_2 at 1773 K were stable in air even at 1000 °C. Therefore, we only present the TGA data of y = 0.00 and 0.20 on behalf of all $y \leq 0.20$ samples. The colour of samples after TGA was still black for $y \leq 0.20$, however, white for $y \geq 0.30$. From the XRD data after TGA, samples decomposed into TiO_2 and perovskite structures, as shown in Table 6.1.

Table 6.1 The weight variation, oxidation onset temperature and decomposed products after TGA of $Sr_{1-x}La_xTiO_{3-\delta}$ and $Sr_{1-3y/2}La_yTiO_{3-\delta}$ ceramics sintered in N_2/5%H_2 at 1773 K for 6 hrs.

Composition	Δwt. (%)	Oxidation Temperature (^oC)	Products after TGA
x = 0.10	0.13	> 1000	perovskite
x = 0.20	0.80	600	perovskite
x = 0.30	1.15	620	Sr_2TiO_4+perovskite
x = 0.40	1.55	450	Sr_2TiO_4+perovskite
x = 0.50	1.80	400	Sr_2TiO_4+perovskite
x = 0.60	1.82	320	Sr_2TiO_4+perovskite
x = 0.70	1.15	320	$La_2Ti_2O_7$+perovskite
x = 0.80	0.75	320	$La_2Ti_2O_7$+perovskite
y = 0.10	0.00	×	perovskite
y = 0.20	0.00	×	perovskite
y = 0.30	0.60	820	TiO_2+perovskite
y = 0.40	1.40	800	TiO_2+perovskite
y = 0.50	1.40	750	TiO_2+perovskite
y = 0.60	1.80	700	TiO_2+perovskite
y = 0.63	0.78	800	TiO_2+perovskite
y = 2/3	1.62	760	TiO_2+perovskite

6.3.2 Comparison of Electrical Properties for Three Mechanisms at 10 at. % La Doping

The colour of x, y, z = 0.10 pellets prepared in O_2 at 1773 K for 6 hours was black, dark green and milky white, respectively, as shown in Figure 6.10.

All doped bar samples prepared in $N_2/5\%H_2$ at 1773 K for 6 hours were totally dark in appearance.

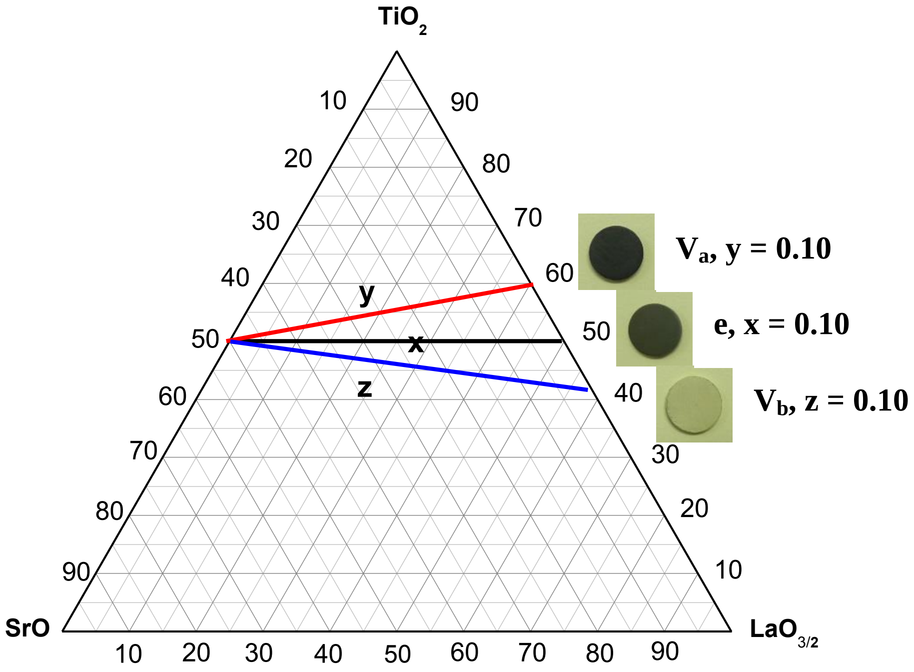

Figure 6.10 Ternary phase diagram of the LST system with the colour of x, y, z = 0.10 pellets sintered in O_2 at 1773 K for 6 hrs.

As shown in Figure 6.11, typical Z* plots at room temperature (RT) for unpolished and polished x, y = 0.10 ceramics sintered in O_2 at 1773 K were different. Highly conductive ceramics at RT were obtained for x, y = 0.10, especially y = 0.10 (< 0.5 kΩ cm after polishing), both with the appearance of a resistive surface layer that could be removed by polishing. However, almost the same Z* plots for unpolished and polished ceramics showed z = 0.10 based on the B-site vacancy mechanism to be homogeneous with really high resistivity (> 10 MΩ cm) that can not be measured by IS at RT.

Figure 6.12 shows the temperature dependence of the electrical conductivity for x, y, z = 0.10 ceramics sintered in $N_2/5\%H_2$ at 1773 K indicating that y = 0.10 has the highest electrical conductivity when sintered in reducing conditions. Therefore, effort was focused on the thermoelectric properties of the V_a, y series.

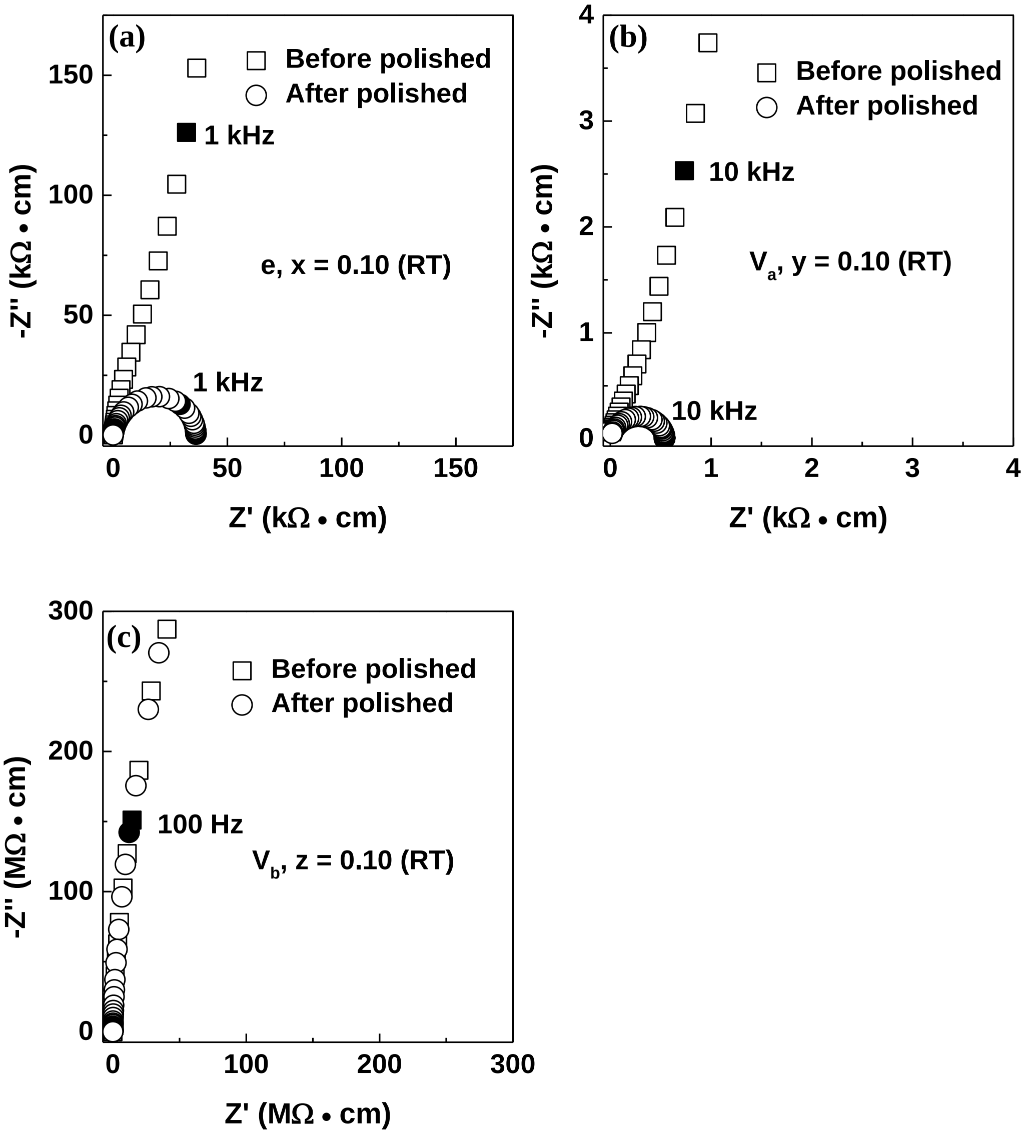

Figure 6.11 Z* plots for x, y, z = 0.10 ceramics sintered in O_2 at 1773 K for 6 hrs.

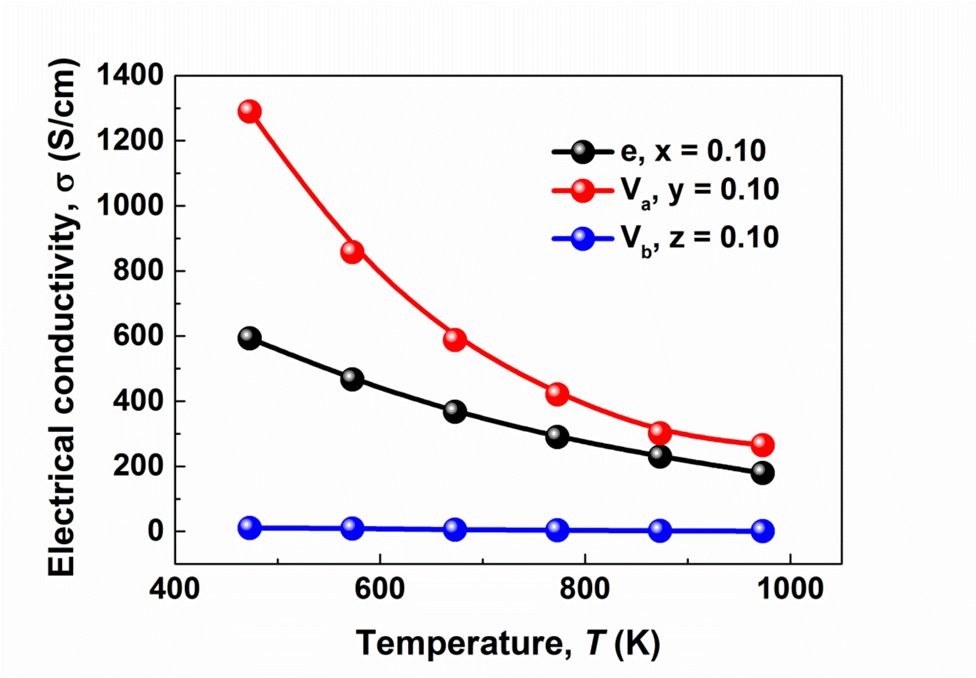

Figure 6.12 4-probe σ versus temperature for x, y, z = 0.10 ceramics sintered in N_2/5%H_2 at 1773 K for 6 hrs.

6.3.3 Thermoelectric Properties of La-doped $SrTiO_3$ with A-site Vacancy

The thermoelectric properties for the V_a series sintered in N_2/5%H_2 at 1773 K for 6 hours are shown in Figure 6.13. Negative S values suggested that all samples are n-type semiconductors. The absolute S value became smaller with increasing y, Figure 6.13(a), possibly due to an increase in the carrier concentration, Figure 6.13(b). Electrical conductivity increased at first, reached a maximum and then decreased with increasing y beyond y = 0.175, as shown in Figure 6.13(b). Thermal conductivity decreased with increasing temperature and was around 3 W m^{-1} K^{-1} at 973 K for $y \leq 0.30$, Figure 6.13(c). ZT is shown in Figure 6.13(d) and comparison of ZT at 973 K showed it to have the same trend as σ with temperature and reached a maximum ZT of 0.41 at ~973 K for y = 0.15, as shown in Figure 6.13(e).

With further increasing y, the Seebeck coefficient and electrical conductivity dropped dramatically and became too low for thermoelectric applications at $y \geq 0.40$, Figure 6.13(f) and (g). A steep decline in the electrical conductivity was observed for y = 0.40 and 0.50, Figure 6.13(g).

The Ti^{3+} content of y ≤ 0.40 samples can be calculated from an empirical equation for a cubic ST-type perovskite, as follows:

$$a = a_0 + 0.063x_{Ti^{3+}}$$

where a and a_0 are the cell parameters for N_2/5%H_2 and air sintered samples, respectively[5]. As shown in Figure 6.14, the assumed Ti^{3+} concentration was found to increase with increasing La concentration up to y = 0.20, then reached a plateau at y = 0.30 and 0.40, while the electrical conductivity at 473 K kept rising to y = 0.175 and then decreased with increase of La concentration, suggesting that the conductivity increase of these cubic perovskites with low La content (y ≤ 0.175) mainly stemmed from an increase in the carrier concentration.

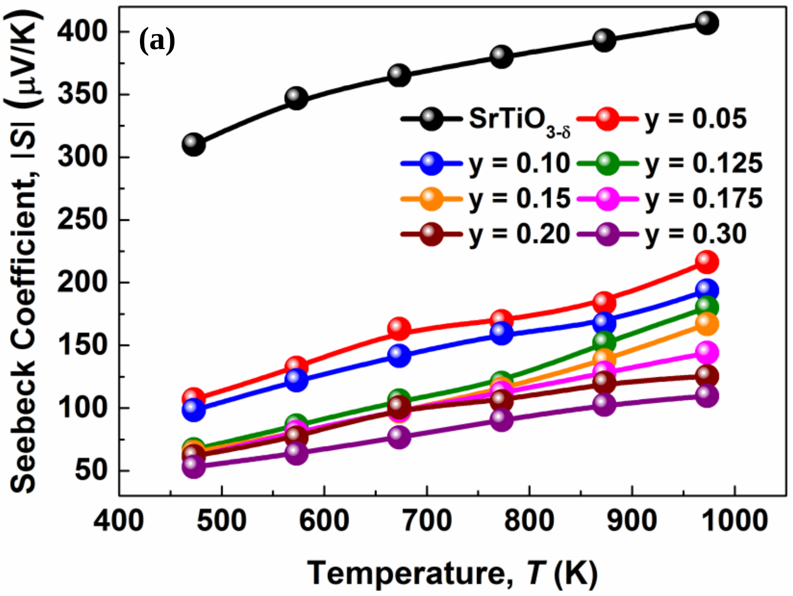

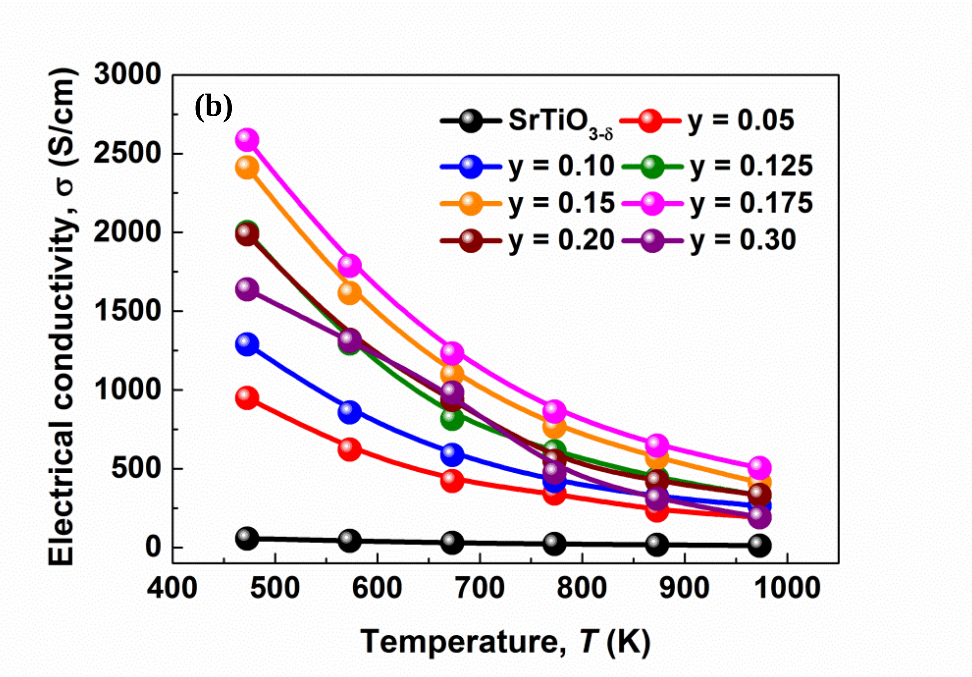
(b)
Electrical conductivity, σ (S/cm)
Temperature, T (K)
SrTiO3-δ
y = 0.05
y = 0.10
y = 0.125
y = 0.15
y = 0.175
y = 0.20
y = 0.30
0
500
1000
1500
2000
2500
3000
400
500
600
700
800
900
1000

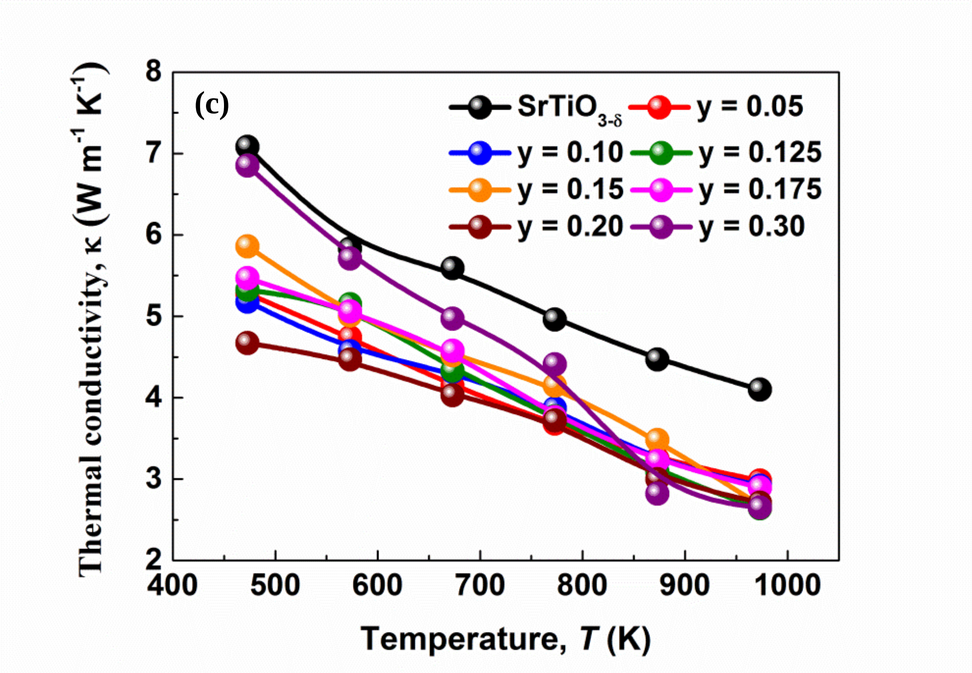
(c)
Thermal conductivity, κ (W m-1 K-1)
Temperature, T (K)
SrTiO3-δ
y = 0.05
y = 0.10
y = 0.125
y = 0.15
y = 0.175
y = 0.20
y = 0.30
2
3
4
5
6
7
8
400
500
600
700
800
900
1000

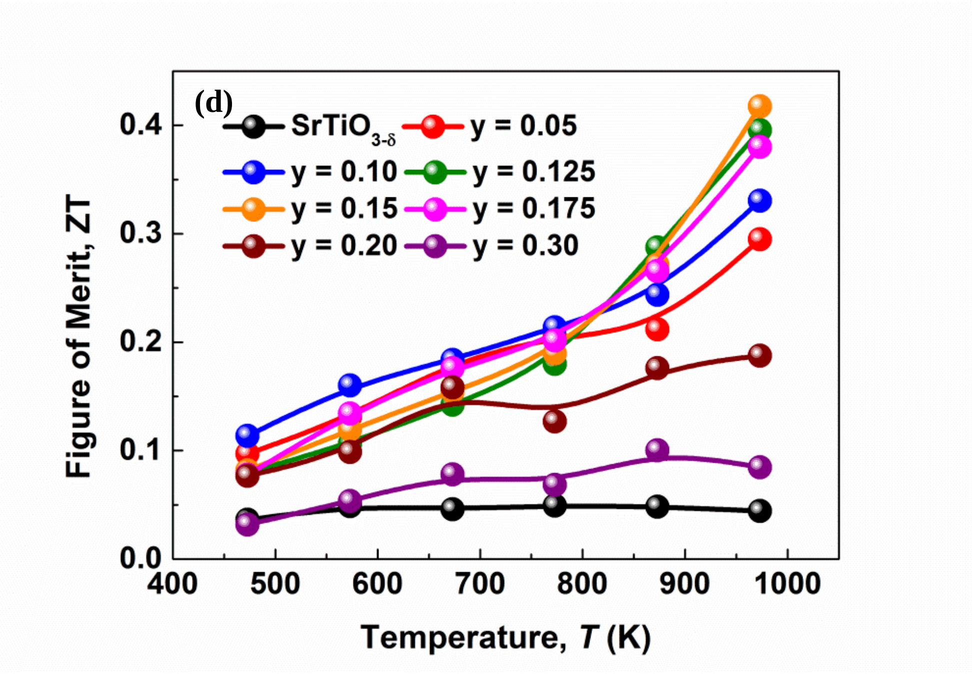
(d)
SrTiO3-δ
y = 0.05
y = 0.10
y = 0.125
y = 0.15
y = 0.175
y = 0.20
y = 0.30
Figure of Merit, ZT
0.0
0.1
0.2
0.3
0.4
Temperature, T (K)
400
500
600
700
800
900
1000

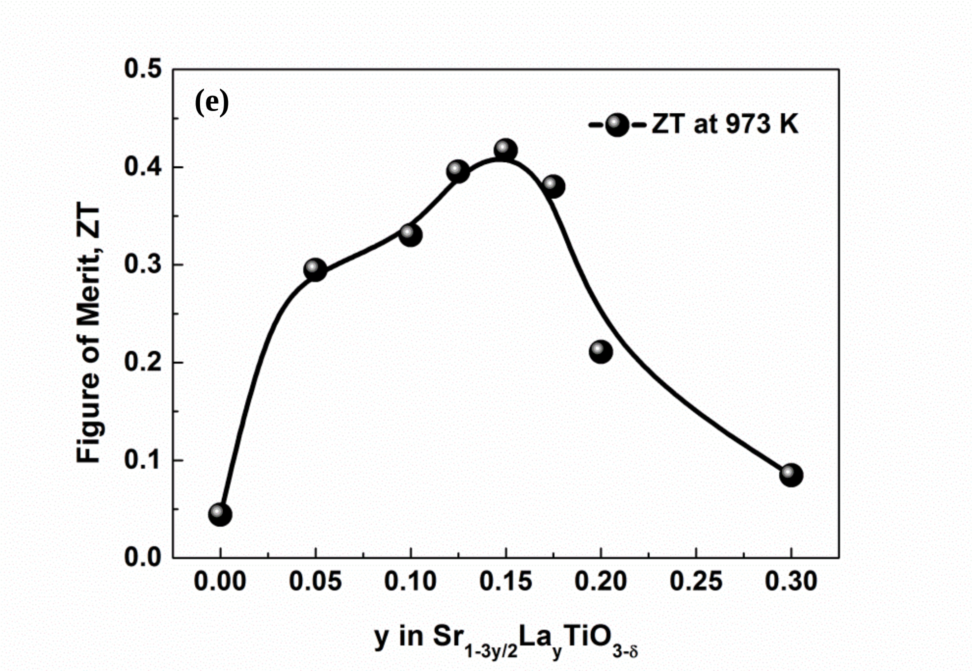
(e)
ZT at 973 K
Figure of Merit, ZT
0.0
0.1
0.2
0.3
0.4
0.5
y in Sr1-3y/2LayTiO3-δ
0.00
0.05
0.10
0.15
0.20
0.25
0.30

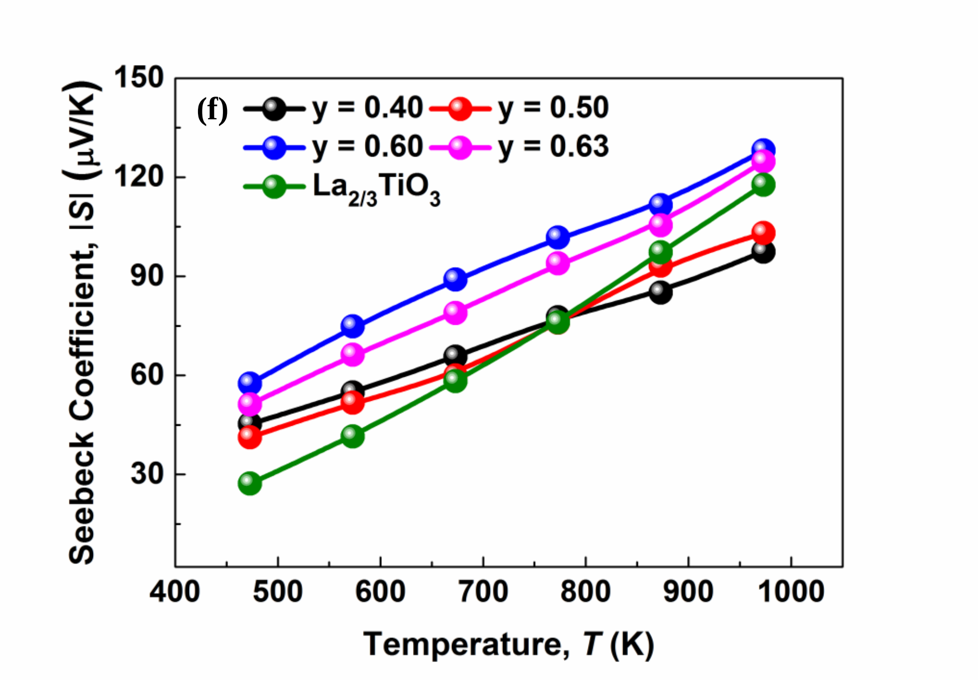

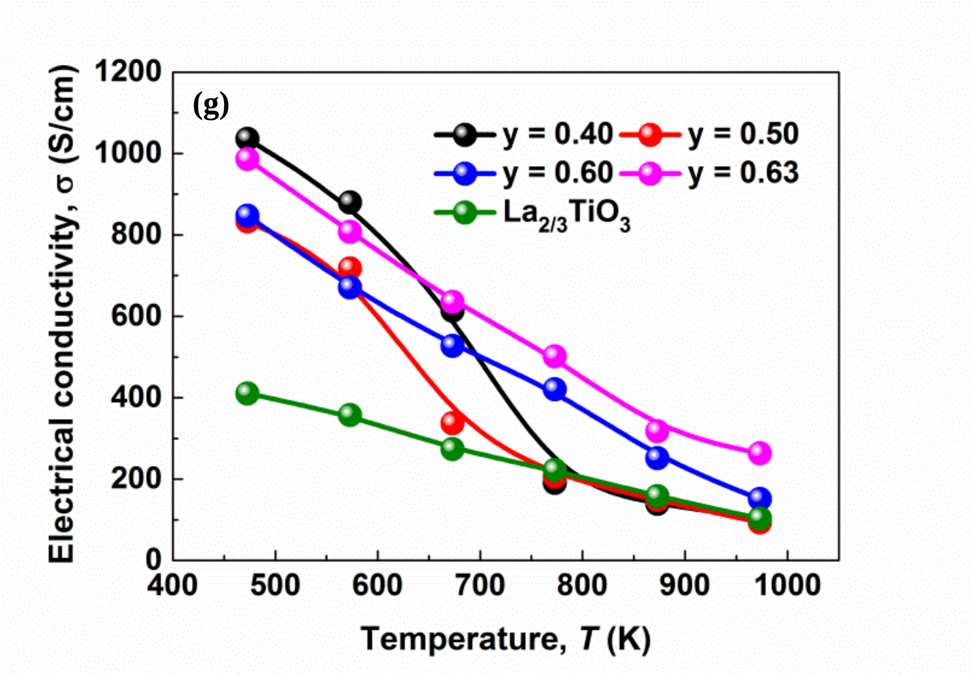

Figure 6.13 Temperature dependence of (a) S, (b) σ, (c) κ, and (d) ZT for y ≤ 0.30; (e) ZT at 973 K versus y in $Sr_{1-3y/2}La_yTiO_{3-\sigma}$ ceramics; (f) S, (g) σ for y ≥ 0.40.

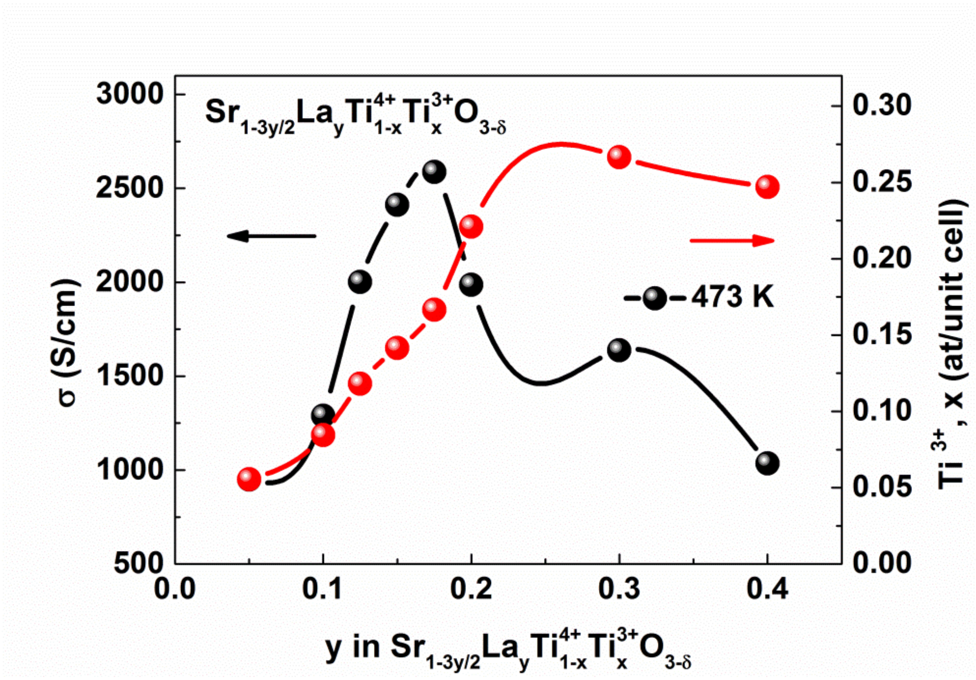

Figure 6.14 The electrical conductivity versus y at 473 K combined with the Ti^{3+} content versus y in $Sr_{1-3y/2}La_yTiO_{3-\delta}$ ceramics sintered in N_2/5%H_2 at 1773 K. The Ti^{3+} content was calculated from an empirical equation: $a = a_0 + 0.063x_{Ti^{3+}}$, where a and a_0 are the cell parameters for N_2/5%H_2 and air sintered samples, respectively[5].

6.3.4 Structure Transition Studied by TEM

10 at. % La-doped samples

Diffraction patterns obtained from x, y, z = 0.10 samples sintered in N_2/5%H_2 at 1773 K for 6 hours are shown in Figure 6.15. For all 10 at. % La doping samples, sharp discrete superstructure reflections of the type ½{ooo} were observed in <110> zone-axis electron diffraction patterns (ZADPs) with no discrete sharp superstructure present in <111> or <001> ZADPs. According to Woodward and Reaney, the appearance of only ½{ooo} reflections indicates a perovskite crystal structure in which the O octahedra are rotated in antiphase only[6] consistent with the tetragonal symmetry (I4/mcm) and $a^0a^0c^-$ Glazer tilt system[7] reported for these compositions by Howard *et al.*[8]. By XRD, 10 at. % La-doped samples were metrically cubic, however the appearance of the ½{ooo} reflection defines a lower symmetry. The absence of discernible peak splitting in in-house XRD patterns is not uncommon for perovskite ceramics tilted in antiphase only[9].

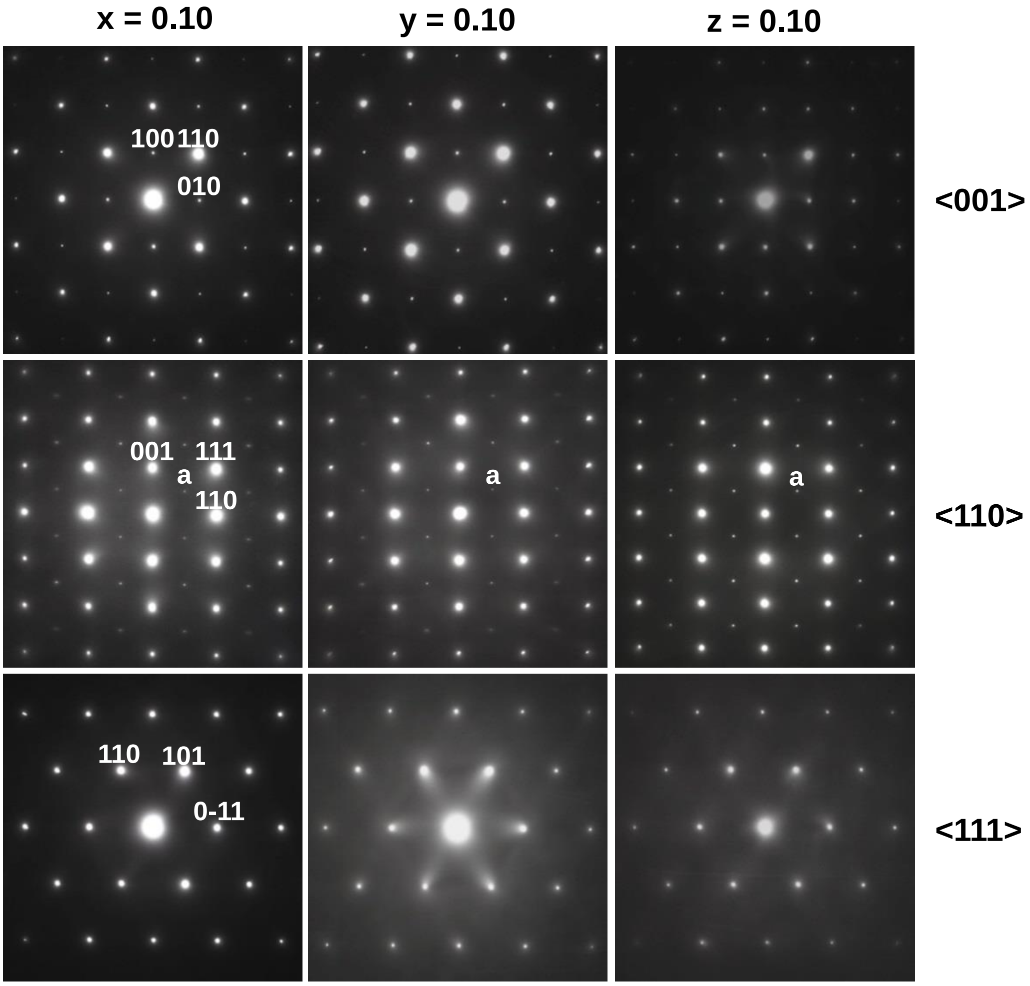

Figure 6.15 <001>, <110>, <111> zone axis diffraction patterns from $Sr_{1-x}La_xTiO_{3-\delta}$, $Sr_{1-3y/2}La_yTiO_{3-\delta}$ and $Sr_{1-z}La_zTi_{1-z/4}O_{3-\delta}$ ceramics sintered in N_2/5%H_2 at 1773 K for 6 hours. Superstructure reflections are indicated with: 'a' = ½{ooo} antiphase tilt reflection.

Air sintered samples for V_a series

<100>, <110>, <111> zone-axis electron diffraction patterns (ZADPs) from ceramics with y = 0.30, 0.50 and 0.63 sintered in air at 1773 K are shown in Figure 6.16. For samples with y = 0.30, sharp discrete reflections of the type ½{ooo} in <110> ZADPs with no discrete superstructure present in <111> or <001> ZADPs show it to be antiphase only and consistent with I4/mcm symmetry ($a^0a^0c^-$) reported by Howard *et al.*[8]. However, diffuse reflections were also observed in samples with y = 0.30 at ½{eeo} positions. These reflections are unlikely to relate to octahedral tilting as ½{eeo} only occur when both in-phase and antiphase tilting are present[6]. More likely, the diffuse reflections relate to short range order (SRO) of A-site vacancies on alternate (001) planes first proposed to exist in these compounds by Battle *et al.*[10].

For y = 0.50 and 0.63, superstructure reflections of the type ½{ooe}, ½{eeo} were observed in <001>, <110> and ½{ooe} in <111> ZADPs (Figure 6.16) ½{ooe} and ½{eeo} reflections are conventionally associated with the presence of in-phase rotations of the O-octahedra and antiparallel cation displacements, respectively,[6] but this simplistic interpretation is complicated by the presence of long range A-site vacancy order which according to Battle *et al.*[10] gives rise to primary superstructure reflections at ½{eeo}. Moreover, ½{eeo} superstructure reflections may undergo complex double diffraction routes to give rise to ½{ooe} if diffraction occurs from two domain variants of the vacancy ordered structure. Care must therefore be taken in de-convoluting these two mechanisms for the generation of superstructure. From their intensity distributions and based on structural data presented by Howard *et al.*[8] and Battle *et al.*[10], it is reasonable to assume that there are contributions to the ½{eeo} reflections from both A-site vacancy ordering and antiparallel cation displacements for compositions with y = 0.50 and 0.63, Figure 6.16.

To determine the primary origin of the ½{ooe} reflections, <111> zone axes (Figure 6.16) are particularly useful since these reflections cannot be generated by any known mechanism of double diffraction in this zone (NB

½{eeo} reflections are forbidden according to the Weiss zone law in <111> ZADPs).[6] Therefore, it can concluded that the discrete sharp reflections in <111> ZADPs from y = 0.63 arise uniquely from in-phase rotations of the octahedra, consistent with the proposed tilt system ($a^-a^-c^+$) by Howard *et al.*[8]. According to Glazer[7] and Woodward and Reaney[6], if one axis of the perovskite structure is tilted in-phase, e.g. ½(312) and ½(132) reflections (*NB these reflections are the allowed reflections of the type ½{ooe} in <111> ZADPs*) were observed in <111> zone axes but ½(321), ½(123) and ½(213), ½(231) remained forbidden. All superstructure reflections of the type ½{312} are present in the <111> ZADP for compositions with y = 0.50 because diffraction has occurred equally from all potential domain variants of the $a^-a^-c^+$ tilt system.[6] The small ferroelastic twin domain width (20 - 50 nm) associated with y = 0.50 is shown in Figure 6.18. For y = 0.63, sharp, discrete reflections were observed only at ½(312) indicating diffraction from a single variant, the structure of which has one axis tilted in-phase consistent with the tilt system ($a^-a^-c^+$) reported by Howard *et al.*[8]. Single domain diffraction patterns may be obtained from samples with y = 0.63 due to their larger domain width (0.5 μm), Figure 6.18. However, diffuse reflections of the type ½{312} are visible at all positions in <111> ZADPs from samples with y = 0.63, including diffuse halos around the sharp, discrete reflections at ½(312). The diffuse reflections are most likely associated with A-site vacancy ordering, but ½{312} (½{ooe}) reflections are forbidden according to the structure model proposed by Battle *et al.*[10], which only generates superstructure reflections of the type ½{eeo}. The origin of these reflections therefore requires further explanation.

A calculation of the proportion of A-site vacancies with respect to the available A-sites as y increases points to a simple scenario to explain the initial appearance of ½{eeo} followed by diffuse reflections at ½{ooe} as y increases. As y increases (y < 0.50, < 25% A-site vacancies), A-site vacancies accrete randomly onto alternate (001) planes, resulting in the appearance of ½{eeo} superstructure reflections. The cell doubling mechanism is the scattering power differences between the alternate partially vacated and the fully occupied (001) A-site planes. As y increases (y ≥ 0.50, ≥ 25% A-site vacancies), the A-site vacancies not only order on alternate (001) planes but also begin to undergo SRO within the partially vacated planes. The SRO in the (001) planes occurs to minimize the charge and strain associated with A-site vacancies according to the arrangement schematically illustrated in Figure 6.17, which would give rise to weak diffuse intensities at ½{ooe} positions in electron diffraction patterns in addition to strong discrete reflections at ½{eeo}.

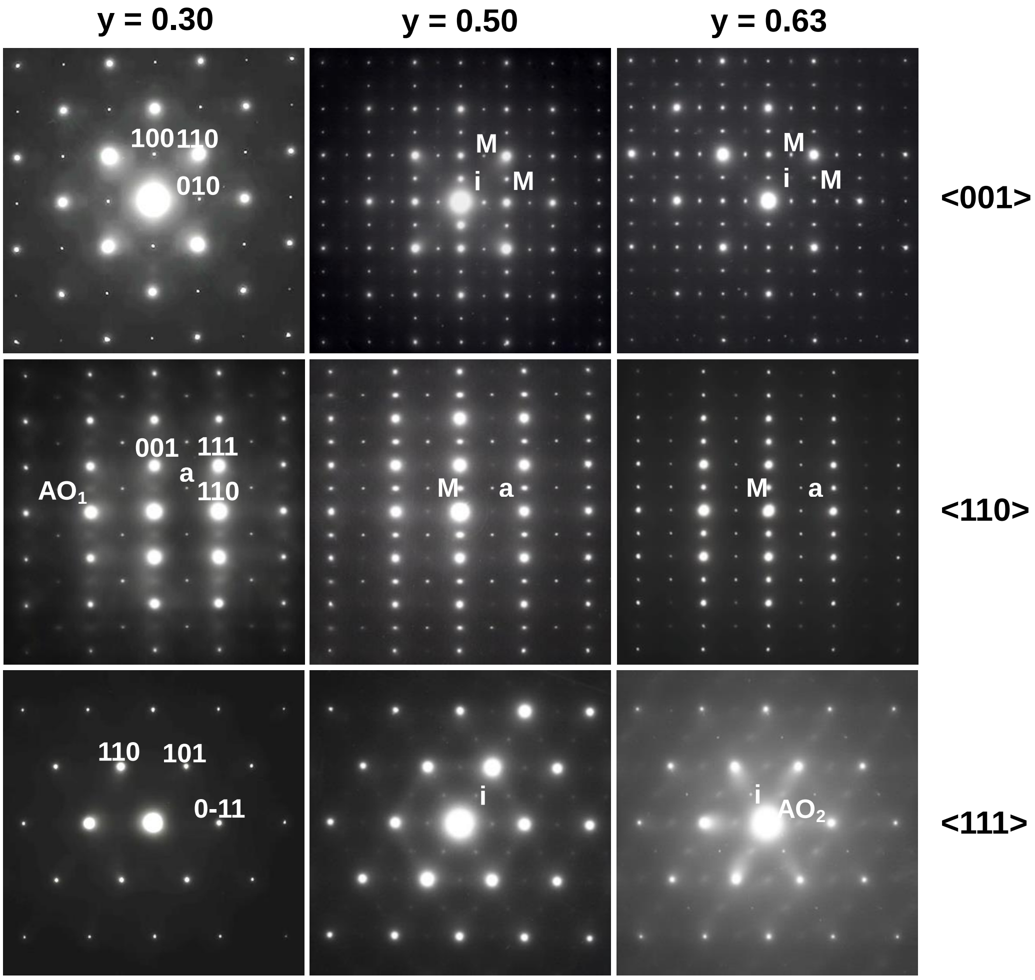

Figure 6.16 <001>, <110> and <111> zone axis diffraction patterns from $Sr_{1-3y/2}La_yTiO_3$ ceramics sintered in air at 1773 K for 6 hrs. Superstructure reflections are indicated with: 'a' = ½{ooo} antiphase tilt reflection, 'i' = ½{eeo} in-phase tilt reflection, 'AO_1' and 'AO_2' = ½{eeo} and ½{ooe} short range vacancy ordering, respectively, and M = ½{eeo} with contributions from antiparallel cation displacements and long range A-site vacancy order.

The above mechanism of A-site vacancy ordering coupled with the onset of structural transitions involving rotations of the O-octahedra can do a first approximation to explain all superstructure intensities in the electron diffraction patterns but the extent and geometry of A-site vacancy distribution as a function of sintering time and temperature are complex and worthy of further study using aberration corrected STEM in combination with a detailed crystallographic investigation using diffuse scatter in electron diffraction patterns.

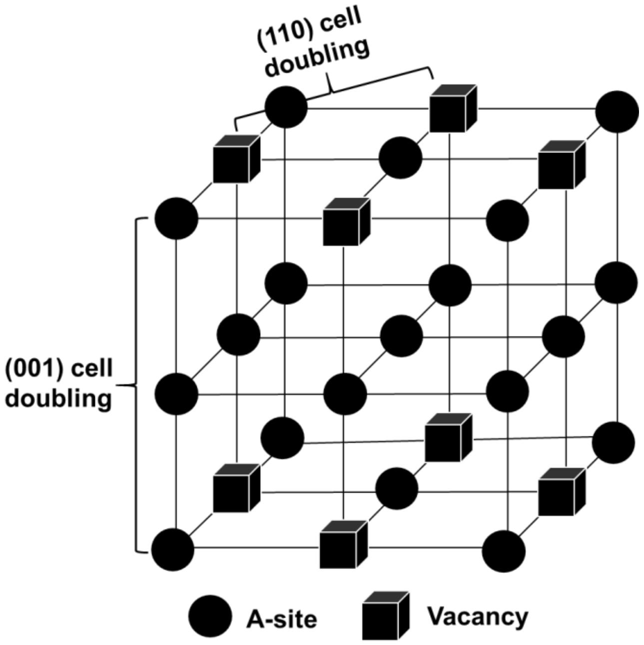

Figure 6.17 Schematic of A-site vacancy ordering scenarios in $Sr_{1-3y/2}La_yTiO_3$ sintered in air at 1773 K for 6 hrs. (001) cell doubling dominates with a transition from SRO (y = 0.30) to LRO (y ≥ 0.50) as vacancies accrete onto alternate (001) planes. As the concentration of vacancies increases, SRO occurs within the (001) planes, resulting in generation of weak diffuse ½{ooe} reflections. ((110) cell doubling) (*NB: B and O site ions are excluded for simplicity*)

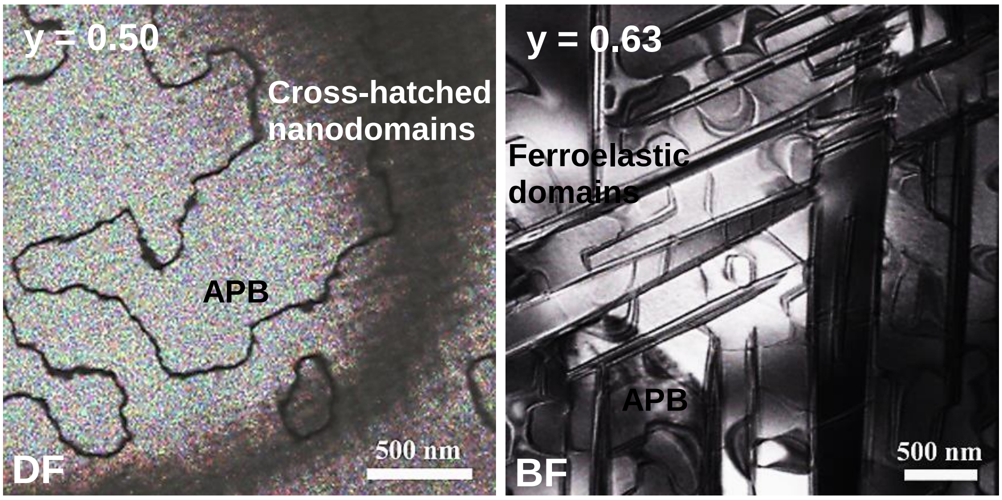

Figure 6.18 TEM images near <110> of $Sr_{1-3y/2}La_yTiO_3$ for ceramics with y = 0.50 and 0.63 sintered in air at 1773 K for 6 hrs. The dark field (DF) image reveals APBs associated with antiphase rotations of the O-octahedra. The bright field (BF) image shows ferroelastic domains due to the orthorhombic distortion and APBs relating to antiparallel cation displacements.

Figure 6.18 reveals a dark field (DF) TEM image obtained near the <110> direction using ½{ooo} from antiphase rotations of the O-octahedra and a bright field TEM image near the <110> in which ½{eeo} reflections (A-site vacancies/antiparallel cation displacements) were preferentially excited. Figure 6.18 (DF) clearly illustrates the antiphase boundaries which form due to impingement of regions of antiphase tilt that have nucleated out of phase. Note also that there is a cross hatched background contrast in Figure 6.18 (DF) which arises from ferroelastic twin domains. The twin domains are approximately 20 - 50 nm and give rise to the multidomain electron diffraction patterns discussed above in Figure 6.16. In contrast, the twin domains for samples with y = 0.63 are much larger and permit single domain diffraction data, Figure 6.16. Also visible in Figure 6.18 (BF) are antiphase boundaries that arise primarily from the impingement of regions of antiparallel cation displacements that have nucleated out of phase (a contribution to the image from regions of A-site vacancy order cannot be excluded since the ½{eeo} reflection used to form the two beam condition for the image contain intensities arising from both mechanisms for the generation of superstructure). Note that the antiphase domain width associated with antiparallel cation displacements (~500 nm) is typically less than observed for antiphase domains that arise from antiphase tilting.

N_2/5%H_2 sintered samples for V_a series

<100>, <110>, <111> ZADPs obtained from y = 0.30, 0.50 and 0.63 samples sintered in N_2/5%H_2 are shown in Figure 6.19. For y = 0.30 and 0.50 samples, <110> ZADP exhibit strong, discrete ½{ooo} reflections with no other discrete superstructure reflections present in other major ZADPs. The tilt system is thus defined as being in antiphase only and consistent with I4/mcm symmetry ($a^0a^0c^-$) proposed by Howard *et al.*[8] and also with the extra peak in XRD data at $y \geq 0.30$. It should be noted that weak ½{ooo} reflections associated with antiphase tilting are also be observed in <110> ZADPs from compositions with y = 0.10 and 0.15 (not shown here), indicating that the onset of octahedral tilting occurs at relatively low concentrations of La even though XRD traces indicate that these compositions are metrically cubic. Diffuse intensities are also observed at ½{eeo} positions in <001> and <110> ZADPs, Figure 6.19. These reflections are associated with A-site vacancy ordering but the onset of SRO occurs at y = 0.50 for N_2/5%H_2 in comparison with y = 0.30 for air sintered samples.

For y = 0.63, superstructure reflections of the type ½{ooe} are observed in Figure 6.19 revealing the presence of in-phase rotations of the O octahedra, consistent with an $a^-a^-c^+$ tilt system. The appearance of sharp discrete ½{ooe} reflections and thus the onset of in-phase tilting occurs at lower values of y in air (y = 0.50) compared with N_2/5%H_2 (y = 0.63) sintered samples. The presence of SRO A-site vacancies in samples with y = 0.50 (N_2/5%H_2) suggests that for y = 0.63, LRO should have developed. However, the coincidence of reflections at ½{eeo} positions due to antiparallel cation displacements and A-site vacancy order prevents the presence of the latter being unambiguously determined. Nonetheless, the weight of evidence suggests that A-site vacancy ordering occurs in N_2/5%H_2 but at higher values of y than in air sintered samples.

The displacement of the onset of both in-phase tilting and A-site vacancy order to high values of y for N_2/5%H_2 compared with air sintered samples is directly related to the formation of V_O in the former. First, V_O disrupts the cogwheel-like correlation of octahedral rotations and decreases the driving force for the onset of octahedral tilt transitions. This effect has been elegantly demonstrated in a range of doped $SrTiO_3$ compositions by Tkach *et al.*[11] and shown to be a universal principle in all octahedral framework compounds such as tetragonal tungsten bronzes by Zhu *et al.*[12]. Second, the formation of V_O is likely to be accompanied by the creation of Ti^{3+}. A distribution of V_O and Ti^{3+} ions throughout the lattice resulting from reduction in N_2/5%H_2 could potentially decrease the total number of A-site vacancies by facilitating direct compensation of La^{3+} through electrons (Ti^{3+}). We note however, that reduction in N_2/5%H_2 may also decrease the driving force for A-site vacancy order by creating a B-site and O-site defect distribution that coexists with the A-site distribution and disrupt the conventional charge and strain related driving forces for order.

Dark and bright field images obtained under similar conditions to those described in Figure 6.18, were also obtained for samples which had been sintered in N_2/5%H_2 (not shown). Antiphase boundaries associated with antiphase rotations of the O octahedra were routinely observed but strong contrast arising from large ferroelastic twin domains could not be routinely observed, suggesting that, even for y = 0.63, samples sintered in N_2/5%H_2 are not strongly distorted away from cubic, consistent with the XRD data shown, Figure 6.4.

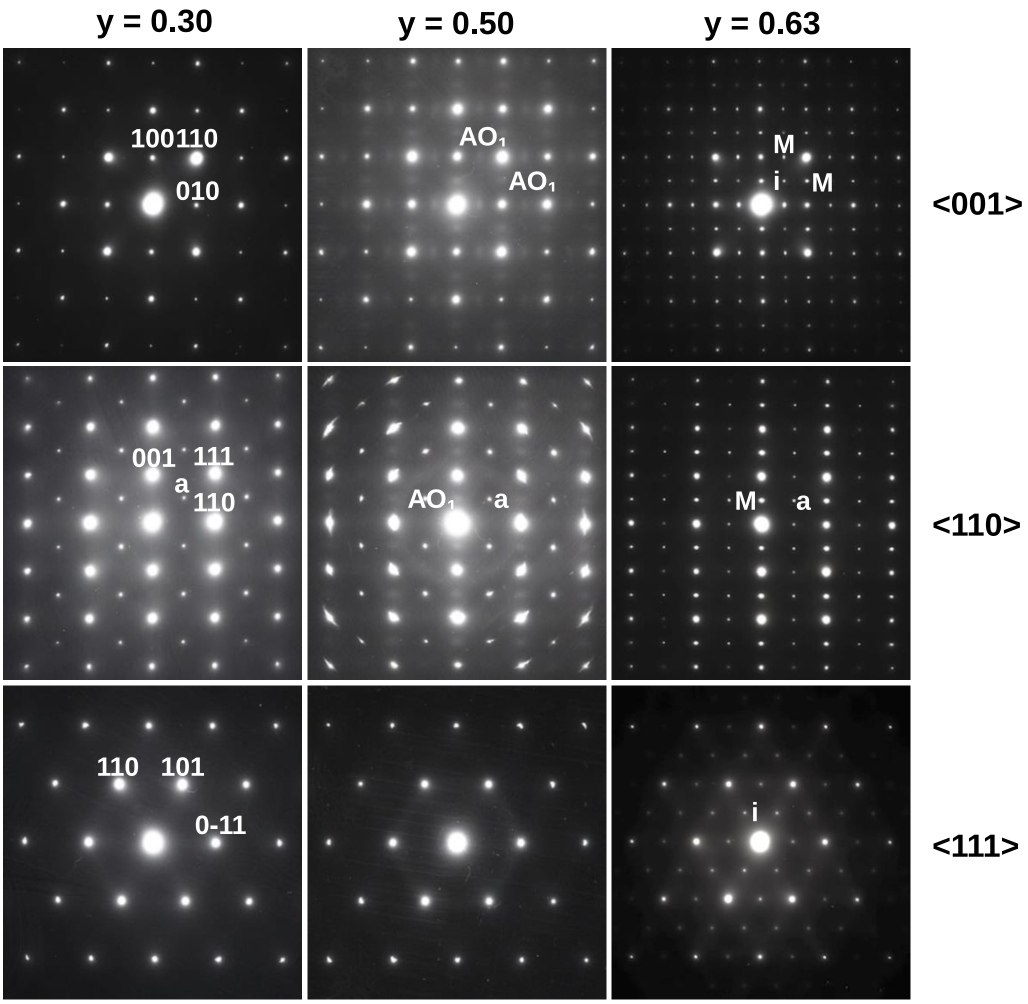

Figure 6.19 <001>, <110>, <111> zone axis diffraction patterns from $Sr_{1-3y/2}La_yTiO_{3-\delta}$ ceramics sintered in N_2/5%H_2 at 1773 K for 6 hrs. Superstructure reflections are indicated with: ‘a’ = ½{ooo} antiphase tilt reflection, ‘i’ = ½{ooe} in-phase tilt reflection, M = ½{eeo} with contributions from antiparallel cation displacements and ‘AO_1’ = short range A-site vacancy order.

6.4 Discussion and Conclusion

A thin surface layer with a similar composition (Figure 6.2) but lower electrical conductivity (Figure 6.3) to that of the ceramic interior was observed for undoped $SrTiO_3$ sintered in N_2/5%H_2 at 1773 K, caused by a pO_2 gradient within the ceramics and oxygen up-take during the cooling procedure. It was assumed that all La-doped samples had the same surface layers and therefore polished samples were used for the measurement of thermoelectric properties.

From Figure 6.4, XRD data showed that for the electronic compensation series, solid solubility for the N_2/5%H_2 sintered samples is higher ($x \leq 0.60$) than the air sintered samples ($x \leq 0.30$). For the A-site vacancy series, the solid solution exists up to the end member, $La_{2/3}TiO_3$, in N_2/5%H_2 sintered and to $y = 0.63$ in air sintered ceramics. However, for the B-site vacancy series, single phase was only observed for $z \leq 0.20$ and $z \leq 0.15$ for air and N_2/5%H_2 sintered samples, respectively. It is concluded therefore that, A-site vacancy is the most favourable compensation mechanism for La-doping in $SrTiO_3$ independent of pO_2 but that reducing conditions are more conducive for substituting La into the A-site.

When sintering in air at 1773 K, the increase of unit cell volume in proportion to La concentration for the electronic compensation series is consistent with the results of Hashimoto *et al.* who sintered their ceramics at 1723 - 1923 K and complies with Vegard's law between $SrTiO_3$ and $LaTiO_3$[13]. If we assume that samples are close to stoichiometric '$\mathrm{Sr}_{1-x}\mathrm{La}_x Ti^{4+}_{1-x} Ti^{3+}_x \mathrm{O}_3$' due to the reduction of Ti at high enough treatment temperature[14], the larger unit cell obtained by substitution of Sr ($r_{Sr^{2+}} = 1.44$ Å, CN = 12) by smaller La ions ($r_{La^{3+}} = 1.36$ Å, CN = 12) may be explained in part by the introduction of the larger Ti^{3+} ($r_{\mathrm{Ti}^{3+}} = 0.670$ Å, CN = 6) for the host Ti^{4+} ion ($r_{\mathrm{Ti}^{4+}} = 0.605$ Å, CN = 6) in the B-site. The cubic unit cell volume therefore increased with increasing La concentration for all three series when sintering in N_2/5%H_2 due in part to reduction of Ti^{4+} to Ti^{3+} but also to the formation of oxygen vacancies and the associated cation repulsion effect, as discussed by Howard *et al.*[1]. However, the unit cell volume for the air sintered V_a series samples decreased linearly with increasing La content at $y \leq 0.40$ in agreement with the results reported by Moos *et al.* for $y \leq 2/3$[15] and Howard *et al.* for $y \leq 0.60$[1]. This data suggests the decrease in average A-site ion radius through substitution of La for Sr more than offsets the formation of A-site vacancies and the lattice expansion through the small amount of Ti^{3+} present in air sintered samples. Overall, it may be concluded that the variation of unit cell volume with La concentration is complex and depends on a number factors which include cation vacancies, Ti^{3+}, oxygen deficiency and mismatch of A-site ion ionic radius.

SEM data reveal that even small amounts of cation vacancies are able to decrease the grain size from ~20 µm ($x = 0.00$) to ~5 µm ($x = 0.10$) but at high La concentration, the grain size increases. The mechanisms of grain growth are complex and the interplay of oxygen and cation vacancies with the formation of secondary phases clearly play a role but at the time of writing a coherent mechanism to explain grain growth in La-doped $SrTiO_3$ remains to be elucidated. It is noted however, that undoped $SrTiO_3$ ceramics have a complex grain boundary structure with strong evidence to suggest that they are non stoichiometric[16, 17]. It is perhaps unsurprising therefore that the exact defect chemistry of $SrTiO_3$ based ceramics has a major influence on grain growth.

Although thermogravimetric analyses does not offer a fully quantitative understanding of the amount of Ti^{3+} due to the complex phase assemblage that is obtained for the samples after re-oxidation, it nonetheless gives an important clue for the correlation of La concentration and onset temperature of oxidation for the electronic compensation and A-site vacancy series. After TGA, the colour of $x = 0.10$ and $y \leq 0.20$ samples are still black with the cubic structure, indicating these compositions are stable under oxidation compared to other compositions. As the La concentration increased however, the onset temperature for oxidation decreased. Conveniently, La-doped compositions with the best thermoelectric properties are also amongst the most stable with respect to re-oxidation, Figure 6.9 and hence may well be suitable for practical applications.

Comparison of the colours of the O_2 sintered ceramics with 10 at. % La concentration (Figure 6.10), revealed that the z = 0.10 sample (B-site vacancies) was off-white in appearance suggesting it was fully oxidised with little or no formation of Ti^{3+}. However, x, y = 0.10 samples were black and dark green, respectively, indicating some level of oxygen loss and therefore partial reduction of Ti^{4+} to Ti^{3+}. From Figure 6.11, IS at room temperature for the O_2 sintered ceramics shows heterogeneous electrical microstructures of x, y = 0.10 and the presence of insulating surface layers, associated with re-oxidation during the cooling, that can be removed by polishing, similar to La-doped $BaTiO_3$ ceramics[18]. The z = 0.10 sample is insulating before and after polishing, suggesting oxygen loss is not favoured in samples with B-site vacancies but partial reduction of Ti^{4+} to Ti^{3+} is evident for x, y = 0.10, especially y = 0.10 which contains A-site vacancies. 4 probe σ measurements were also performed on $N_2/5\%H_2$ sintered samples, confirming y = 0.10 has the highest electrical conductivity, Figure 6.12. Combining IS and 4 probe results, it is concluded therefore that La-doped $SrTiO_3$ with A-site vacancies has the highest electrical conductivity at the same La concentration (10 at. %) and sintering temperature (1773 K) independent of pO_2.

Based on selected-area electron diffraction studies, antiphase tilting was observed at x, y, z = 0.10 sintered in $N_2/5\%H_2$ samples doped with as little as 10 at. % La despite the disruptive effect of $V_{O.}$ However, the weak distortion associated with the onset of antiphase tilting in these samples could not be detected using in-house XRD and compositions remained metrically cubic.

For the case of the V_a series, XRD data revealed a phase transition from a metrically cubic phase to a distorted orthorhombic phase (tilt system $a^-a^-c^+$) at y = 0.50 and 0.63 in air and $N_2/5\%H_2$ sintered samples, respectively. However, electron diffraction patterns indicated that samples with $0.10 \leq y < 0.50$ and $0.10 \leq y < 0.63$ in air and $N_2/5\%H_2$, respectively, exhibit reflections consistent with a structure in which the octahedra are rotated in antiphase only, presumably with an $a^0a^0c^-$ (I4/mcm) tilt system, as refined by Howard *et al*[8]. The onset of octahedral tilting has been shown to be sensitive to the concentration of V_O by several authors[12, 19]. V_O disrupt the cogwheel-like correlation of O-octahedral rotations which results in either a decrease in the onset temperature of the relevant tilt transition or an increase in y before tilting occurs above ambient. The role of A-site vacancies and vacancy order in the onset of structural transitions is less clear. A-site vacancies in the context of tilting may be considered as an effective ionic radius which influences the onset of tilting through simple tolerance factor (t) considerations[20],

$$t = (R_A + R_O)/\sqrt{2}(R_B + R_O),$$

where R_A, R_B and R_O are the A, B and O site ionic radii, respectively. Ubic *et al.*[21] have discussed at length the role of A-site vacancies in the onset of structural transitions. They concluded that the effective ionic radius of the vacancy was similar to the constituent A-site ion and that no significant lowering of the tolerance factor was evident and hence there is little effect on the tilt transition temperature.

In addition to the onset of tilting, air-sintered samples revealed a transition from SRO to LRO A-site vacancies as y increased from 0.30 to 0.63 in agreement with work presented by Battle *et al.*[10]. SRO A-site vacancies were evidenced by unique weak diffuse reflections at ½{eeo} for samples with y = 0.30. Direct evidence for LRO of A-site vacancies was considered to be the unusually strong intensities associated with the ½{eeo} reflections (in comparison with ½{ooe}) in electron diffraction patterns for samples with y ≥ 0.50 sintered in air. The ½{eeo} reflections are an amalgam of intensity associated with antiparallel cation displacements and A-site vacancy order whereas ½{ooe} reflections arise uniquely from in-phase tilting. However, this qualitative interpretation requires further study using more detailed electron diffraction in addition to aberration-corrected high angle annular dark-field imaging to distinguish the order A-site vacancy distribution.

The appearance of A-site vacancy order in samples sintered in $N_2/5\%H_2$ was less clear with the driving-forces for cation/vacancy order (charge and strain) potentially disrupted by additional B- (Ti^{3+}) and O-site (V_O) defects. However, the appearance of TiO_2 and $SrTiO_3$ phases after re-oxidation suggests that the concentration of A-site vacancies is lower in samples sintered in N_2/5%H_2 and implies that at least some La^{3+} has been incorporated into the lattice through compensation by the formation of Ti^{3+} (electronic compensation). This observation is consistent with the appearance of SRO A-site vacancies for y = 0.50 rather than y = 0.30 for N_2/5%H_2 and air sintered samples, respectively. The coincidence of reflections associated with antiparallel cation displacement and A-site vacancy order at ½{eeo} however, prevents a detailed investigation using only electron diffraction and further studies are required to determine the complex interplay of A-site and O vacancies with the formation of Ti^{3+}. To understand this fully, extensive atomistic simulation is urgently required since the data presented strongly suggests that enhancement of thermoelectric properties occurs when all 3 sites are likely to exhibit charge and strain defects of the type described. A summary of electron diffraction results on $Sr_{1-3y/2}La_yTiO_3$ ceramics sintered in air and N_2/5%H_2 is shown in Table 6.2.

Table 6.2 A summary of electron diffraction results on $Sr_{1-3y/2}La_yTiO_3$ ceramics sintered in air and N_2/5%H_2 at 1773 K for 6 hrs.

Composition	**y = 0.30**		**y = 0.50**		**y = 0.63**	
Atmosphere	Air	N_2/5%H_2	Air	N_2/5%H_2	Air	N_2/5%H_2
Antiphase tilt	√	√	√	√	√	√
Inphase tilt	×	×	√	×	√	√
A-site ordering	Short	×	Long	Short	Long	Long

Optimum thermoelectric properties for $Sr_{1-3y/2}La_yTiO_3$ sintered in N_2/5%H_2 occur for ceramics with y ≈ 0.15 which represents the best combination of S, κ and σ. Importantly for applications, these compositions are not subject to easy re-oxidation as illustrated by the thermogravimetric data presented in Figure 6.9. The high degree of re-oxidation associated with samples with y > 0.20 may relate to the onset of A-site vacancy ordering observed in electron diffraction patterns which in principle could create short circuit diffusion paths for the egress and ingress of oxygen. We note however, that in $N_2/5\%H_2$ sintered samples there is no significant evidence of SRO for y = 0.30 and superstructure reflections only appear for y ≥ 0.30. Despite the absence of detectable A-site vacancy superstructure reflections for y = 0.30, it is nonetheless reasonable to consider that an increase in the concentration of A-site vacancies plays a significant role in re-oxidation. According to stoichiometry, y = 0.3 gives rise to 15% A-site vacancies. The development of SRO within the solid solution suggests that statistically, these vacancies reside on alternate (001) planes so their effective concentration on the partially vacated planes is > 15%. For y ≥ 0.50, the concentration of A-site vacancies on the partially vacated (001) planes can exceed 50% for ordered regions. We propose that the A-site vacancies create an interconnected 2D array of short circuit diffusion paths through the comparatively empty (001) A-site planes, resulting in a rapid increase in the diffusion rate of O. Increasing the La concentration, therefore increases the number and interconnectivity of these short circuit paths, resulting in rapid re-oxidation. We postulate that SRO and LRO reflections indicate the tendency for A-site vacancies to accrete onto (001) planes and lead to the conclusion that the short circuit diffusion pathways are primarily 2D and develop at comparatively low La concentration (y ~0.30). In perovskites, grain boundary O diffusion is often considered to dominate over bulk particularly at temperatures significantly lower than that of sintering (e.g. ~300 ^{o}C lower), as described extensively for $BaTiO_3$ based positive temperature coefficient thermistors[22, 23]. Doubtless, grain boundaries play a role in re-oxidation within the present study but comparison of the thermogravimetric data with grain size does not reveal a systematic trend and the increase in La concentration (and A-site vacancies) is therefore considered to dominate.

At high temperatures, values of thermal conductivity for La-doped compositions converge with only the undoped composition being significantly higher. There are many factors which influence thermal conductivity, such as point defects, dislocations and grain boundaries. However, we note that all the measured La-doped compositions exhibit octahedral rotations of the O octahedra. The combination of octahedral tilting and oxygen vacancies through reduction leads to increased disorder of the O sublattice and may be a primary contribution through phonon scattering to the lowering of thermal conductivity with respect to the undoped compound.

In conclusion, the highest ZT value (0.41) ever reported for n-type $SrTiO_3$ based ceramics at 973 K is achieved in ceramics with A-site and oxygen deficiency, which provides a highly promising route to further improve thermoelectric properties of titanate-based perovskites.

Reference

1 S. A. Howard, J. K. Yau and H. U. Anderson, Journal of Applied Physics 65, 1492 (1989).

2 J. Canales-Vázquez, M. J. Smith, J. T. S. Irvine and W. Zhou, Advanced Functional Materials 15, 1000 (2005).

3 R. Moos and K. H. Hardtl, Journal of the American Ceramic Society 80, 2549 (1997).

4 C.-D. Savaniu, D. N. Miller, J. T. S. Irvine and M. Menon, Journal of the American Ceramic Society 96, 1718 (2013).

5 D. Neagu and J. T. S. Irvine, Chemistry of Materials 22, 5042 (2010).

6 D. I. Woodward and I. M. Reaney, Acta Crystallographica Section B 61, 387 (2005).

7 A. M. Glazer, Acta Crystallographica Section B: Structural Science 28, 3384 (1972).

8 C. J. Howard, G. R. Lumpkin, R. I. Smith and Z. Zhang, Journal of Solid State Chemistry 177, 2726 (2004).

9 Y. Han, I. M. Reaney, D. S. Tinberg and S. Trolier-McKinstry, Acta Crystallographica Section B B65, 694 (2009).

10 P. D. Battle, J. E. Bennett, J. Sloan, R. J. D. Tilley and J. F. Vente, Journal of Solid State Chemistry 149, 360 (2000).

11 A. Tkach, P. M. Vilarinho and A. L. Kholkin, Acta Materialia 53, 5061 (2005).

12 X. Zhu, M. Fu, M. C. Stennett, P. M. Vilarinho, I. Levin, C. A. Randall, J. Gardner, F. D. Morrison and I. M. Reaney, Chemistry of Materials 27, 3250 (2015).

13 S. Hashimoto, L. Kindermann, F. W. Poulsen and M. Mogensen, Journal of Alloys and Compounds 397, 245 (2005).

14 M. Higuchi, K. Aizawa, K. Yamaya and K. Kodaira, Journal of Solid State Chemistry 92, 573 (1991).

15 R. Moos, T. Bischoff, W. Menesklou and K. H. Hardtl, Journal of Materials Science 32, 4247 (1997).

16 M. M. McGibbon, N. D. Browning, M. F. Chisholm, A. J. McGibbon, S. J. Pennycook, V. Ravikumar and V. P. Dravid, Science 266, 102 (1994).

17 L. Fitting, S. Thiel, A. Schmehl, J. Mannhart and D. A. Muller, Ultramicroscopy 106, 1053, (2006).

18 F. D. Morrison, D. C. Sinclair and A. R. West, Journal of the American Ceramic Society 84, 531 (2001).

19 A. Tkach, P. M. Vilarinho, A. L. Kholkin, I. M. Reaney, J. Pokorny and J. Petzelt, Chemistry of materials 19, 6471 (2007).

20 I. M. Reaney and R. Ubic, Ferroelectrics 228, 23 (1999).

21 R. Ubic, G. Subodh, M. T. Sebastian, D. Gout and T. Proffen, Chemistry of Materials 20, 3127 (2008).

22 J. Nowotny and M. Rekas, Ceramics International 17, 227 (1991).

23 R. L. Brutchey, G. Cheng, Q. Gu and D. E. Morse, Advanced Materials 20, 1029 (2008).

Chapter 7: Summary

In this project, different doping strategies and variable oxygen partial pressure were employed to study and develop La-doped $SrTiO_3$ based oxide thermoelectrics sintered at 1773 K.

Single phase undoped and La-doped $Sr_3Ti_2O_7$ ceramics were easier to be obtained in reducing conditions with a relatively insulating surface layer resulting from oxygen up-take during the cooling procedure. In the aspect of crystal structure, a TEM study confirmed that lattice strain between the layers of La-doped $Sr_3Ti_2O_7$ ceramics was released by sintering in N_2/5%H_2. For doping mechanisms, only electronic doping was found to exist up to 5 at. % La-doping in reducing conditions. A-site or B-site vacancies mechanisms did not exist for samples with > 1 at. % La concentration independent of pO_2. All air sintered La-doped $Sr_3Ti_2O_7$ were insulating with low bulk conductivity and high associated activation energies. The N_2/5%H_2 sintered La-doped $Sr_3Ti_2O_7$ ceramics with the highest electrical conductivity were phase mixtures that contained conductive cubic ST-type perovskite phase, which masked the real electrical conductivity of $Sr_3Ti_2O_7$ matrix.

For Ruddlesden-Popper phases, donor doping $(Sr, Ca)_3Ti_2O_7$ is not conductive enough for thermoelectric applications because the rock-salt layers act as electrical barriers to destroy the electrical conductivity even when they contain conductive perovskite layers[1].

In the La-doped $SrTiO_3$ system, samples also have thin surface layers due to reoxidation during the cooling procedure after being sintered in N_2/5%H_2. Following three starting nominal mechanisms with variable pO_2, samples sintered in high pO_2 (air and O_2) at 1773 K with A-site vacancies have the highest electrical conductivity. At same La-doping level and pO_2, the electrical conductivity sequence of samples sintered at 1773 K is: A-site vacancy > electronic compensation > B-site vacancy.

Reducing conditions are also beneficial for electronic and A-site vacancy compensation mechanisms in La-doped $SrTiO_3$. For the electronic compensation series, intergrowth phases of $SrTiO_3$ and $La_2Ti_2O_7$ with layered perovskite structures that are consistent with J. T. S. Irvine's work[2] were obtained at $x > 0.30$ in air and $x > 0.60$ in $N_2/5\%H_2$. For the B-site vacancy series, the solubility limit was low and independent of pO_2 suggesting B-site deficiency was not favourable in La-doped $SrTiO_3$, which is the opposite to that observed for La-doped $BaTiO_3$[3].

For samples prepared on the A-site vacancies series, cubic structures may be perserved for $y < 0.10$ in air and $y < 0.10$ in $N_2/5\%H_2$. Tetragonal structures with I4/mcm symmetry ($a^0a^0c^-$) reported by Howard et al.[4] were observed at $0.10 \leq y < 0.50$ and $0.10 \leq y < 0.63$ in air and $N_2/5\%H_2$, respectively. Orthorhombic structures with the proposed tilt system ($a^-a^-c^+$) by Howard et al.[4] and Battle et al.[5] were obtained at $y \geq 0.50$ in air and $y \geq 0.63$ in $N_2/5\%H_2$. Short range V_{Sr} ordering occurred at $y = 0.30$ in air and at $y = 0.50$ in $N_2/5\%H_2$. Long range V_{Sr} ordering appeared at $y \geq 0.50$ in air and $y \geq 0.63$ in $N_2/5\%H_2$.

The highest ZT value (0.41) ever reported for an n-type $SrTiO_3$ based ceramics at 973 K has been achieved in 15 at. % La doped $SrTiO_3$ with A-site and oxygen deficiency. High thermoelectric properties and oxidising temperature for samples with $y \geq 0.20$ sintered in $N_2/5\%H_2$ maybe related to their slight distortion away from a cubic structure with randomly distributed A-site and O-site vacancies. However, lower thermoelectric properties and oxidising temperatures for samples with $y > 0.2$ sintered in $N_2/5\%H_2$ may be due to the onset of A-site vacancy ordering that could create some form of short circuit for rapid oxygen diffusion pathways.

In summary, this project has accomplished the task to improve the thermoelectric properties and understanding of the structure-composition -property relationships of La-doped $SrTiO_3$ based oxide thermoelectrics. It provides a highly promising route to further improve the thermoelectric properties of titanate-based perovskites.

Reference

1 N. Sirikanda, H. Matsumoto and T. Ishihara, Solid State Ionics 181, 315 (2010).

2 J. Canales-Vázquez, M. J. Smith, J. T.S . Irvine and W. Zhou, Advanced Functional Materials 15, 1000 (2005).

3 C. L. Freeman, J. A. Dawson, H.-R. Chen, L. Ben, J. H. Harding, F. D. Morrison, D. C. Sinclair and A. R. West, Advanced Functional Materials 23, 3925 (2013).

4 C. J. Howard, G. R. Lumpkin, R. I. Smith and Z. Zhang, Journal of Solid State Chemistry 177, 2726 (2004).

5 P. D. Battle, J. E. Bennett, J. Sloan, R. J. D. Tilley and J. F. Vente, Journal of Solid State Chemistry 149, 360 (2000).

Chapter 8: Future Work

For the La-doped $Sr_3Ti_2O_7$ system, a combination of X-ray/Neutron diffraction with Rietveld refinement of data and atomic resolution scanning transmission electron microscopy (STEM) needs to be employed to investigate whether the La ions dope into the rock salt layer or perovskite blocks in $Sr_3Ti_2O_{7.}$ This information will be useful in trying to fully understand the conduction mechanism and may provide direct support for the proposition of the formation of electrical barriers due to insulating rock salt layers.

A detailed TEM study still needs to be carried out to ascertain the space group symmetry for the La-doped $SrTiO_3$ system. The extent and geometry of A-site vacancy distribution are worthy of further study using aberration corrected STEM in combination with a detailed crystallographic investigation using diffuse scatter in electron diffraction patterns.

For La-doped $BaTiO_3$, simulation results have indicated that oxygen loss due to the arrangement of La ions on the A-site with B-site vacancies leads to semi-conductivity of $BaTiO_3$[1]. A similar atomistic modelling study of La-doped $SrTiO_3$ would be useful to establish whether or not there is also a link between A-site vacancies and oxygen loss[2]. This would explain the higher electronic conductivity observed for A-site deficient compositions compared to stoichiometric (donor-doped) compositions.

The electrical properties of La doped $SrTiO_3$ ceramics sintered in air at various temperatures based on the three different doping mechanisms should be studied by Impedance Spectroscopy to detect oxygen-loss and electrical heterogeneity in these materials.

Calcining mixed powders of La-doped $SrTiO_3$ in N_2/5%H_2 instead of air before sintering may lead to more oxygen-loss and therefore higher conductivity. In addition, Spark Plasma Sintering might create dense ceramics with microstructures of restricted grain size and this may give rise to better thermoelectric properties by their lowering thermal conductivity without decreasing the electrical conductivity.

In addition to other single Rare Earth (RE) dopants, a detailed study of RE A-site co-doped and/or A-site and B-site (donor) co-doped $SrTiO_3$ systems may further enhance the thermoelectric properties in this system. Some of these systems have recently been reported in the literature, for example $Sr_{1-x}La_{0.67x}Ti_{1-y}Nb_yO_{3-\delta}$ by Bos[3].

Reference

1 C. L. Freeman, J. A. Dawson, H.-R. Chen, L. Ben, J. H. Harding, F. D. Morrison, D. C. Sinclair and A. R. West, Advanced Functional Materials 23, 3925 (2013).

2 J. A. Dawson, X. Li, C. L. Freeman, J. H. Harding and D. C. Sinclair, Journal of Materials Chemistry C 1, 1574 (2013).

3 S. R. Popuri, A. J. M. Scott, R. A. Downie, M. A. Hall, E. Suard, R. Decourt, M. Pollet and J.-W. G. Bos, RSC Advances 4, 33720 (2014).